

NASA TECHNICAL
MEMORANDUM



NASA TM X-1979

NASA TM X-1979

EFFECT OF UNDERWING ENGINE
NACELLE SHAPE AND LOCATION ON
BOATTAIL DRAG AND WING PRESSURES
AT MACH NUMBERS FROM 0.56 TO 1.46

by *Bernard J. Blaha*
Lewis Research Center
Cleveland, Ohio

FACILITY FORM 602	N70-21658	
	(ACCESSION NUMBER)	(THRU)
	72	1
	(PAGES)	(CODE)
	TM X 1979	01
	(NASA CR OR TMX OR AD NUMBER)	(CATEGORY)

1. Report No. NASA TM X-1979	2. Government Accession No.	3. Recipient's Catalog No.	
4. Title and Subtitle EFFECT OF UNDERWING ENGINE NACELLE SHAPE AND LOCATION ON BOATTAIL DRAG AND WING PRESSURES AT MACH NUMBERS FROM 0.56 TO 1.46		5. Report Date March 1970	
		6. Performing Organization Code	
7. Author(s) Bernard J. Blaha		8. Performing Organization Report No. E-5348	
9. Performing Organization Name and Address Lewis Research Center National Aeronautics and Space Administration Cleveland, Ohio 44135		10. Work Unit No. 126-15	
		11. Contract or Grant No.	
12. Sponsoring Agency Name and Address National Aeronautics and Space Administration Washington, D. C. 20546		13. Type of Report and Period Covered Technical Memorandum	
		14. Sponsoring Agency Code	
15. Supplementary Notes			
16. Abstract A 1/20-scale model of the F-106 aircraft with simulated underwing engine nacelles was tested in the Lewis Research Center 8- by 6-Foot Supersonic Wind Tunnel. Boattail pressure drag, wing pressures, and nacelle pressures were obtained on a series of configurations including changes in nacelle and inlet geometry and location under the wing. Boattail pressure drag was obtained with jet boundary simulators on 15°, 20°, and 25° conical boattail afterbodies each with a boattail-to-nacelle area ratio of 0.551. Data were obtained with and without inlet airflow through the nacelles at angles of attack from 0° to 15°. Installed-boattail pressure-drag coefficient was lower than isolated-nacelle values at all Mach numbers, and transonic boattail drag rise was delayed to Mach 0.98. The effects of changes in nacelle and inlet geometry and location were generally small. Conical boattail angles greater than 15° tended to increase local regions of flow separation.			
17. Key Words (Suggested by Author(s)) Airframe installation effects; Airframe nacelle integration; Propulsion system; Transonic; Underwing nacelles; Flight test; Nozzle installation, Boattail, Boattail drag; Aircraft component drag; Variable flap ejector nozzle		18. Distribution Statement Unclassified - unlimited	
19. Security Classif. (of this report) Unclassified	20. Security Classif. (of this page) Unclassified	21. No. of Pages 71	22. Price* \$3.00

*For sale by the Clearinghouse for Federal Scientific and Technical Information
Springfield, Virginia 22151

EFFECT OF UNDERWING ENGINE NACELLE SHAPE AND LOCATION ON BOATTAIL DRAG AND WING PRESSURES AT MACH NUMBERS FROM 0.56 TO 1.46

by Bernard J. Blaha
Lewis Research Center

SUMMARY

Tests were conducted in the Lewis Research Center 8- by 6-Foot Supersonic Wind Tunnel using a 1/20-scale model of the F-106 aircraft with simulated underwing engine nacelles. Boattail pressure drag, wing pressures, and nacelles pressures were obtained on a series of configurations including changes in nacelle and inlet geometry and location under the wing. Boattail drag was obtained by pressure integration with conical 15° , 20° , and 25° boattail afterbodies each with a boattail-to-nacelle area ratio of 0.551 and a jet-boundary simulator. Data were obtained with and without inlet airflow through the nacelles at angles of attack from 0° to 15° .

Airframe installation resulted in increased pressure on the wing lower surface near the nacelle forebody and decreased pressure near the cylindrical portion of the nacelle. These effects on the wing flow field combined with the effects on the nacelle flow field resulted in reduced boattail drag coefficient at all Mach numbers, and the transonic drag rise was delayed until Mach 0.98. Good agreement was observed between flight and wind tunnel model results except at Mach 1.0 where the flight installation effects were small. The effects of changes in nacelle and inlet geometry on boattail drag were generally small except for a flared-nacelle configuration. The effects of increased nacelle spanwise location were small at subsonic speeds and resulted in further reductions in boattail drag at the supersonic speeds. Increased boattail angle resulted in local regions of afterbody flow separation. Increased angle of attack resulted in increased pressure forward on the lower surface of the wing but had little effect on boattail pressure drag for angles less than 8.5° .

INTRODUCTION

As part of a program in airbreathing propulsion, the Lewis Research Center is investigating airframe-installation effects on the performance of nozzle systems appro-

appropriate for use at supersonic speeds. In this program, airframe-installation effects are being investigated both in wind tunnel and flight tests at subsonic and transonic speeds.

Past experience has shown that performance of an exhaust nozzle system can be appreciably affected by installation on an aircraft, especially at off-design conditions (ref. 1). For an engine-nacelle installation typical of a supersonic-cruise aircraft, the nacelle may be installed close to the lower surface of a large wing, and the afterbody may extend downstream of the wing trailing edge. This aft location of the nacelle provides shielding of the inlet by the wing surface to minimize angle-of-attack effects and may also provide favorable interference between the nacelle and wing. To investigate installation effects on the flow over a podded engine installation of this type, Lewis is conducting a flight test program utilizing an F-106 aircraft with underwing engine nacelles housing J-85 afterburning turbojet engines. The F-106 aircraft was selected for this study because it is a delta-wing aircraft capable of flight at supersonic speeds. In this flight program, installation effects are being investigated on complex exhaust nozzles in the high subsonic and transonic speed range because wind tunnel models are limited to very small size to avoid wall interference effects. In a concurrent effort, tests are being conducted in the Lewis 8- by 6-Foot Supersonic Wind Tunnel utilizing a 1/20-scale model of the F-106 aircraft with simulated underwing engine nacelles with 15° sharp-edge boattail afterbodies. Some of the results of these tests are presented in reference 2 and indicate that with an airframe installation of this type, boattail drag is reduced at all Mach numbers and the transonic boattail drag rise is delayed to Mach 0.98.

To further investigate these effects the 1/20-scale model of the F-106 aircraft was subsequently retested in the 8- by 6-Foot Supersonic Wind Tunnel. Boattail drag, nacelle pressures, and wing pressures were obtained on a series of model configurations including changes in nacelle and inlet geometry and in nacelle position. Boattail drag was obtained on 15°, 20°, and 25° sharp-shoulder conical afterbodies with jet-boundary simulators. These afterbodies simulated the geometry of variable-flap ejector-type nozzles when the exit area is closed for operation at subsonic and transonic speeds. Data were obtained with and without inlet airflow through the nacelles over a Mach number range of 0.56 to 1.46 at angles of attack from 0° to 15°. Some of the results of these tests are presented in reference 3. However, the detailed results of these tests are presented herein, and comparisons are made with flight test results (ref. 4) and with wind tunnel data from isolated-nacelle tests (refs. 5 and 6) and tests with a nacelle under a simulated wing (refs. 7 and 8).

SYMBOLS

A	cross-sectional area of nacelle at boattail juncture
A_β	projected area of boattail
b	wing span, 59.1 cm
$(C_D)_\beta$	axial boattail pressure-drag coefficient, (Axial force)/ $q_0 A$
C_p	pressure coefficient, $(p - p_0)/q_0$
d_{\max}	reference diameter of nacelle at the boattail juncture
l	axial distance coordinate
M_0	free-stream Mach number
P_0	free-stream stagnation pressure
p	local static pressure
p_0	free-stream static pressure
q_0	free-stream dynamic pressure
R	Reynolds number per meter
$w\sqrt{\tau}$	corrected secondary flow ratio
x	axial distance coordinate along nacelle
Y	coordinate defining upper surface of nacelle strut or lower surface of wing near nacelle at $2y/b = 0.313$
y	spanwise distance coordinate
z	distance coordinate defining width of nacelle strut
α	model angle of attack, deg
φ	angular coordinate, deg

APPARATUS AND PROCEDURE

Figure 1 is a schematic drawing of the model installation in the transonic test section of the Lewis 8- by 6-Foot Supersonic Wind Tunnel. The model, a 1/20-scale of the F-106 aircraft, was sting mounted from the tunnel floor strut. In figure 2 the model is shown installed in the 8-foot, 3.1-percent-porosity wind tunnel test section with open bulged nacelles mounted under the wing. Tests were conducted over a range of Mach numbers from 0.56 to 1.46 at angles of attack from 0° to 15° . Reynolds number varied from 11.8×10^6 per meter at Mach number 0.56 to 16.28×10^6 per meter at Mach

number 1.46. Model blockage at 0° angle of attack was less than 0.3 percent. Although the model scale was relatively small, it was selected to avoid effects of tunnel wall interference at transonic Mach numbers.

Schematic drawings of the model details, the instrumentation, and the installation of the simulated engine nacelles under the wings are shown in figure 3. Model dimensions are shown in figure 3(a). The aircraft model was 97.6 centimeters long and had a 60° sweptback delta wing with a 29.57-centimeter semispan. The F-106 fuselage inlets were open and thus allowed airflow to pass through the model fuselage. The simulated engine nacelles were strut mounted to the lower surface of the wing on each side of the fuselage at the basic spanwise station of 9.26 centimeters (or 31.4 percent semispan). Tests were also conducted with the nacelles at spanwise stations of 18.21 centimeters (or 61.6 percent semispan). Hereinafter, these nacelle spanwise stations are called inboard and outboard with respect to the fuselage centerline. Details of the model wing instrumentation are shown in figures 3(b) and (c). Sixteen pressure orifices were installed on the upper surface of the right wing (as viewed in the upstream direction). These orifices were arranged in two axial rows on either side of the nacelle inboard spanwise station ($y = 9.26$ cm). Forty-eight pressure orifices were installed on the lower surface of the left wing. These orifices were arranged to yield both axial and spanwise pressure distributions, with the concentration being near the nacelle inboard spanwise station. Details of the pressure instrumentation installed on the aft end of the fuselage are shown in figure 3(d). The typical nacelle installation under the model wing is shown in figure 3(e). The nacelles were installed at incidence angles of between -3° to -4.5° with respect to the wing chord (dependent on nacelle configuration) and extended aft of the wing trailing edge. The nacelles also extended below the lower surface of the fuselage, which was fairly flat in the region of the nacelles. However, because of area-rule considerations, the fuselage sidewalls, which extended below the wing, had a slight contour in the vicinity of the nacelles (fig. 3(a)). Each nacelle configuration tested had a conical boattail with zero radius of curvature at its juncture with the cylindrical portion of the nacelle and was followed by a cylindrical jet-boundary simulator. The purpose of the simulator was to approximate the local flow field that would exist in the presence of a jet with an exit-to-local-static pressure ratio of 1.0. In figure 3(e) the wing lower surface coordinates along the inboard spanwise station in the vicinity of the nacelle are shown. Fixed sections of the elevons, hereinafter called elevon cutouts, were used above the nacelles.

All the nacelle geometries investigated in this series of tests are shown in figures 4 to 8. Figure 4 is a series of schematic drawings of the solid nacelle geometries. The solid nacelles had 3.145-centimeter-diameter cylindrical bodies and were designed such that the forebodies and boattails could be detached and changed. The basic nacelle body length was 14.82 centimeters, and the base of the 15° boattails was located 0.97 nacelle diameters aft of the wing trailing edge. To investigate the effects of a change in fore-

body geometry, three forebodies were tested: a 6.1° half-angle conic forebody (fig. 4(a)), a 10° half-angle conic forebody (fig. 4(b)), and an ogive forebody with a length-to-maximum-diameter ratio of 3.0 (fig. 4(c)). The nacelle with the 6.1° conic forebody was identical to the solid cylindrical nacelle described in reference 2. The 10° conic forebody nacelle was similar to the larger nacelle described in references 5, 7, and 8. Each of the forebody geometries were tested on the cylindrical nacelles with 15° conic boattail afterbodies.

To investigate the effects of increased boattail angle on installed afterbody pressure drag and installed afterbody flow separation, 20° and 25° conic boattails (figs. 4(d) and (e)) were tested with the 10° conic forebody nacelle. These nacelles with the increased boattail angles were geometrically similar to the nacelles described in reference 8. To facilitate comparison of the afterbody drag results, all the afterbodies investigated had a ratio of projected boattail area to cross-sectional area of the nacelle, based on the diameter at the boattail-nacelle juncture A_β/A , of 0.551. The nacelles with the 10° conic forebodies and 15° boattails were also used to investigate the effects on afterbody drag of inboard and outboard nacelle location. The outboard location was tested both with and without an adjacent inboard nacelle. To investigate the effects of a change in nacelle length on afterbody drag with the 15° boattails, the ogive forebody was tested with two lengths of the cylindrical portion of the nacelle body: 14.82 and 8.63 centimeters.

Figure 4(f) shows a schematic drawing of the nacelle struts. Figure 4(g) shows the instrumentation on the solid nacelles. These nacelles were instrumented over their entire length with static-pressure orifices located at five angular coordinate stations φ . The nacelles on each side of the fuselage were similarly instrumented, except at the $\varphi = 180^\circ$ station. Because of the symmetry seen in the nacelle pressures presented in reference 2, only a small number of orifices were installed on the right nacelle at $\varphi = 180^\circ$ for the present tests. For the same reason, only a few orifices were installed at the $\varphi = 45^\circ$ and 90° stations of either nacelle. The pressures measured at $\varphi = 270^\circ$ and 315° on the right nacelle were assumed to be equal to those at $\varphi = 90^\circ$ and 45° , respectively, on the left nacelle. Each boattail had orifices located at three angular coordinate stations, $\varphi = 0^\circ$, 180° , and 270° and at eight axial stations (five for the 25° boattails). Eight orifices at each angular coordinate station was double the number used on the boattails described in reference 2. Each of these orifices was located at the centroid of equal annular areas, thus an equal projected area was assigned to each orifice. The three axial rows of orifices on the boattail under one wing were then combined with the missing row of orifices ($\varphi = 270^\circ$) from the boattail under the other wing. Together these orifices were then used to obtain the integrated boattail axial pressure-drag coefficient defined as follows:

$$\left(C_D\right)_\beta = -\frac{A_\beta}{A} \bar{C}_p$$

where \bar{C}_p is the average boattail pressure coefficient. The instrumentation for the solid nacelles was brought out through the end of the jet-boundary simulators.

Figure 5 is a schematic diagram of the two basic open-nose nacelles described in reference 2: a cone cylinder configuration and a similar configuration with a bulged section added to the lower surface to simulate an engine accessory pod. These nacelles were retested without nacelle or afterbody instrumentation to obtain the effects of these geometries on wing and fuselage pressures. These effects were not obtained in the tests discussed in reference 2. The latter nacelle configuration is a scaled version of the nacelle being used in the F-106 flight test program with underwing engine nacelles housing J-85/13 engines. The nacelles shown in figure 5 had normal shock inlets, which allowed stream flow to pass through the nacelle body and exit at the aft end of the jet-boundary simulator.

Figure 6 shows the details of the bent-nacelle configuration. Schematic drawings of the side view and plan view of the nacelle installation under the wing are shown in figures 6(a) and (b). The nacelles installed on the model and the nacelle and strut dimensions are shown in figures 6(c) and (d), respectively. This nacelle geometry was investigated because it was more representative of engine nacelles that have been proposed for future supersonic-cruise-type aircraft than the nacelles described in reference 2. The nacelle had three conic sections ahead of a 15° boattail with a jet-boundary simulator and had an open spike inlet with an 11° half-angle spike. The inlet capture and flow areas were selected to approximate the transonic mass flow ratio characteristics of a supersonic-cruise turbojet propulsion system. The nacelle had a 3° cowl, which was followed by a 3° half-angle divergent section that was bent upward in the vertical plane at 3° to the cowl section. This section simulated the engine segment of the nacelle and had a maximum diameter of 3.454 centimeters. The engine segment of the nacelle was followed by a 3° tapered section to the boattail juncture, which was bent downward 6° with respect to the engine segment of the nacelle. The 15° boattail had the same ratio of projected area to nacelle area based on the nacelle diameter at the boattail juncture as the other boattails tested ($A_\beta/A = 0.551$). The combined 3° tapered segment and 15° boattail were representative of a typical auxiliary-inlet ejector-nozzle installation. As part of this simulated auxiliary-inlet ejector-nozzle installation, faired elevon cutouts were used above the nacelles (fig. 6(b)). In such an installation, some of the auxiliary inlets would be exposed to the top wing flow field and the remainder to the underwing flow field. Because of the limitations of the model design, open auxiliary inlets were not used. Instrumentation details on the bent nacelle are shown in fig-

ure 6(e). The instrumentation on the open-nacelle configurations was brought out of the nacelles through the struts and through channels cut into the model wing. As a result, the open-nacelle configurations were instrumented near the aft end only. Twelve pressure orifices were located on the tapered section of the bent nacelles at four angular coordinate stations. These orifices were located at the centroid of equal annular areas; therefore, an integrated axial pressure drag could be calculated for this section. The boattails had a total of 16 orifices located at only two angular coordinate stations. Orifices were located at angular coordinate stations φ of 0° and 90° on the left nacelle (viewed in the upstream direction) and at 90° and 180° on the right nacelle. The integrated boattail pressure drag was then obtained by combining the orifices on the two angular coordinate stations from the nacelle under one wing with the orifices on the two angular coordinate stations from the nacelle under the other wing.

Figure 7 shows the details of the bulged bent-nacelle configuration. Schematic drawings of the nacelle installation under the wing are shown in figures 7(a) and (b). The nacelle and strut dimensions are shown in figure 7(c), and the instrumentation details are shown in figure 7(d). This nacelle was similar to the bent nacelle, but the inlet cowl and engine sections were replaced by a bulged section that simulated an engine accessory pod. The nacelle had an open spike inlet and simulated the nacelle geometry that would be necessary if this inlet and nozzle geometry were flight tested on the F-106 aircraft with the J-85/13 engine. The instrumentation on the nacelle was identical to that on the bent-nacelle configuration.

Figure 8 shows the details of the flared-nacelle configuration. These nacelles had open normal-shock inlets identical to those on the cylindrical and bulged nacelles shown in figure 5. The inlets were followed by a 3° axisymmetric cowl that extended back to the boattail juncture. The maximum diameter was therefore at the boattail juncture and was the same as that of the cylindrical nacelles, 3.145 centimeters. The 15° boattails were identical to those tested with the cylindrical nacelles. This nacelle geometry was investigated because it represented a configuration that was significantly different from the other nacelle geometries investigated. This nacelle had no cone shoulder or bend upstream of the boattail juncture. The length of these nacelles was adjusted to be similar to the ratio of length to maximum diameter of the bent-nacelle configurations, $l/d_{\max} = 4.9$. To investigate the effects of afterbody location with respect to the wing trailing edge, these nacelles were tested in two axial locations: with the base of the boattail 0.97 nacelle diameters aft of the wing trailing edge (fig. 8(a)) and in a more forward position with the base of the boattail aligned with the wing trailing edge (fig. 8(b)). The flared-nacelle dimensions are shown in figure 8(c), and the nacelles are shown installed on the model in the forward position in figure 8(d). Since these nacelles had open inlets, instrumentation could be installed only on the aft end (fig. 8(e)). Seven pressure orifices were installed on the nacelle body at four angular coordinate stations. The

boattail instrumentation was similar to that on the bent-nacelle configurations shown in figures 6 and 7.

Figure 9 shows the details of the fixed elevon cutouts used above the nacelles. The rectangular cutouts were used with the cylindrical and flared nacelles. The faired elevon cutouts were used with the bent nacelles to simulate a typical auxiliary-inlet ejector-nozzle installation.

Boundary-layer trips (figs. 2, 6(c), and 8(d)) were used to ensure that transition would occur forward on the nacelles. A 0.634-centimeter-wide strip of number-30 grit was attached from 2.54 to 5.08 centimeters aft of the leading edge of each nacelle. No grit was used on the model wing during the present series of tests.

RESULTS AND DISCUSSION

Boattail Pressure Drag

Figure 10 presents a comparison at Mach 0.9 of 15° boattail pressure coefficient distributions for isolated-nacelle conditions in the wind tunnel and installed-nacelle conditions in flight and on the 1/20-scale model. These results indicate a large installation effect that increased boattail pressures. In reference 2 it was felt that because of the limited instrumentation on the installed nacelle (16 orifices as compared with 70 on the larger isolated model), the low pressure which occurred just aft of the boattail shoulder was not properly accounted for in the boattail pressure integration. Consequently, an approximate correction was applied to the boattail drag results of reference 2 using the results from the isolated-nacelle tests. This correction tended to increase the measured drag coefficients especially at subsonic speeds. For the present series of tests, the boattail instrumentation was doubled such that eight pressure orifices were located along each angular coordinate station. Therefore, the low pressure near the shoulder was more adequately accounted for. Comparisons of the pressure distributions shown in figure 10 indicate that good agreement existed between all the installed nacelles, especially with the flight results. The boattail drag results from the present series of tests showed good agreement with the uncorrected results of reference 2. Also, as will be shown in figure 11, good agreement existed between the boattail drag coefficients obtained in flight and those measured on the wind tunnel model without any correction. Because of these results, no corrections were made to the data in this report.

A comparison of wind tunnel and flight boattail pressure-drag data for the 15° boattail nozzles is shown in figure 11 as a function of free-stream Mach number. The 1/20-scale model data were obtained at 2.5° angle of attack. The flight data shown vary in angle of attack dependent on Mach number from 3.6° at Mach 0.8 to 1.2° at Mach 1.3. Also, flight Reynolds number varied from 12×10^6 per meter at Mach 0.8 to 14×10^6 per

meter at Mach 1.3. To show the installation effect, data from the installed cylindrical nacelles with 10° conic forebodies are presented and compared with wind tunnel data from two isolated-nacelle models tested in the same facility: a 10.16-centimeter-diameter isolated nacelle without jet flow and a 21.48-centimeter-diameter cold-jet isolated nacelle. The 10.16-centimeter-diameter nacelle had a 10° conic forebody, a 15° boattail with a jet-boundary simulator, and the same length-to-diameter ratio as the installed nacelles. The appearance of this model was similar to the nacelle described in reference 5. The 21.48-centimeter-diameter cold-jet model had a strut-mounted cylindrical nacelle with a 15° boattailed nozzle and is described in reference 6. The data shown for this model were obtained with the cold-jet nozzle having an exit-to-local-static pressure ratio of 1.0. Also shown in figure 11 are flight data (ref. 4) and data from the 10.16-centimeter-diameter model under a rectangular flat-plate simulated wing (refs. 7 and 8). The flight data presented were obtained with a J-85 engine at maximum afterburning, which provided a nozzle-pressure ratio and area ratio such that the cylindrical ejector nozzle was overexpanded below Mach 1.0 and underexpanded above Mach 1.0. The simulated-wing test used the 10.16-centimeter-diameter nacelle previously described installed close to the lower surface of a large flat-plate rectangular wing. This test was a first attempt to investigate installation effects on larger-sized nacelles in the 8- by 6-Foot Supersonic Wind Tunnel with only portions of the wing and airframe present. This tunnel test technique, if perfected, offers the possibility of obtaining installation effects with larger nacelles than can be used on complete airframe models without exceeding wind tunnel blockage limitations.

The boattail drag data presented in figure 11 indicate that an installation of this type resulted in a significant decrease in drag when compared to isolated-nacelle results. The installed-boattail drag coefficients are low at the high subsonic Mach numbers, and the transonic drag rise was delayed to Mach 0.98. Similar results were reported in references 2 to 4. The flight and wind tunnel installed-nacelle drag data compare favorably at all speeds except near Mach 1.0, where the flight values indicate little or no installation effect when compared to isolated-nacelle results. In figure 11 it is also apparent that some of the drag reduction is obtained with just a flat-plate wing simulation, which provides a reflection plate for the nacelle flow field. The further decrease in afterbody drag seen at Mach 0.95 for the installed-nacelle flight and 1/20-scale model data was the additional result of the pressure gradients inherently produced by the lower-wing-surface curvature.

In general, these installation effects were caused by accelerations and recompressions in the combined flow fields of the wing and the nacelles, which resulted in high pressures on the boattail afterbodies, especially at the high subsonic speeds. These results are qualitatively demonstrated in the nacelle pressure distributions shown in reference 2 and the wing and nacelle pressure distributions shown in reference 3. These

results are supported by the detailed wing pressure distributions which are presented later in this report. As seen in figure 11, transonic terminal shocks were also present on the 10.16-centimeter-diameter nacelle, both isolated and installed under the flat-plate wing, and on the 21.48-centimeter-diameter cold-jet nacelle. However, since tunnel blockage causes a delay in terminal shock travel, the effects on afterbody drag were delayed to Mach 1.02 and 1.08, respectively.

The effects of changes in nacelle geometry on boattail drag of the 15° conical boattails at 2.5° angle of attack are presented in figure 12. Data for most of the nacelle geometries investigated are presented and compared to the isolated-nacelle results. The data from the open cylindrical and bulged nacelles are uncorrected data from the tests described in reference 2. As described previously, an approximate correction was applied to the boattail drag data presented in reference 2, which increased boattail drag at the subsonic speeds. The results of figure 12 indicate that the effects of nacelle geometry on the afterbody drag of the installed nacelles were rather small relative to the gross effect of the airframe installation. The exception was the flared-nacelle configuration, where the boattail drag was considerably increased, with coefficients similar in magnitude to the isolated-nacelle results. This was probably the result of the significant difference in the details of the inlet and cowl spillage around the forward portions of this nacelle in contrast to that of the others. This flared nacelle was a rather unusual transonic case in that no flow was spilled at the inlet. Most supersonic inlets are oversized in the transonic speed range and the resulting flow spillage would provide a flow field similar to that of the other nacelles. Also this nacelle had no cone-shoulder juncture upstream of the boattail juncture as did the cylindrical and bulged nacelles. With the flared-nacelle configuration, the afterbody drags between Mach numbers 0.85 and 0.95 were fairly constant and are also reduced when compared to isolated-nacelle results. This, as can be seen in the wing-pressure distributions, was the result of the wing transonic terminal shock being near the boattail. The effect of moving the boattail under the wing with the flared nacelles was increased boattail drag.

The effects of nacelle spanwise position on boattail drag are shown in figure 13 for the cylindrical nacelles with 10° conic forebodies at 2.5° angle of attack. The effect of increasing the nacelle position from 31 to 62 percent semispan is shown in figure 13(a) for the nacelle without an adjacent inboard nacelle. These data show that essentially the same installation effects were obtained at subsonic Mach numbers when the nacelle spanwise position was doubled. For low supersonic Mach numbers, the installed-boattail drag was further reduced from isolated-nozzle values as the nacelle was moved outboard. The effect of an adjacent inboard nacelle on outboard nacelle boattail drag is shown by comparing figures 13(a) and (b). At subsonic Mach numbers, the presence of an inboard nacelle had little effect on the outboard nacelle boattail drag. However, for low supersonic Mach numbers, boattail drag on the outboard nacelle increased when the

adjacent nacelle was installed. These values are closer to the values observed on the inboard nacelle alone. This was probably the result of obtaining similar reflecting conditions between the inboard nacelle and the fuselage as were obtained between the outboard and inboard nacelles. The effects of an adjacent outboard nacelle on inboard nacelle boattail drag were reported in reference 2 and can also be seen by comparing figures 13(a) and (b). The effects of an adjacent outboard nacelle on inboard nacelle boattail drag were small except between Mach numbers 0.95 to 1.05 and 1.36 to 1.46 where increased boattail drag was observed.

The effects of increasing angle of attack on boattail drag are shown in figure 14 for the cylindrical nacelles with 10° conic forebodies both at the inboard and outboard locations. The effects of increasing angle of attack were generally small for angles less than 8.5° . For angles greater than 8.5° , increasing angle of attack resulted in increased boattail drag. Similar results were observed for all other configurations. It must be noted however that at the higher angles of attack jet boundary simulators have not been adequately compared to real jet effects. Real jets tend to bend at high angles of attack and the effects on boattail drag may therefore be different.

The effect of nacelle forebody shape on boattail drag is shown in figure 15 for the solid cylindrical nacelles with 15° conic boattails at 2.5° angle of attack. Forebody shape had little effect on afterbody drag.

In figure 16 the effect of nacelle length on boattail drag is shown for the 15° boattails on the cylindrical nacelles with ogive forebodies at 2.5° angle of attack. Data are shown for two lengths of the cylindrical nacelles: 6.36 and 8.32 nacelle diameters. In general, the drag coefficients measured with the shorter nacelle were slightly lower than with the longer nacelle, except between Mach numbers 0.98 and 1.2. The largest difference in drag coefficient between the two nacelle lengths was seen at Mach 0.98. With the shorter nacelle, the transonic drag rise began slightly above Mach 0.95; however, with the longer nacelle, it began at Mach 0.98. This evidently was the result of the terminal shock on the shorter nacelle passing over the boattail at a lower Mach number than on the longer nacelle.

A comparison of the drag coefficients observed with the 15° , 20° , and 25° boattails mounted on the cylindrical nacelles with 10° conic forebodies is shown in figure 17 at 2.5° angle of attack. At subsonic Mach numbers, an increase in boattail angle resulted in an increase in boattail drag. However, at supersonic Mach numbers an increase in boattail angle had little effect on afterbody drag. These results, as can be seen in the afterbody pressure distributions, resulted from the installed afterbody flow separation characteristics. The 15° boattails generally showed no sign of flow separation except at Mach 1.0. The 20° boattails generally showed signs of flow separation at supersonic speeds on the inboard and bottom sides of the boattail. The 25° boattails showed signs of flow separation over most of the Mach numbers investigated. At supersonic speeds,

the flow separated from all sides of the 25° boattail, except the top surface close to the wing. Similar results were observed on the 20° and 25° boattails that were installed close to the rectangular-flat-plate simulated wing described in reference 8.

The boattail drag coefficients calculated by pressure integration of the 12 pressure orifices located on the 3° tapered section just upstream of the 15° boattail on the bent and bulged bent nacelles are shown in figure 18. These data indicate trends similar to those measured on the higher-angle boattails. The drag coefficients were low at subsonic Mach numbers and the transonic drag rise occurred between Mach numbers 0.90 and 0.95. The drag coefficients at supersonic Mach numbers were higher than at the subsonic Mach numbers but were much lower than those measured on the higher-angle boattails. As mentioned previously, the combined 3° tapered segment and 15° boattail of these nacelles were representative of a typical auxiliary-inlet ejector-nozzle installation. Therefore, it should be noted that these results might differ if open auxiliary inlets were present.

Wing Pressures

In figure 19 pressures on the upper and lower surface of the model wing are presented without nacelles for all Mach numbers investigated at 2.5° angle-of-attack. These data are presented as a function of model station for various wing spanwise position coordinate stations defined as the ratio of model spanwise station to wing semispan $2y/b$. The wing cross section at 31-percent semispan (the inboard nacelle location) is shown at the top of the figure. The model wing had a symmetrical NACA 0004-65 modified airfoil with the maximum thickness at the 50-percent chord station, and had a cambered leading edge. In figure 19 unpublished flight data are also presented for some Mach numbers. As mentioned previously, these flight data were obtained at various angles of attack dependent on Mach number, ranging from 4.3° at Mach 0.7 to 1.2° at Mach 1.2. These data are presented for only two wing position coordinate stations but the results were similar for the other spanwise coordinate stations. As seen in the 1/20-scale model data of figure 19, at the subsonic Mach numbers, a region of low pressure existed on both the upper and lower surface of the wing in the region aft of the wing maximum thickness and was followed by a recompression near the wing trailing edge. An increase in Mach number resulted in lower pressure in this region, especially on the wing lower surface, and was followed by a much stronger recompression further aft. Near Mach 0.95, this recompression had the characteristics of a terminal shock. At Mach 1.0, this shock had moved off the wing and the pressure remained low to the wing trailing edge. This result correlates with the sharp drag rise seen near Mach 0.98 on the nacelle afterbodies. As seen from the increased number of pressure orifices on the wing

lower surface, these effects extended over considerable regions of the wing in the spanwise direction. The comparisons shown in figure 19 between flight and model data indicate that generally favorable agreement existed both in pressure level and in the trends observed on the model with changes in Mach number.

In figure 20 pressures on the upper and lower surface of the wing are presented with the open bulged nacelles installed. Again data are presented for all the Mach numbers investigated at 2.5° angle of attack, and some comparisons with the flight data are made. Data at each Mach number investigated are again presented to serve as a comparison with the data in figure 19 without nacelles. Also, as mentioned previously, the open bulged nacelles were the scaled version of the nacelles being flight tested. A comparison of the pressures on the upper surface of the wing indicates little change resulted when the nacelles were installed, except for the pressures near the wing trailing edge, which were slightly lower at the subsonic Mach numbers with the nacelles installed. On the lower surface of the wing, however, with the nacelles installed at all Mach numbers a region of increased pressure occurred above the forward half of the cowl. The pressures above the center portion of the nacelle were generally lower than without the nacelle and, at the subsonic speeds, were followed by a stronger recompression region near the wing trailing edge. Again these effects spread in the spanwise direction over considerable regions of the wing lower surface. The higher pressures above the cowl resulted from the nacelle inlet cowl compression field impinging on the wing. Likewise the lower pressures above the center portion of the nacelle probably resulted from the expansion region generated by the cone-shoulder geometry of the cowl-nacelle juncture. The comparisons shown in figure 20 between flight and model data again indicate that favorable agreement generally existed between the two. As described in reference 4, this modification to the wing-lower-surface pressure distribution generated by the presence of the nacelles resulted in elevon trim changes at the high subsonic speeds.

The wing pressures obtained with the open cylindrical nacelles are presented in figure 21 at 2.5° model angle of attack for two representative Mach numbers (0.9 and 1.2). These pressures show trends similar to those seen with the open bulged nacelles. However, a comparison of figures 20(e) and 21(a) and figures 20(k) and 21(b) indicate that the presence of the bulge resulted in slight differences in the spanwise pressure distribution on the lower surface of the wing.

The effects of increasing model angle of attack on wing lower surface pressure distribution without and with nacelles are presented in figures 22 and 23, respectively. In these figures data are presented for two representative Mach numbers (0.9 and 1.2) and for two spanwise position coordinates ($2y/b = 0.264$ and 0.357). These spanwise position coordinates are just inboard and just outboard of the nacelle inboard spanwise station. The effects of increasing angle of attack on wing pressures without nacelles are seen in figure 22. In general, an increase in angle of attack resulted in an increase in wing

lower surface pressure except for the pressures near the aft edge of the wing at the subsonic Mach numbers. These particular pressures remained fairly constant over the range of angle of attack investigated. Similar effects were observed on the nacelle pressures with an increase in angle of attack, and some of these results are presented in reference 2. These results observed on both the wing and the nacelle pressures correlate with the results seen at subsonic Mach numbers on boattail drag, which was generally constant for angles of attack less than 8.5° . With the nacelles installed, as seen in figure 23, the effects of angle of attack on wing lower surface pressures were generally the same. At both subsonic and supersonic speeds, the pressures forward on the wing increased with increasing angle of attack, while those near the trailing edge were influenced to a lesser extent.

Wing-lower-surface pressure distributions with the bent nacelles, the flared nacelles (both aft and forward positions), and the cylindrical nacelles with the 6.1° , ogive, and 10° forebodies are presented in figures 24 to 28, respectively. All the nacelles were at the 31-percent semispan coordinate position. Data are presented in each figure for two representative Mach numbers at 2.5° angle of attack. As was expected, each nacelle configuration resulted in a slightly different wing-lower-surface pressure distribution; however, the same basic trends seen with the open bulged and cylindrical nacelles were still evident. The most markedly different pressure distribution were observed with the flared-nacelle configurations. With these nacelles, the low pressures seen aft of the wing maximum thickness were not as low as with the other nacelle configurations. This is probably because the surface of this type nacelle generates a flow compression field that extends from the inlet to the boattail juncture.

Fuselage Pressures

Pressure distributions on the aft region of the fuselage are presented in figure 29 both with and without the open bulged nacelles. Data are presented for all Mach numbers investigated at 0° angle of attack. For Mach numbers less than 0.95, the presence of the nacelles had little effect on the fuselage pressures. However, for Mach numbers above 0.95, the presence of the nacelles resulted in reduced fuselage pressure in the regions closest to the nacelles.

Nacelle and Boattail Pressures

In figure 30 and all subsequent figures, pressure coefficient data are presented from only the nacelle under the left wing since favorable agreement was observed be-

tween the left and right nacelle pressures. This agreement was true for all the configurations investigated. Also, in the following figures, for those angular coordinate stations on the left nacelle where instrumentation was not present, the data presented were obtained from the corresponding angular coordinate station on the nacelle under the right wing.

A comparison of unpublished F-106 flight nacelle and 1/20-scale-model nacelle pressures is presented in figure 30. The 1/20-scale-model nacelle was the closed bulged nacelle described in reference 2, which was a closed-inlet scaled version of the flight test nacelle. These model data were obtained during the tests described in reference 2; however, at that time the flight test results were not available. Therefore, these comparisons are made in this report. In figure 30 flight and model data are compared at four angular coordinate stations for three representative Mach numbers at 0° angle of attack. As seen in figure 30, favorable agreement was generally evident between the two sets of data. Some small differences can be seen forward on the nacelles, but these were probably due to differences in inlet spillage and to small differences in angle of attack of the aircraft. At subsonic speeds, larger differences in the pressures were evident at the boattail juncture. As mentioned previously, this was partly the result of the small number of boattail orifices used in the tests described in reference 2. This also resulted from a slight rounding of the boattail juncture that was generated because of the small scale of the model. The agreement in nacelle pressures seen here was also evident at all other Mach numbers.

A comparison of 15° boattail pressures from the F-106 flight tests and the 1/20-scale wind tunnel model tests is presented in figure 31. Data are again presented at four angular coordinate stations for three representative Mach numbers with the model at nominally 2.5° angle of attack. The model data presented were obtained with the cylindrical nacelles with 10° conic forebodies. The data from these nacelles are used because double the amount of instrumentation was installed on these nacelle afterbodies in contrast to the nacelles described in reference 2. Also presented in figure 31 are data from the 10.16-centimeter-diameter isolated nacelle. In figure 31, for the Mach numbers above and below Mach 1.0, the flight results show favorable agreement with the model results (except at the boattail juncture at subsonic speeds), and both sets of data are significantly increased above the pressures measured on the isolated nacelle. As already mentioned, the differences seen at the boattail juncture probably resulted from a slight rounding of the boattail juncture on the 1/20-scale model. At Mach 1.0, the flight data agreed more favorably with the isolated-nacelle results, while the model data still showed increased pressures. These differences were largest at the angular coordinate stations of 90° and 180° , where the model pressures indicate that the local flow might have been separated. These results correlate directly with the results for afterbody drag in figure 11. There good agreement was seen between flight and model re-

sults at all Mach numbers except Mach 1.0, where the installation effect on the flight data was small when compared to isolated-nacelle results. Some of the flight pressure distributions shown in figure 31 indicate that pressure disturbances existed on the boattails. This was later found to be caused by electrical noise pickup in the aircraft data and not by disturbances in the afterbody flow. Later flight tests with other boattails indicated this to be true and also indicated that the resulting boattail drag coefficients were not significantly affected by the electrical noise pickup. The favorable agreement between the flight and model results seen at Mach 0.9 and 1.2 also was evident at the other Mach numbers above and below Mach 1.0.

The effect of forebody shape on the solid cylindrical nacelle pressures is presented in figure 32. Data are presented for the three forebodies investigated at two representative Mach numbers (0.9 and 1.2) and at 2.5° angle of attack. As seen in figure 32, a change in forebody shape resulted in significant changes in the pressures over the forward portion of the nacelle but had little effect on the pressures over the aft portion of the nacelle and afterbody.

Pressure distributions on the solid cylindrical nacelles mounted at the outboard wing station (62 percent semispan) are shown in figures 33 and 34 without and with an adjacent inboard nacelle, respectively. These nacelles were tested with the 10° conic forebodies. A comparison of the data in figure 33 with the nacelle pressures shown in figure 32 for the same nacelle geometry mounted at the inboard wing spanwise station indicates that similar pressure distributions resulted when the nacelle spanwise station was doubled. Some slight differences are apparent, however, for the afterbody pressures at the supersonic speeds. These results generally correlate with the results seen for afterbody drag in figure 13, where at subsonic speeds drag remained the same when the spanwise position increased and at supersonic speeds it decreased. As seen in figure 34 the effect of an adjacent inboard nacelle on outboard nacelle pressures was to increase the circumferential pressure variations, especially at Mach 1.2. The largest differences are seen for the 45° and 90° angular coordinate stations.

In figure 35 pressures measured on the bent- and bulged-bent-nacelle configurations are presented. Data are again presented for two representative Mach numbers (0.9 and 1.2). Although some differences exist for the boattail pressures between the two configurations, the largest differences are seen on the tapered region upstream of the boattail at the 180° angular coordinate position. This difference evidently resulted from the bulge on the bottom. Again similar results were seen at the other Mach numbers.

In figure 36 pressures measured on the flared-nacelle configurations are presented for both the aft and forward mounting positions. Data are presented for two Mach numbers at 2.5° angle of attack. Data from the cylindrical nacelles with 15° boattails are also presented for comparison. As seen in figure 36, at both subsonic and supersonic Mach numbers, the boattail pressures on the flared-nacelles were generally lower than

those measured on the cylindrical nacelles. At subsonic speeds, the pressures upstream of the boattail juncture were comparable to those measured on the cylindrical nacelle and were generally higher at the supersonic speeds. The results seen on the boattail correlate directly with the boattail drag results seen in figure 12, where the boattail drags measured on the flared-nacelle configurations were considerably higher than those measured with the cylindrical nacelles. When the flared nacelle was mounted in the forward position with the boattail under the wing, the most notable effect on afterbody pressures was seen on the top of the boattail at the 0° angular coordinate position. For both subsonic and supersonic speeds, these pressures indicate that the flow was probably separated in the region between the boattail and lower surface of the wing.

The effect of increased boattail angle on afterbody pressures is presented in figure 37 for two Mach numbers at 2.5° angle of attack. The most predominant effect of increased boattail angle of afterbody pressures was to result in local regions of flow separation. No flow separation was noted for the 15° boattails except at Mach 1.0, as seen in figure 31(b) at the 90° and 180° angular coordinate stations. With the 20° boattails, flow separation occurred at all Mach numbers greater than 0.9. The separation observed was asymmetric, occurring only at the 90° and 180° angular coordinate stations. With the 25° boattails, flow separation occurred at all Mach numbers on all sides except on top at the 0° angular coordinate stations. Similar results were seen with 20° and 25° boattails tested on the 10.16-centimeter-diameter nacelle both isolated and under a flat-plate wing simulator and are presented in reference 8.

SUMMARY OF RESULTS

To further investigate airframe installation effects on engine nacelles and afterbodies at subsonic and supersonic speeds, tests were conducted in the Lewis Research Center 8- by 6-Foot Supersonic Wind Tunnel using a 1/20-scale model of the F-106 aircraft with simulated underwing engine nacelles. Boattail drag, nacelle pressures, and wing pressures were obtained on a series of configurations including changes in nacelle and inlet geometry and in nacelle location. Boattail drag was obtained with 15° , 20° , and 25° conical afterbodies and jet-boundary simulators. Data were obtained with and without inlet airflow through the nacelles over a Mach number range of 0.56 to 1.46 at angles of attack from 0° to 15° .

The following observations were made:

1. Airframe installation resulted in increased pressure on the wing lower surface near the nacelle forebody and decreased pressure on the cylindrical portion of the nacelle, followed by a stronger recompression near the wing trailing edge. These effects on the wing flow field combined with the effects on the nacelle flow field and terminal

shocks that appeared in both at high subsonic speeds resulted in reduced boattail drag coefficients at all Mach numbers when compared with isolated-nacelle results. The transonic boattail drag rise was delayed to Mach 0.98.

2. Good agreement was observed between flight and 1/20-scale-model wing and nacelle pressures. Good agreement was also observed between flight and 1/20-scale-model boattail drag results, except at Mach 1.0 where the installation effects on the flight-nacelle afterbody were small when compared with isolated-nacelle results.

3. Changes in inlet and nacelle geometry resulted in changed pressures on the wing lower surface and on the forward portions of the nacelles, but had little effect on boattail drag coefficient, except for a 3° flared-nacelle configuration where the installation effects were small when compared with isolated-nacelle results.

4. For subsonic Mach numbers, these favorable installation effects on boattail drag coefficient were generally insensitive to changes in nacelle spanwise position. For Mach numbers greater than 1.0, further reductions in boattail drag were observed when the nacelle was moved outboard either with or without an adjacent inboard nacelle.

5. Increased angle of attack resulted in increased pressures on the forward portion of the wing lower surface but generally had little effect on the pressures near the wing trailing edge. The corresponding effects on boattail drag coefficient were small for angles of attack less than 8.5° . For angles larger than 8.5° , increased angle of attack resulted in increased boattail drag.

6. Increased boattail angle resulted in local regions of afterbody flow separation particularly at supersonic Mach numbers. The corresponding boattail drag coefficients increased with boattail angle at subsonic Mach numbers but showed little effect at supersonic Mach numbers.

7. The presence of the nacelles generally resulted in reduced fuselage aft-end pressure for Mach numbers greater than 0.9.

Lewis Research Center,

National Aeronautics and Space Administration,

Cleveland, Ohio, November 13, 1969,

126-15.

REFERENCES

1. Nichols, Mark R.: Aerodynamics of Airframe-Engine Integration of Supersonic Aircraft. NASA TN D-3390, 1966.

2. Blaha, Bernard J. ; and Mikkelson, Daniel C. : Wind Tunnel Investigation of Airframe Installation Effects on Underwing Engine Nacelles at Mach Numbers From 0.56 to 1.46. NASA TM X-1683, 1968.
3. Blaha, Bernard J. ; Mikkelson, Daniel C. ; and Harrington, Douglas E. : Wind Tunnel Investigation of Installation Effects on Underwing Supersonic Cruise Exhaust Nozzles at Transonic Speeds. NASA TM X-52604, 1969.
4. Crabs, Clifford C. ; Boyer, Earle O. ; Mikkelson, Daniel C. : Engineering Aspect and First Flight Results of the NASA F-106 Transonic Propulsion Research Aircraft. NASA TM X-52559, 1968.
5. Shrewsbury, George D. : Effect of Boattail Juncture Shape on Pressure Drag Coefficients of Isolated Afterbodies. NASA TM X-1517, 1968.
6. Harrington, Douglas E. : Jet Effects on Boattail Pressure Drag of Isolated Ejector Nozzles at Mach Numbers From 0.60 to 1.47. NASA TM X-1785, 1969.
7. Shrewsbury, George D. : Effect of a Simulated Wing on the Pressure-Drag Coefficients of Various 15° Boattails at Mach Numbers From 0.56 to 1.00. NASA TM X-1662, 1968.
8. Harrington, Douglas E. : Effect of a Rectangular Simulated Wing on the Pressure-Drag Coefficient of Various Boattails at Mach Numbers From 0.60 to 1.47. NASA TM X-52609, 1969.

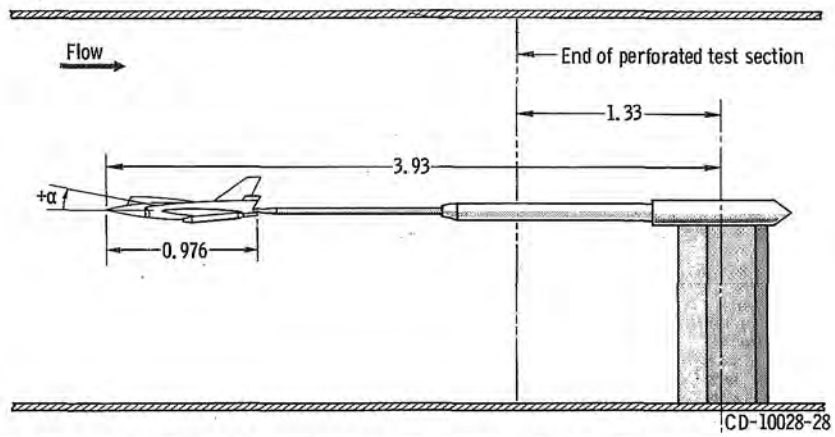


Figure 1. - Schematic drawing of model installation in transonic test section of 8- by 6-foot supersonic wind tunnel. Dimensions are in meters.

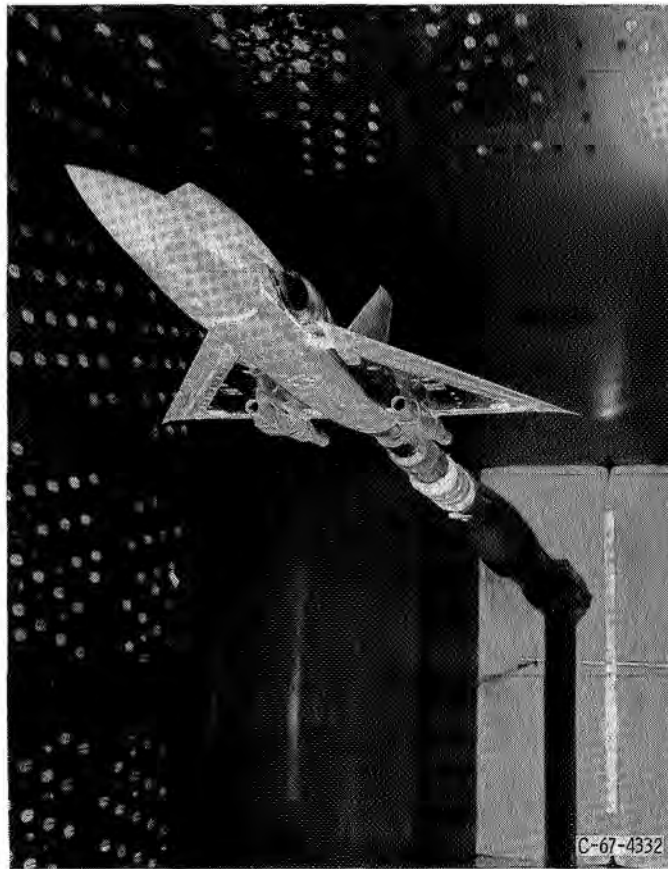
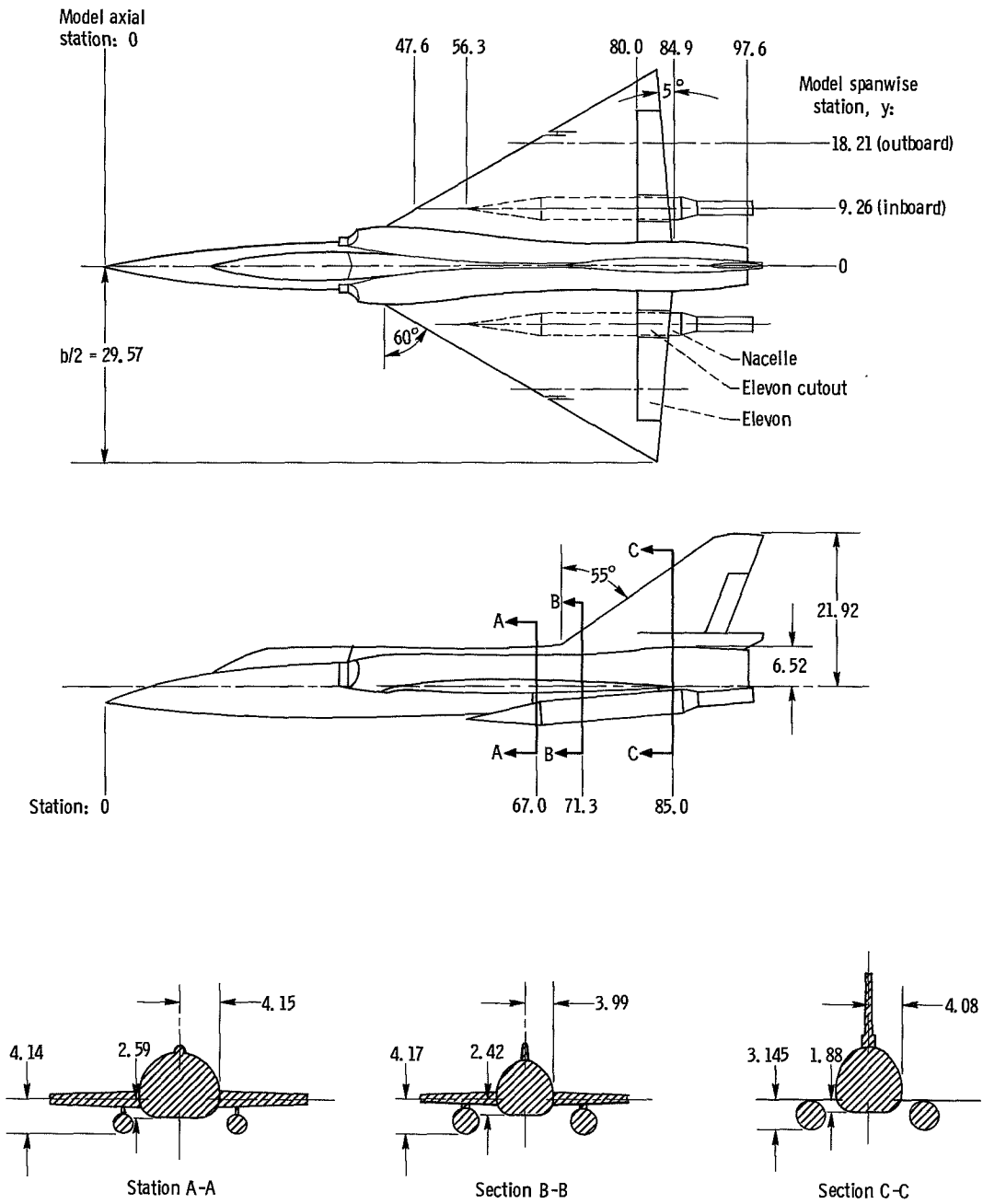


Figure 2. - Model installed in wind tunnel; open bulged nacelles.



(a) Model details and dimensions.

CD-10662-01

Figure 3. - Schematic drawing of model details and installation of nacelle under model wing. Dimensions are in centimeters.

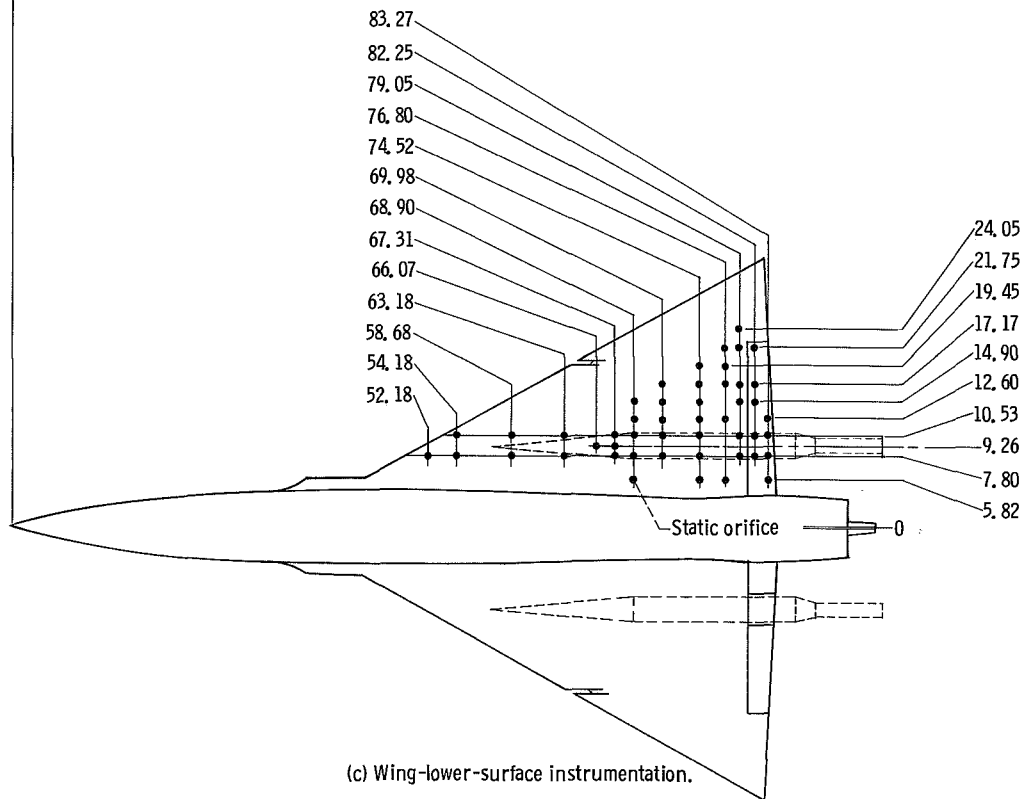
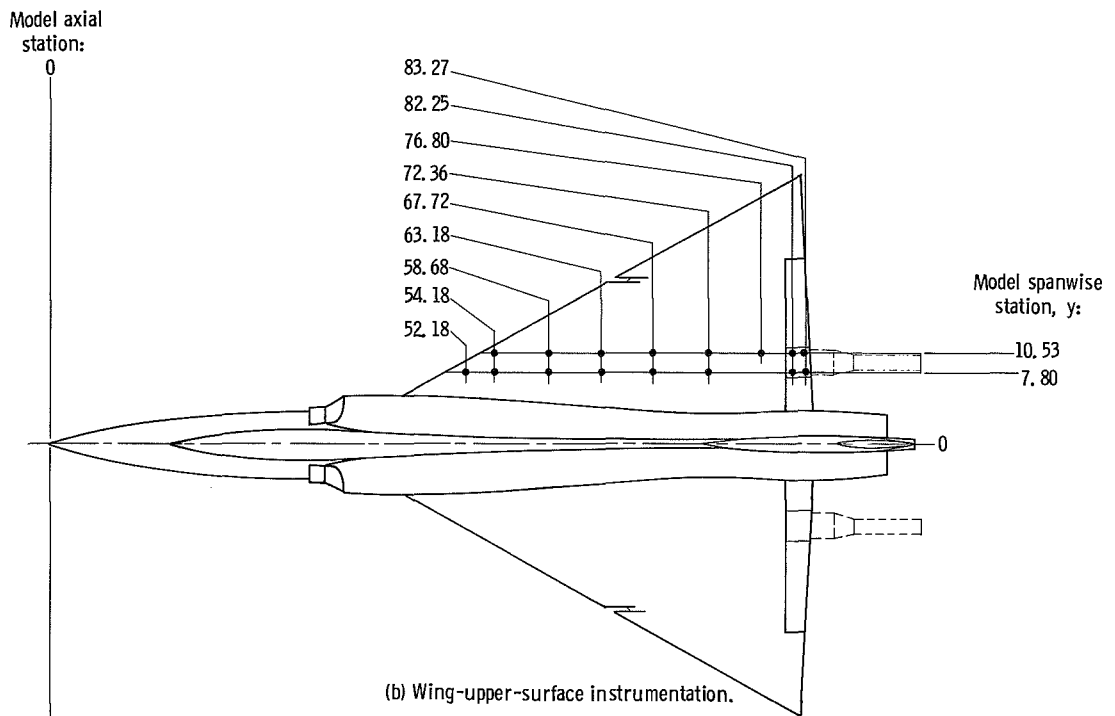
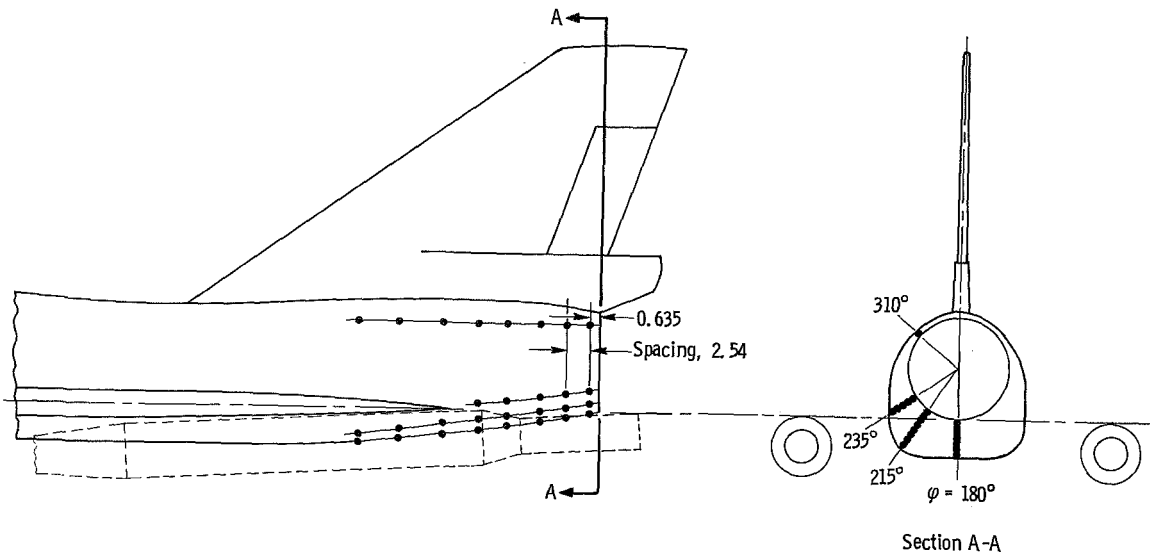
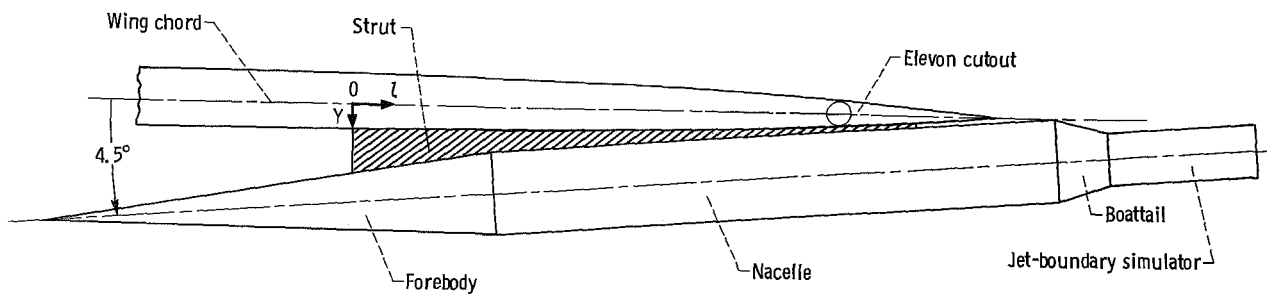


Figure 3. - Continued.

CD-10663-01



(d) Fuselage instrumentation.

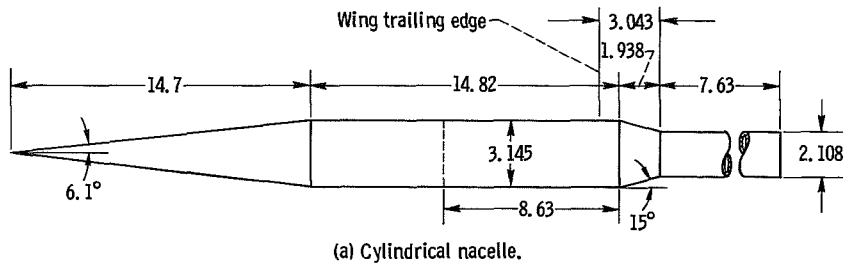


(e) Typical nacelle installation.

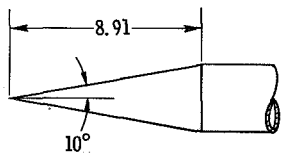
Wing-lower-surface coordinates, cm	
z	Y
0	0.708
4.81	.706
9.46	.602
14.08	.338
16.4	.154

Figure 3. - Concluded.

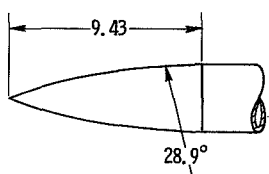
CD-10664-01



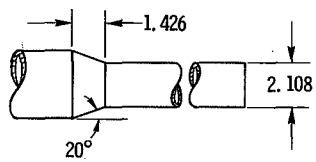
(a) Cylindrical nacelle.



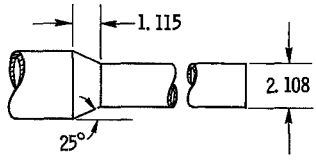
(b) 10° Forebody.



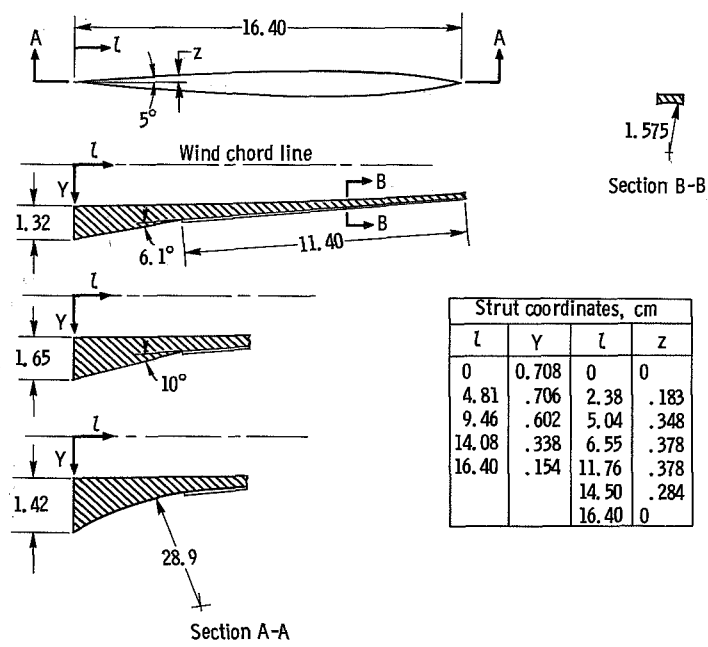
(c) Ogive forebody, $U/d_{max} = 3.0$.



(d) 20° Boattail.



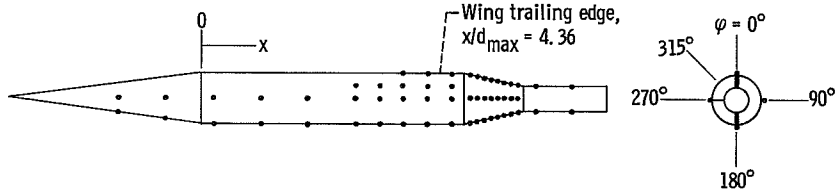
(e) 25° Boattail.



(f) Nacelle strut fairings.

CD-10665-01

Figure 4. - Details of solid nacelle configurations. Dimensions are in centimeters.

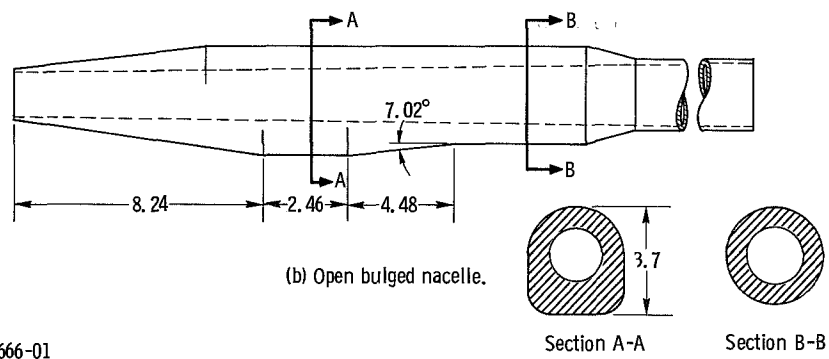
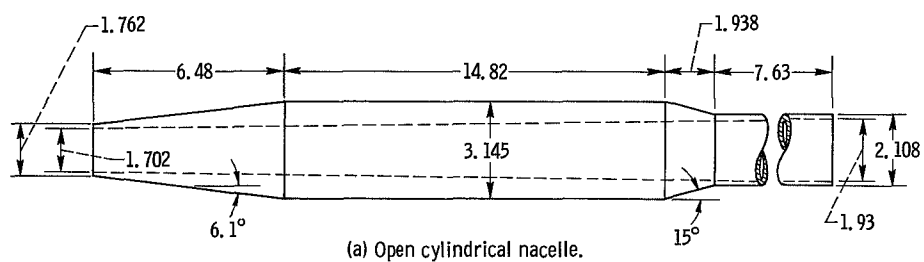


Instrumentation location	Nondimensional positional coordinate, x/d_{max}	Nacelle angular coordinate, φ , deg
Forebody	-1.416	*180, 270
	-.598	*180, 270
Nacelle body	0.218	*180, 270
	.921	*180, 270
	1.623	*180, 270
	2.344	*180, 270, 315
	3.071	*180, 270, 315
	3.704	0, 90, 180, 270, 315
	4.121	0, 90, 180, 270, 315
	4.540	0, 90, 180, 270, 315
15° Boattail	4.745	0, 180, 270
	4.820	↓
	4.89	
	4.955	
	5.030	
	5.110	
	5.190	
	5.290	
Jet-boundary simulator	5.537	
	5.941	0, 180
20° Boattail	4.740	0, 180, 270
	4.780	↓
	4.850	
	4.890	
	4.950	
	5.010	
	5.070	
	5.140	
Jet-boundary simulator	5.360	
	5.770	0, 180
25° Boattail	4.750	0, 180, 270
	4.815	↓
	4.880	
	4.950	
	5.020	
Jet-boundary simulator	5.260	
	5.670	0, 180

*Left nacelle only.

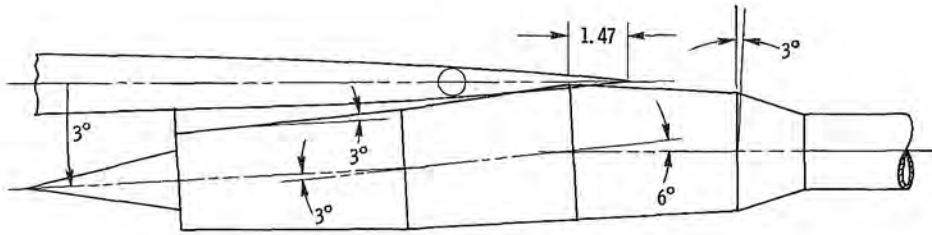
(g) Nacelle pressure instrumentation.

Figure 4. - Concluded.

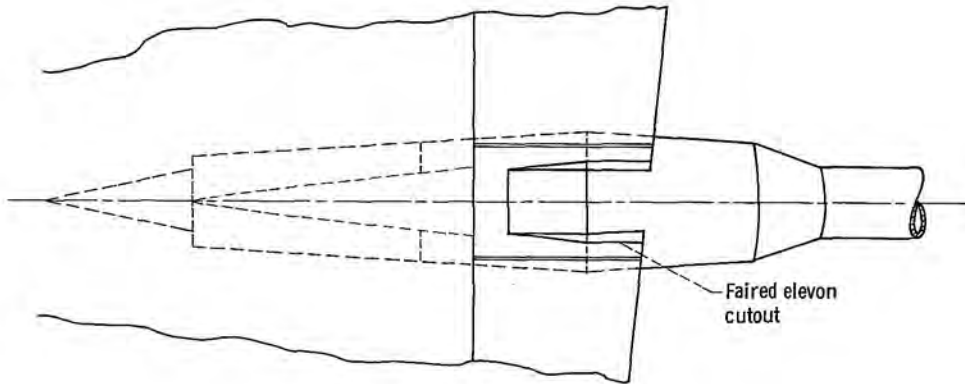


CD-10666-01

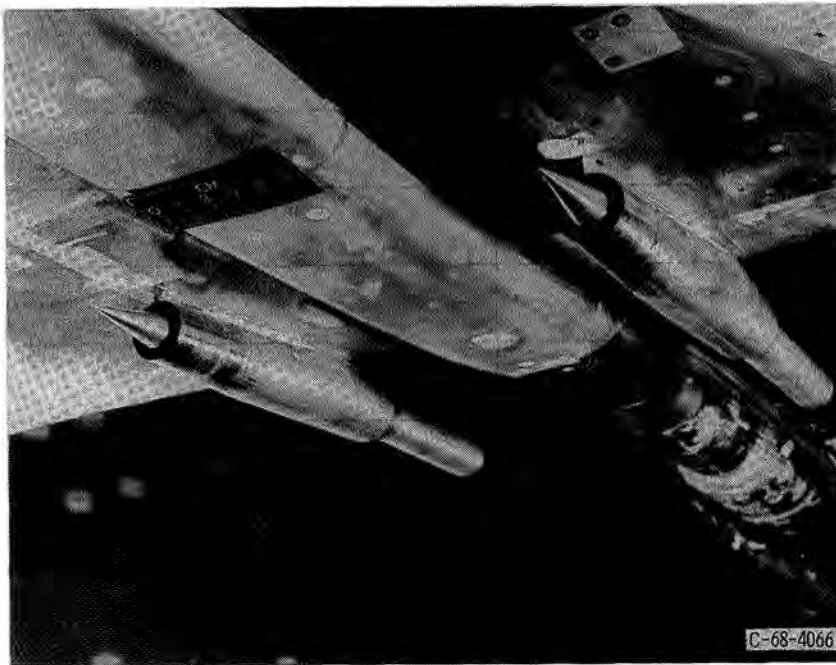
Figure 5. - Details of basic open nacelle configuration. Dimensions are in centimeters.



(a) Installation under wing, side view.

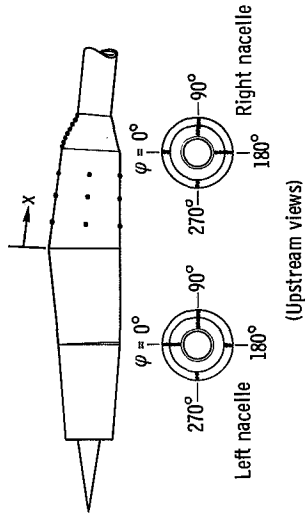


(b) Installation under wing, plan view.



(c) Installed on model.

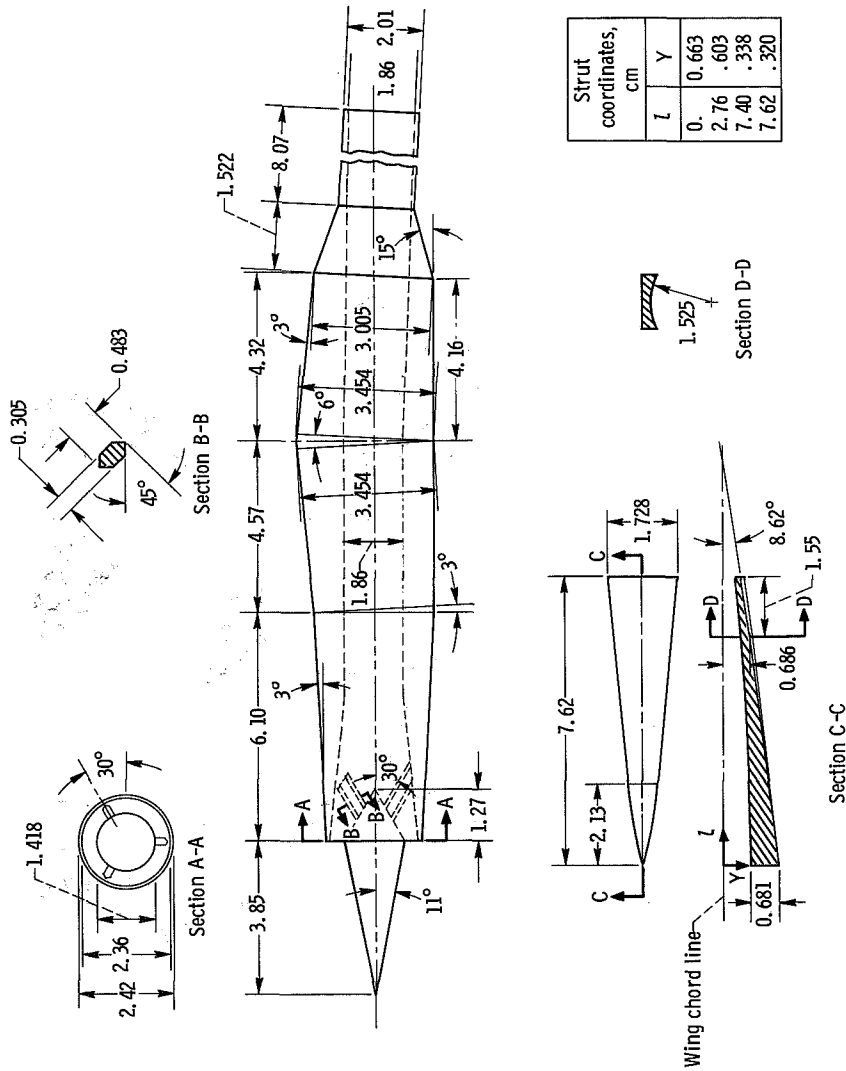
Figure 6. - Details of bent-nacelle configuration. Dimensions are in centimeters.



(Upstream views)

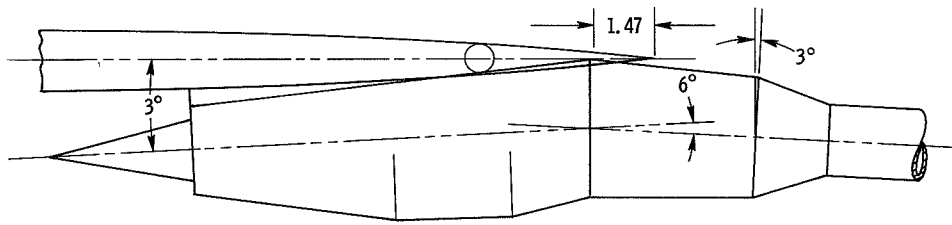
Instrumentation location	Nondimensional position coordinate, x/d max	Nacelle angular coordinate, ψ , deg
Nacelle body (both nacelles)	0.197	0, 90, 180, 270
	.61	0, 90, 180, 270
15° Boattail (left nacelle)	1.03	0, 90, 180, 270
	1.27	0, 90
	1.32	
	1.37	
	1.42	
	1.49	
15° Boattail (right nacelle)	1.53	90, 180
	1.59	
	1.66	
	1.27	
	1.32	
	1.37	

(e) Nacelle pressure instrumentation.

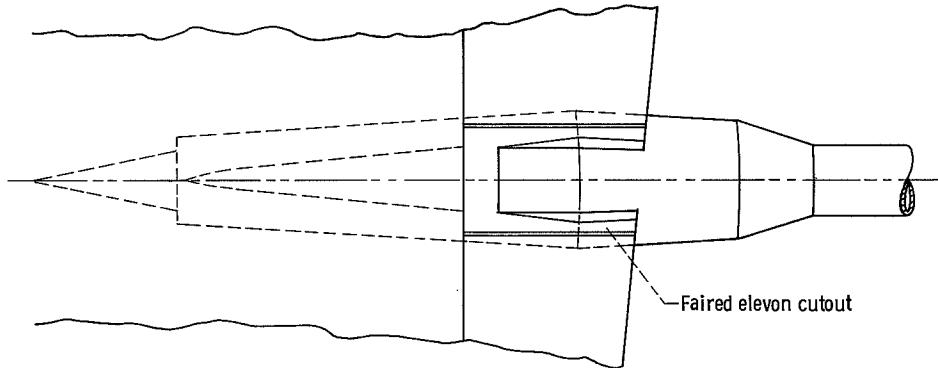


(d) Nacelle and strut fairing dimensions.

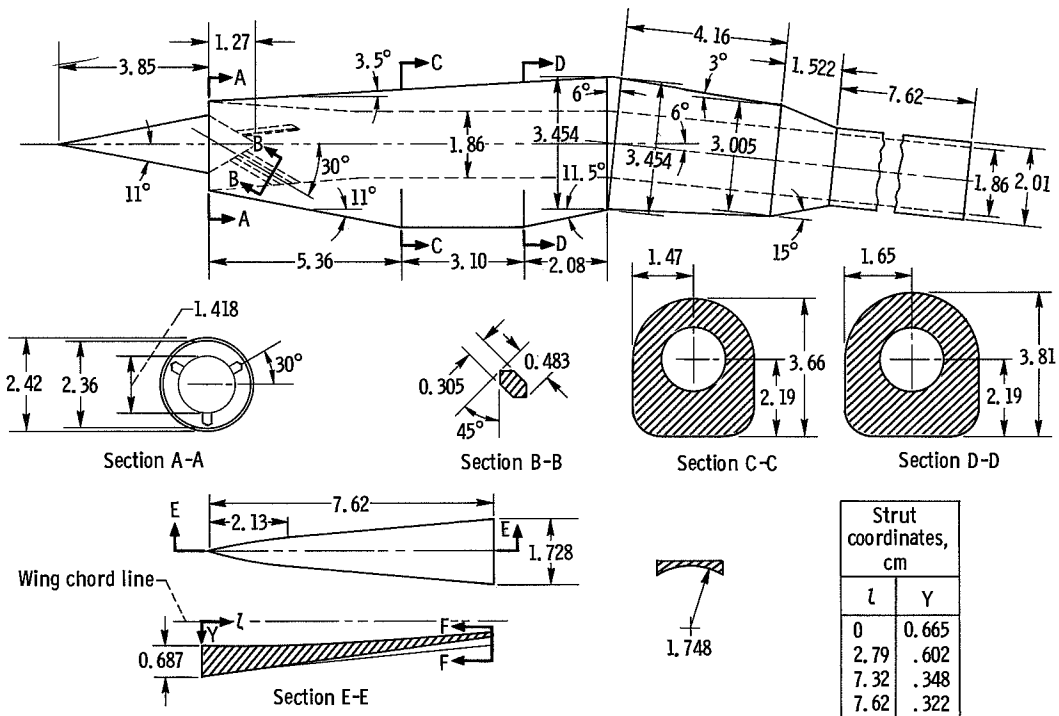
Figure 6. - Concluded.



(a) Installation under wing, side view.



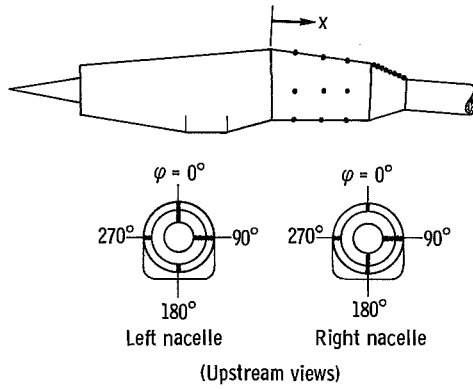
(b) Installation under wing, plan view.



(c) Nacelle and strut fairing dimensions.

CD-10668-01

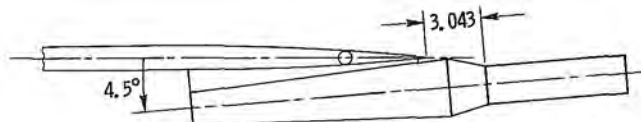
Figure 7. - Details of bulged-bent-nacelle configuration. Dimensions are in centimeters.



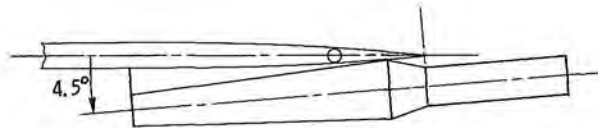
Instrumentation	Nondimensional position coordinate, x/d_{max}	Nacelle angular coordinate, ϕ , deg
Nacelle body (both nacelles)	0.197	0, 90, 180, 270
	.61	0, 90, 180, 270
	1.03	0, 90, 180, 270
15° Boattail (left nacelle)	1.27	0, 90
	1.32	↓
	1.37	
	1.42	
	1.49	
	1.53	
	1.59	
1.66		
15° Boattail (right nacelle)	1.27	90, 180
	1.32	↓
	1.37	
	1.42	
	1.49	
	1.53	
	1.59	
1.66		

(d) Nacelle pressure instrumentation.

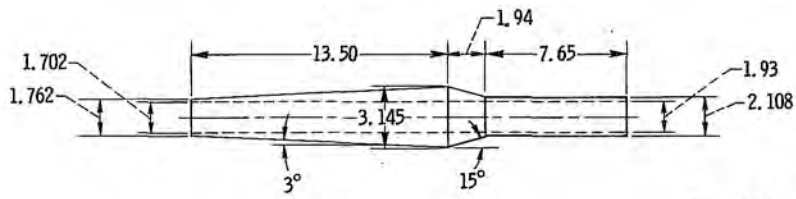
Figure 7. - Concluded.



(a) Aft position.

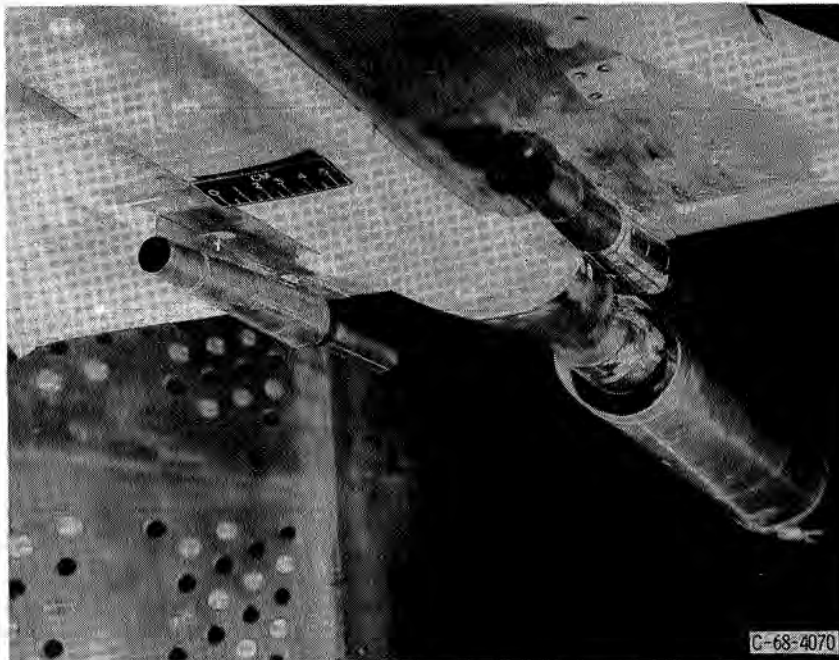


(b) Forward position.



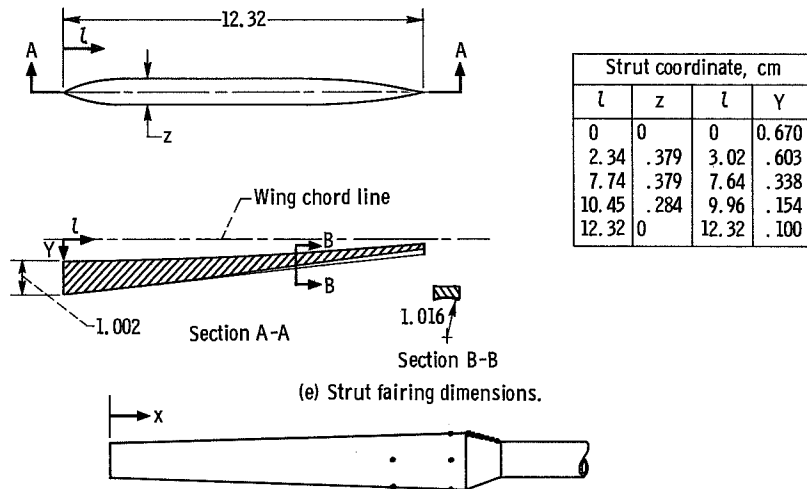
CD-10670-01

(c) Dimensions; nacelle length-to-diameter ratio, $l/d_{max} = 4.9$.

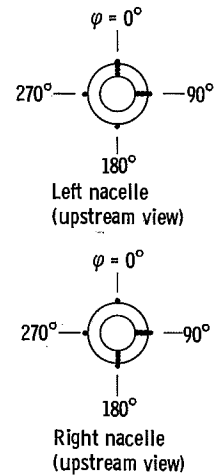


(d) Installed on model; forward position.

Figure 8. - Details of flared nacelle configuration. Dimensions are in centimeters.



Instrumentation location	Nondimensional position coordinate, x/d_{max}	Nacelle angular coordinate, φ , deg
Nacelle body (both nacelles)	3.275 4.120	90, 180, 270 0, 90, 180, 270
15° Boattail (left nacelle)	4.325 4.390 4.460 4.560 4.610 4.685 4.770 4.860	0, 90
15° Boattail (right nacelle)	4.325 4.390 4.460 4.560 4.610 4.685 4.770 4.860	90, 180



(f) Nacelle pressure instrumentation.

Figure 8. - Concluded.

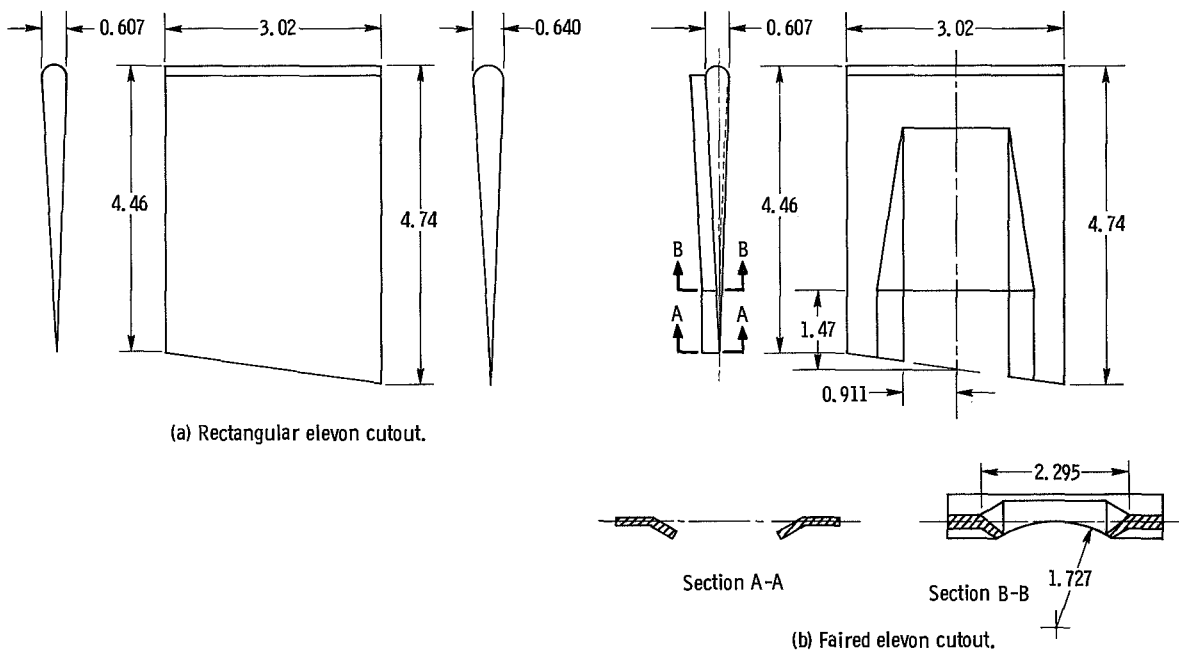
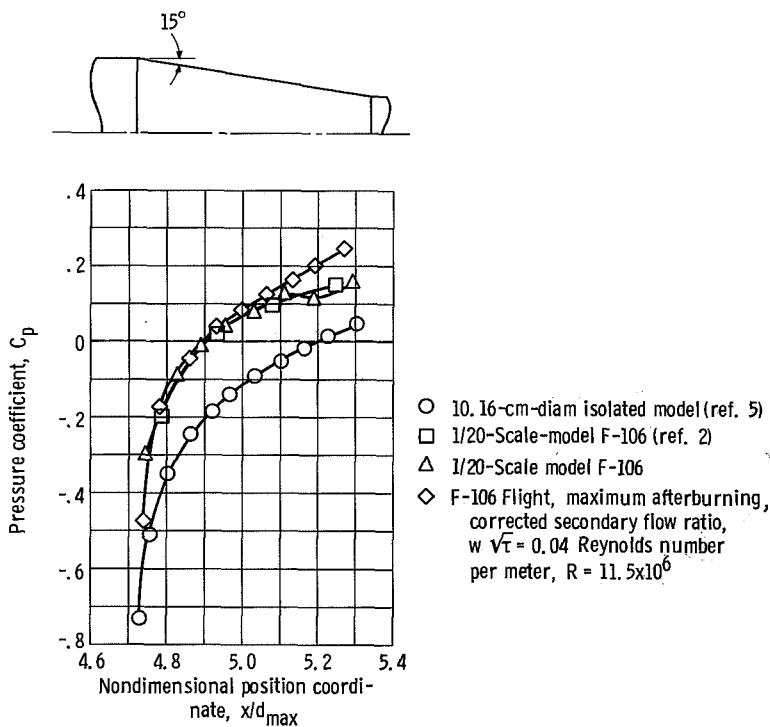


Figure 9. - Details of fixed elevon cutouts. Dimensions are in centimeters.



CD-10669-01

Figure 10. - Comparison of installed-nacelle boattail pressure distributions with data from a 10.16-centimeter-diameter isolated model. Mach 0.9; angle of attack, 0°; angular coordinate station, 270°.

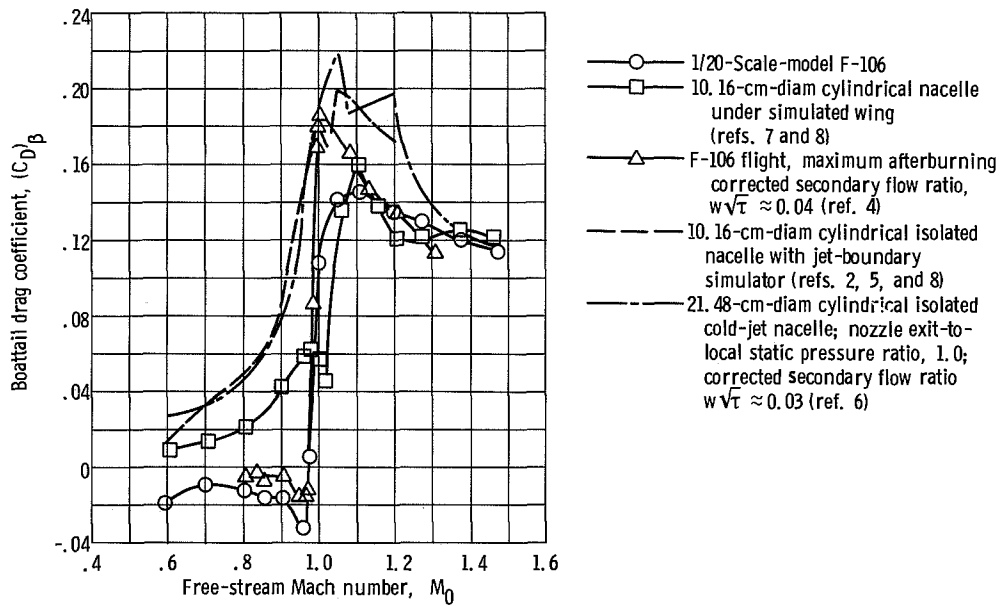


Figure 11. - Installation effect on 15° conical boattail drag coefficient; cylindrical nacelle with 10° conic forebody at 2.5° angle of attack.

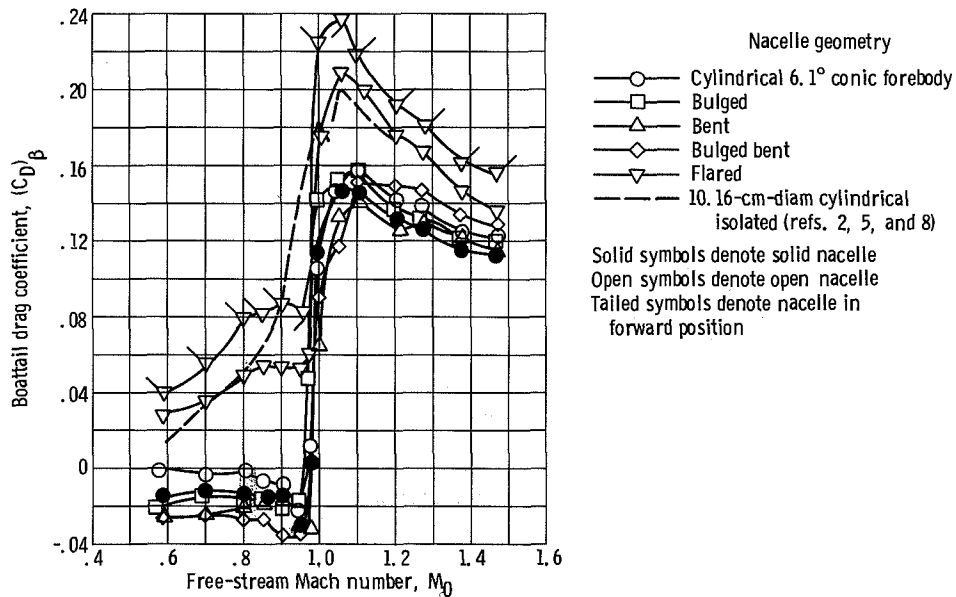


Figure 12. - Effect of nacelle geometry on 15° conical boattail drag coefficient. Angle of attack, 2.5° .

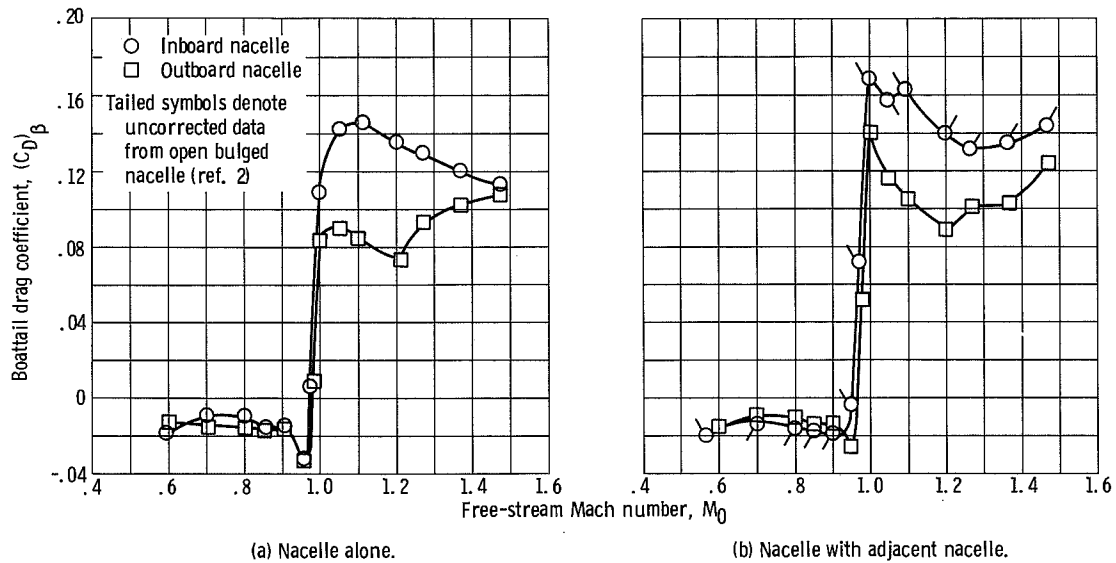


Figure 13. - Effect of nacelle spanwise position on 15° conical boattail drag coefficient. Cylindrical nacelle with 10° conic forebody, angle of attack, 2.5° .

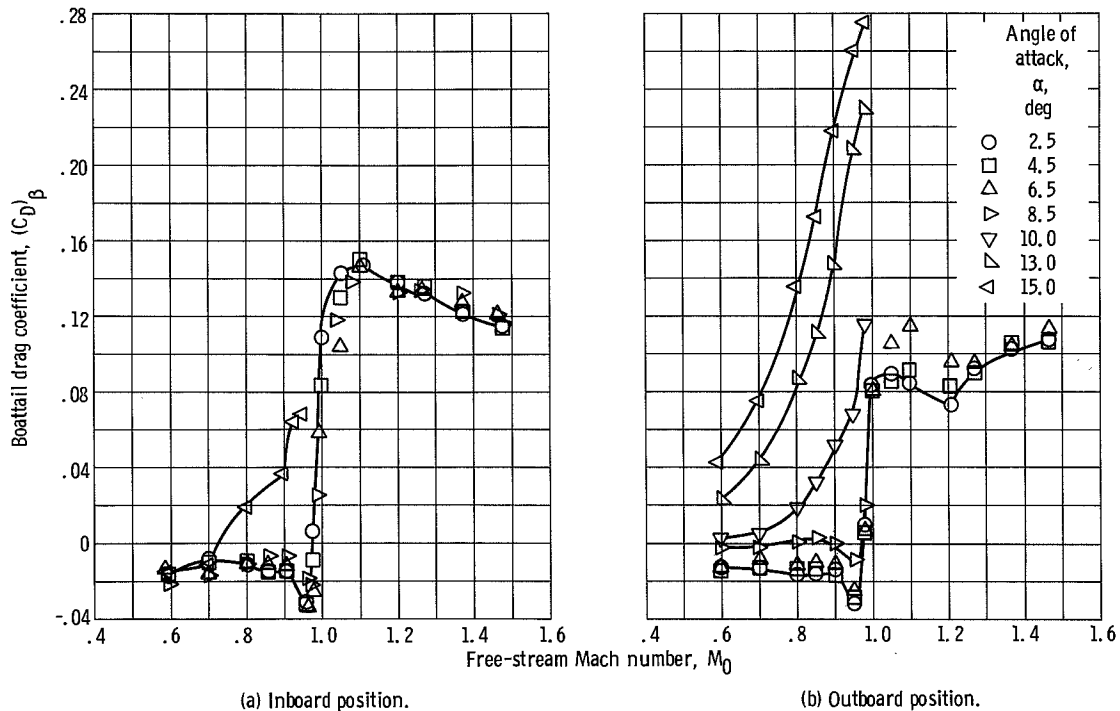


Figure 14. - Effect of angle of attack on 15° conical boattail drag coefficient. Cylindrical nacelle with 10° conic forebody.

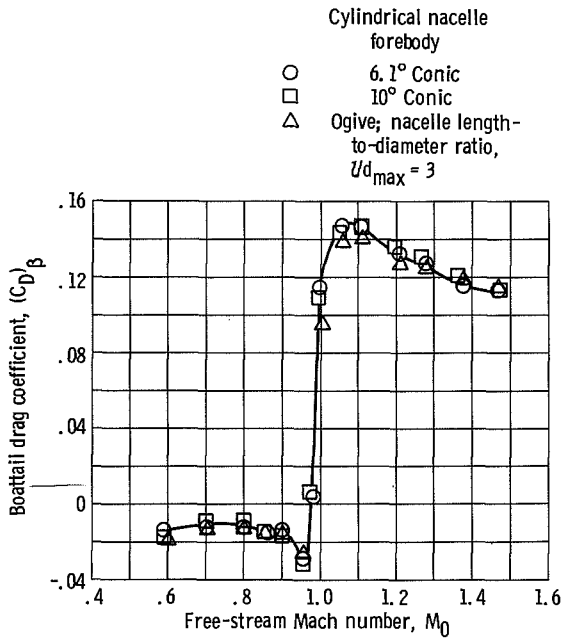


Figure 15. - Effect of cylindrical-nacelle-forebody shape on 15° conical boattail drag coefficient. Angle of attack, 2.5°.

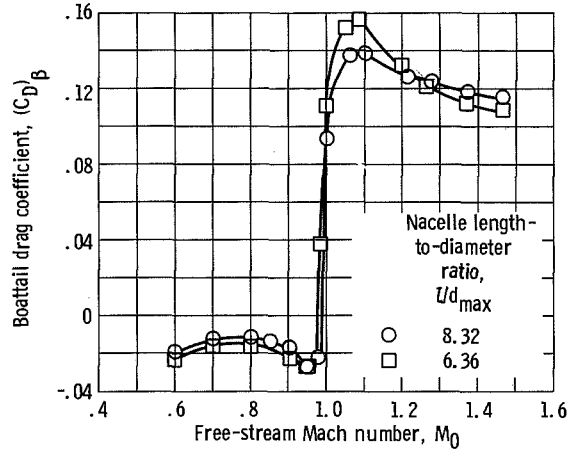


Figure 16. - Effect of nacelle length on 15° conical boattail drag coefficient. Cylindrical nacelle with ogive forebody; angle of attack, 2.5°.

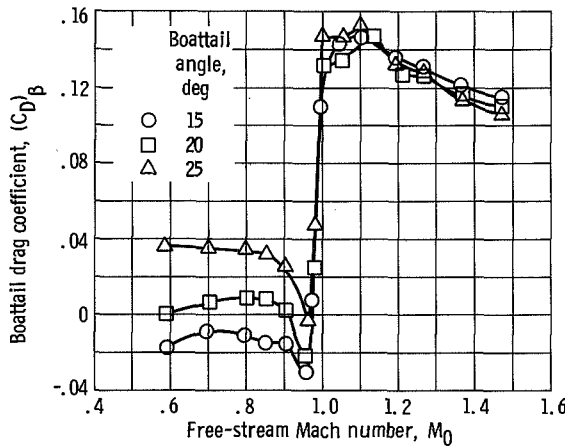


Figure 17. - Effect of increased boattail angle on boattail drag coefficient. Cylindrical nacelle with 10° conic forebody; angle of attack, 2.5°.

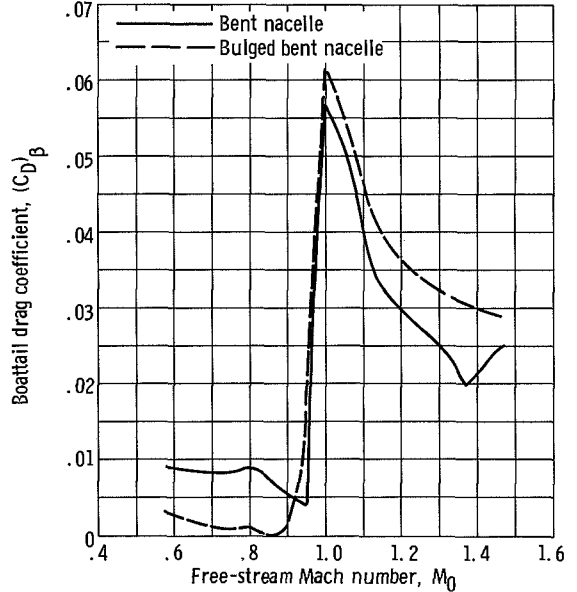
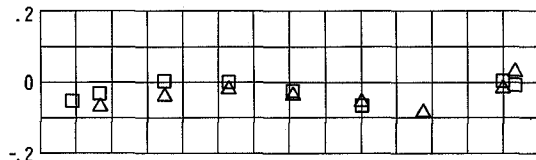


Figure 18. - Boattail drag coefficient on 3° tapered region just upstream of the 15° boattails on the bent nacelles. Angle of attack, 0°.

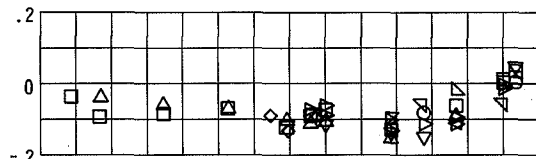
Position coordinate, $2y/b$

- 0.197
- .264
- ◇ .313
- ◇ .357
- ▽ .427
- ▽ .505
- △ .581
- ▽ .658
- ▽ .737
- ▽ .815

--- Flight, $2y/b = 0.271$
 — Flight, $2y/b = 0.366$

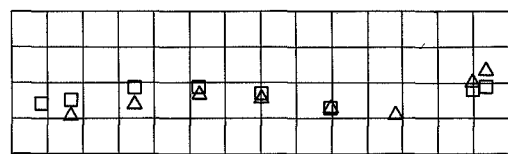


(a-1) Upper surface.

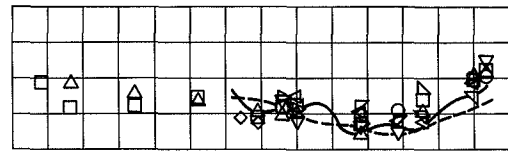


(a-2) Lower surface.

(a) Free-stream Mach number, $M_0 = 0.6$.

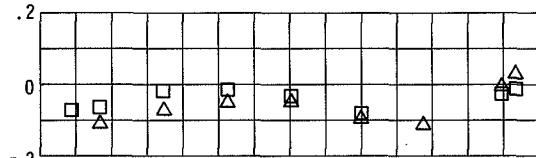


(b-1) Upper surface.

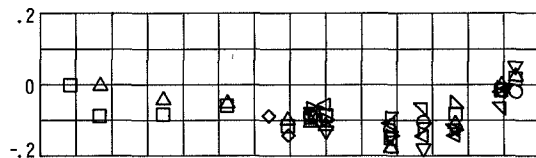


(b-2) Lower surface.

(b) Free-stream Mach number, $M_0 = 0.7$.

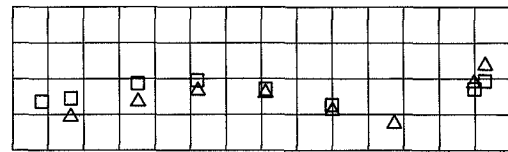


(c-1) Upper surface.

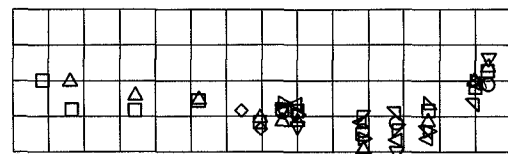


(c-2) Lower surface.

(c) Free-stream Mach number, $M_0 = 0.8$.



(d-1) Upper surface.



(d-2) Lower surface.

(d) Free-stream Mach number, $M_0 = 0.85$.

Figure 19. - Wing pressure distribution without nacelles. Angle of attack, 2.5° .

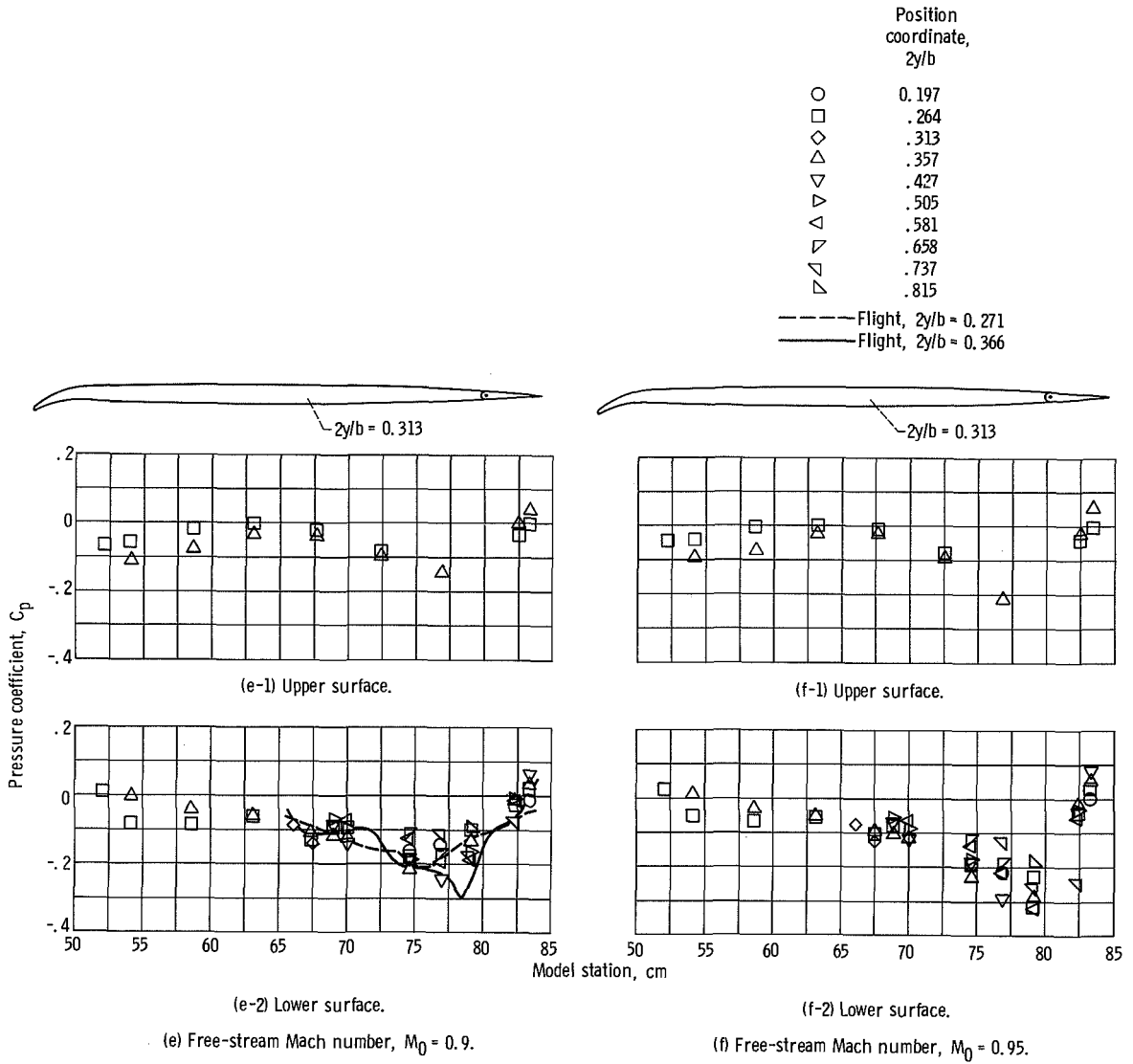


Figure 19. - Continued.

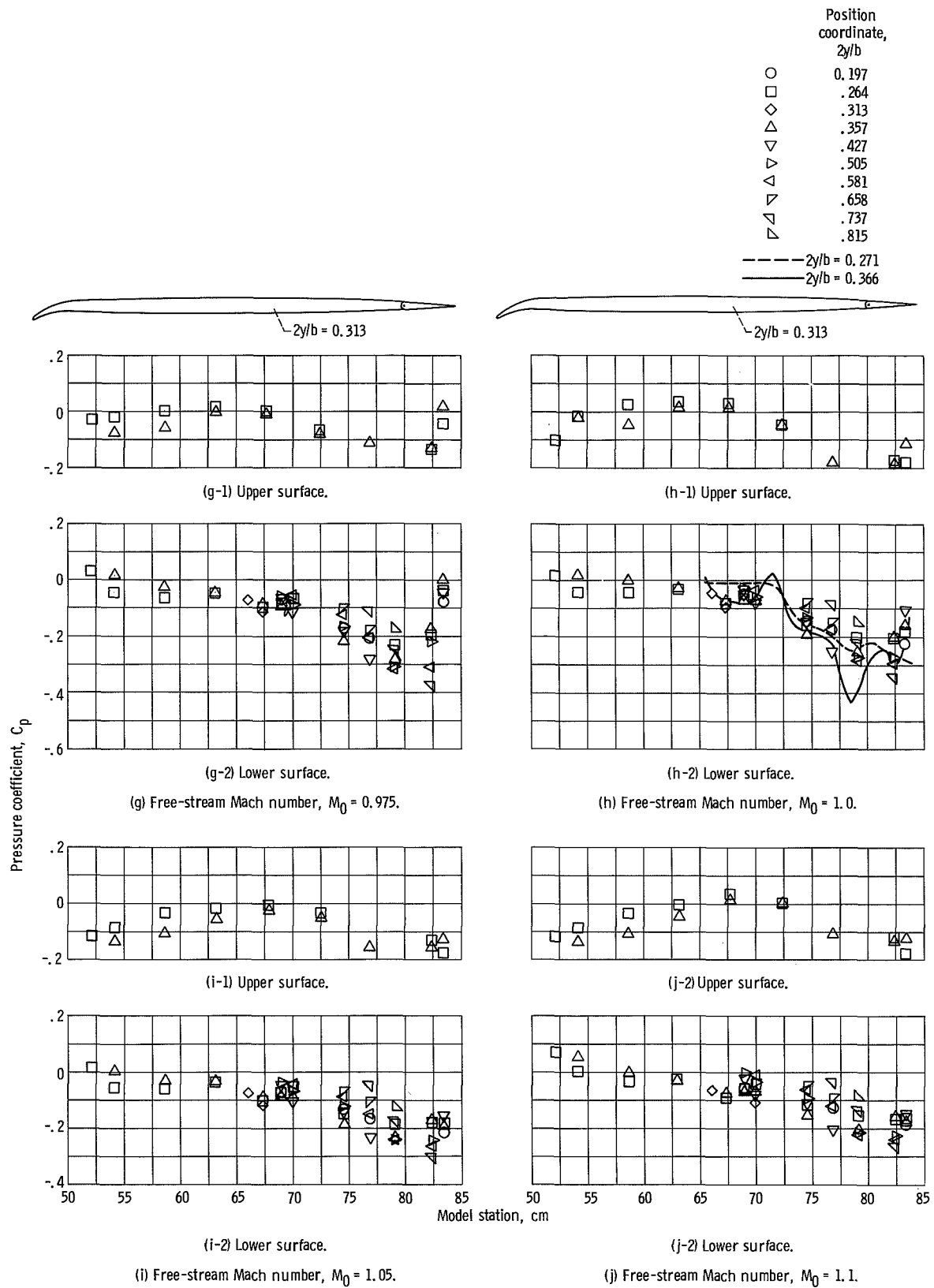


Figure 19. - Continued.

Position coordinate, $2y/b$

- 0.197
- .264
- ◇ .313
- △ .357
- ▽ .427
- ▽ .505
- △ .581
- ▽ .658
- ▽ .737
- ▽ .815

--- Flight, $2y/b = 0.271$
 — Flight, $2y/b = 0.366$

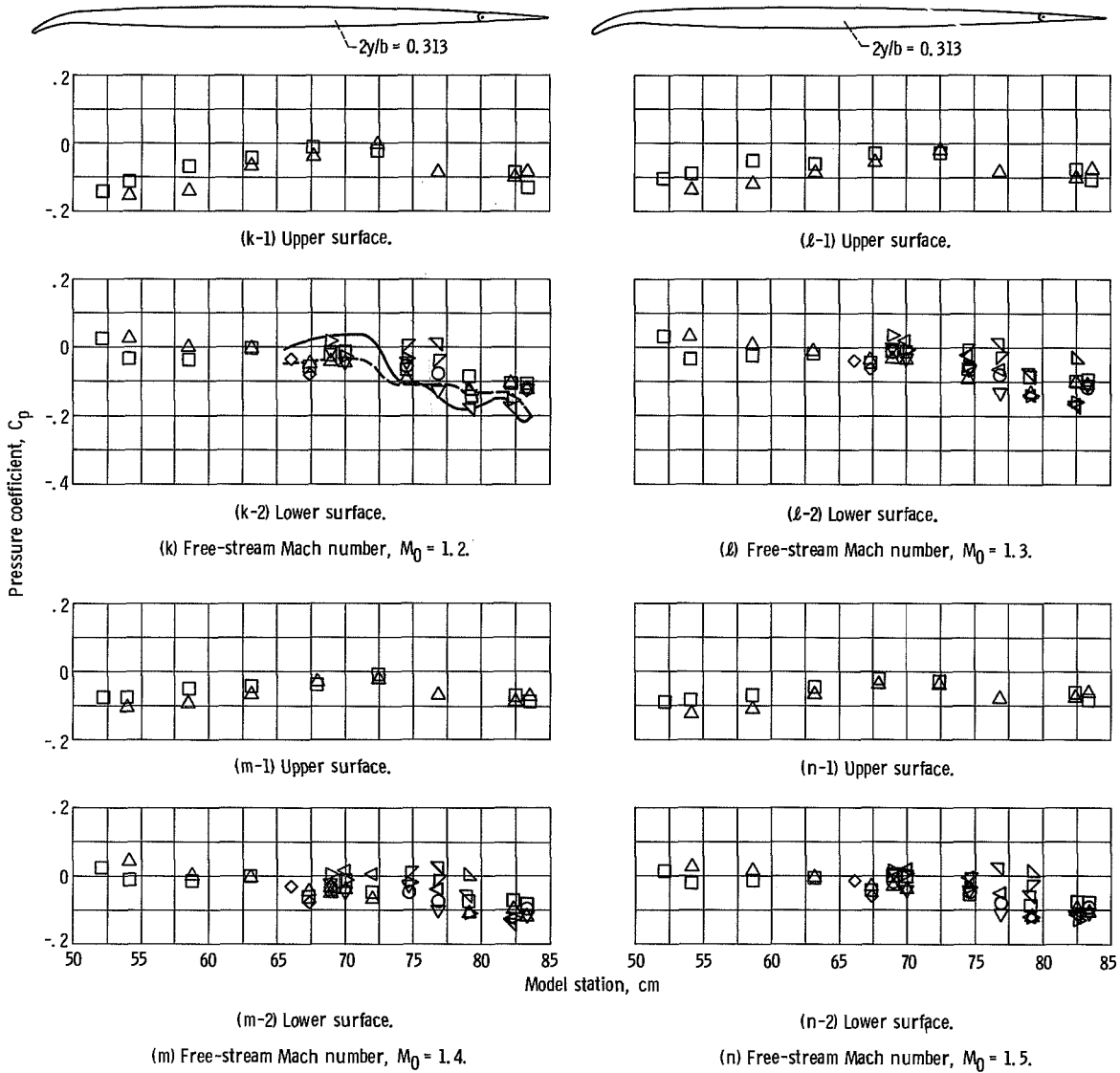
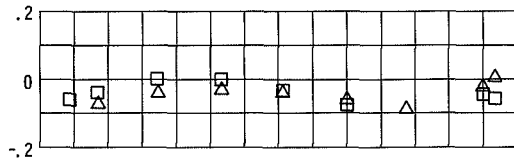
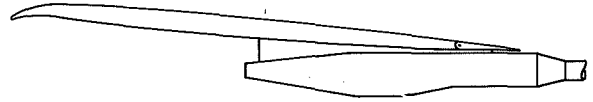
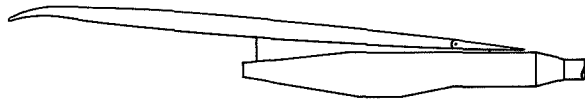


Figure 19. - Concluded.

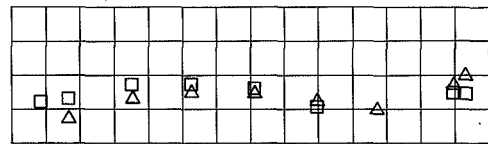
Position coordinate, $2y/b$

○	0.197
□	.264
◇	.313
△	.357
▽	.427
△	.505
▽	.581
△	.658
▽	.737
△	.815

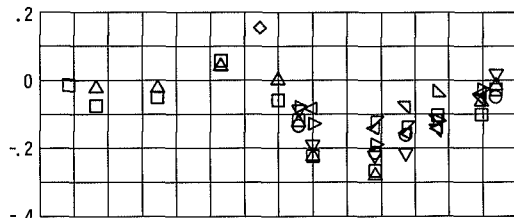
--- Flight, $2y/b = 0.271$
 --- Flight, $2y/b = 0.366$



(a-1) Upper surface.

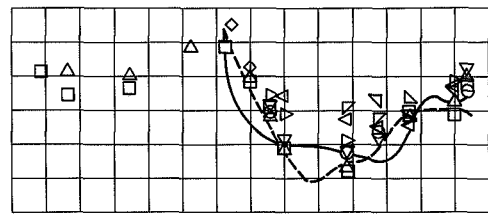


(b-1) Upper surface.



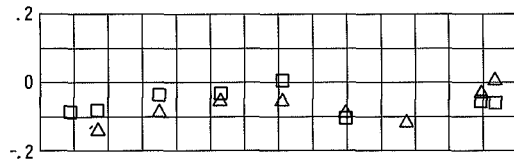
(a-2) Lower surface.

(a) Free-stream Mach number, $M_0 = 0.6$.

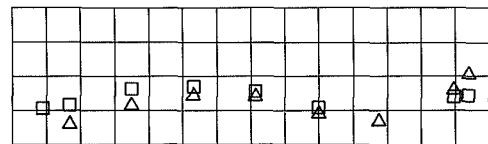


(b-2) Lower surface.

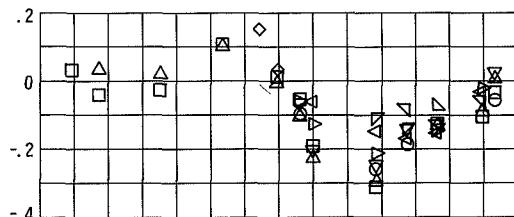
(b) Free-stream Mach number, $M_0 = 0.7$.



(c-1) Upper surface.

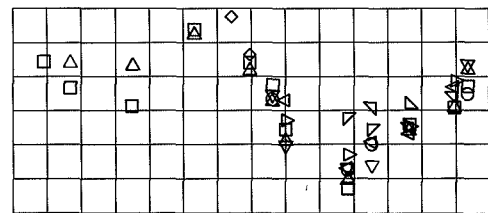


(d-1) Upper surface.



(c-2) Lower surface.

(c) Free-stream Mach number, $M_0 = 0.8$.



(d-2) Lower surface.

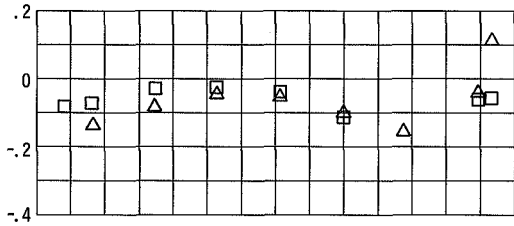
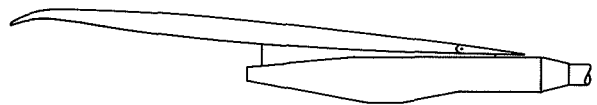
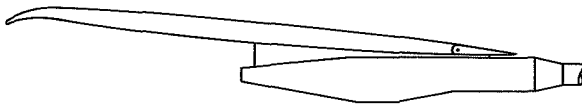
(d) Free-stream Mach number, $M_0 = 0.85$.

Figure 20. - Wing pressure distribution with open bulged nacelle. Angle of attack, 2.5° .

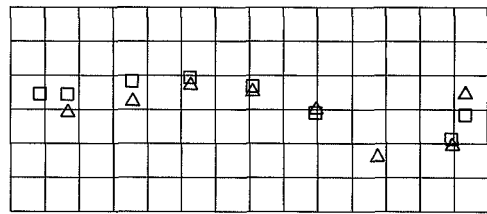
Position
coordinate,
 $2y/b$

- 0.197
- 0.264
- ◇ 0.313
- △ 0.357
- ▽ 0.427
- ▽ 0.505
- ▽ 0.581
- ▽ 0.658
- ▽ 0.737
- ▽ 0.815

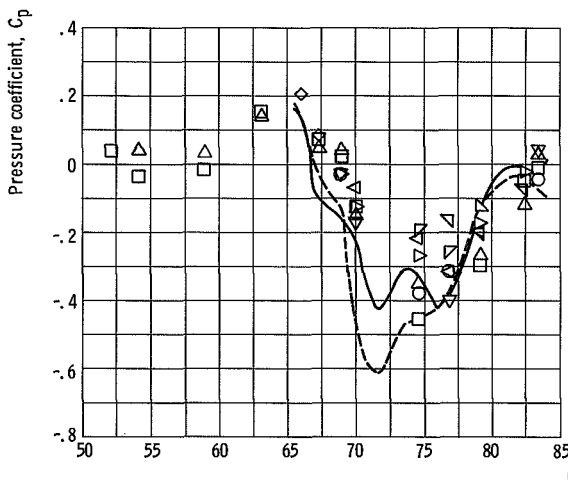
--- Flight, $2y/b = 0.271$
 — Flight, $2y/b = 0.366$



(e-1) Upper surface.

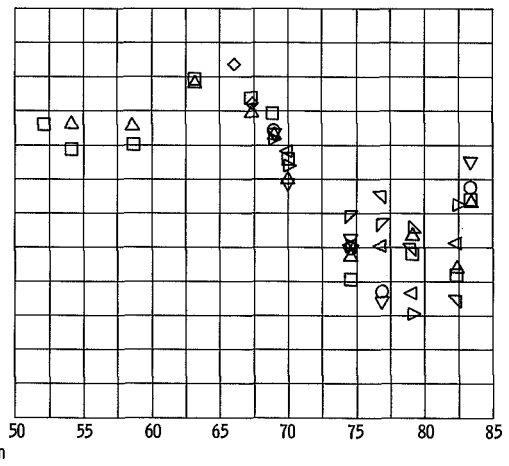


(f-1) Upper surface.



(e-2) Lower surface.

(e) Free-stream Mach number, $M_0 = 0.9$.



(f-2) Lower surface.

(f) Free-stream Mach number, $M_0 = 0.95$.

Figure 20. - Continued.

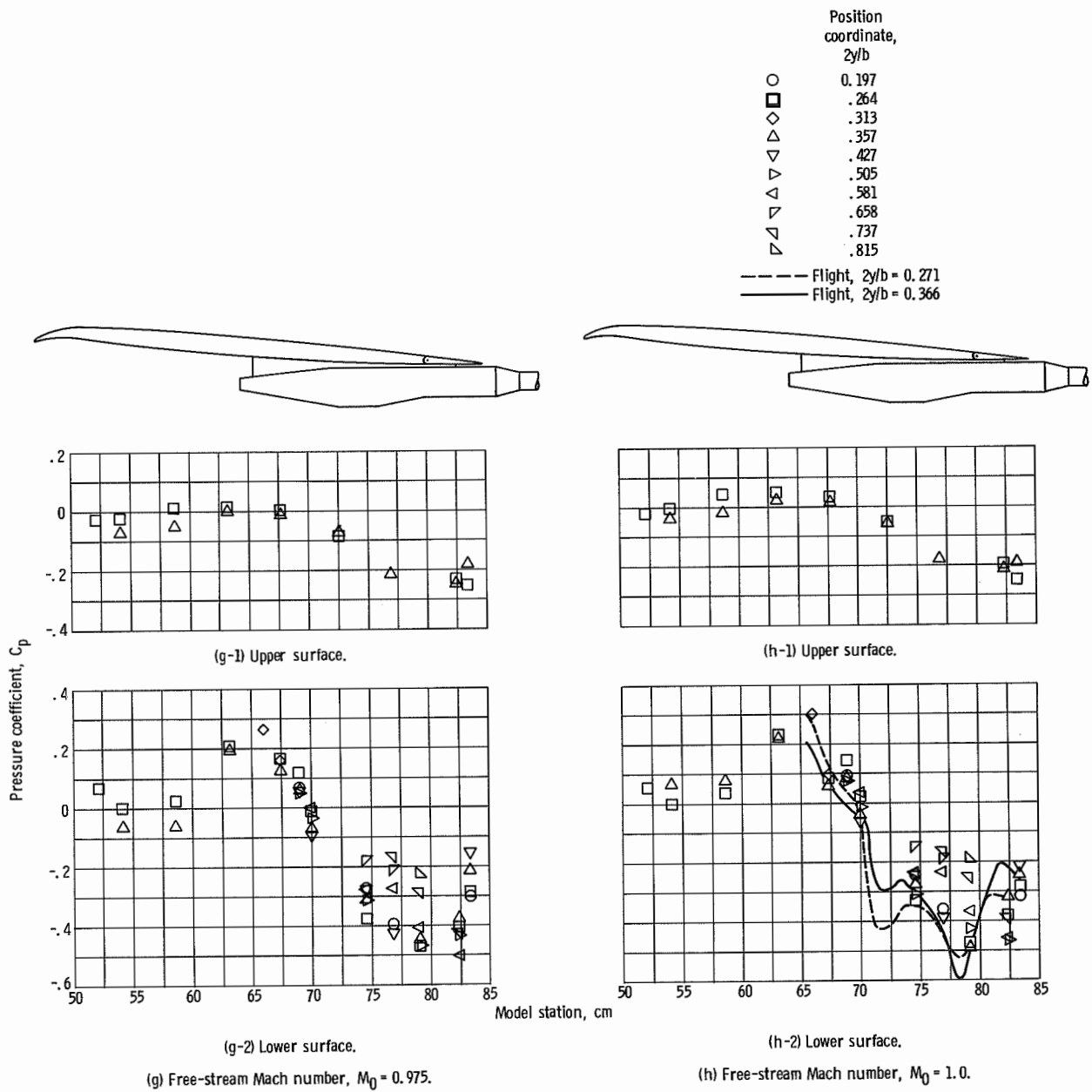
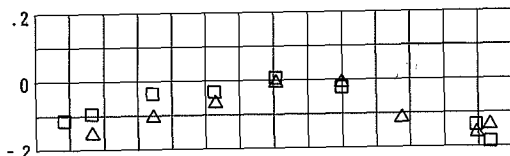
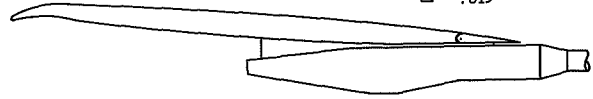
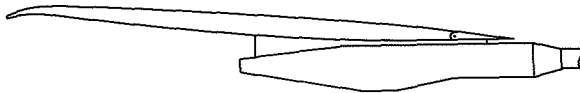


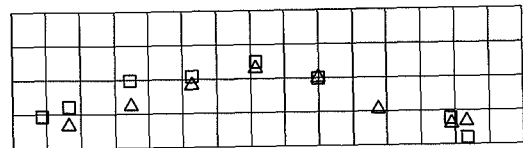
Figure 20. - Continued.

Position coordinate, $2y/b$

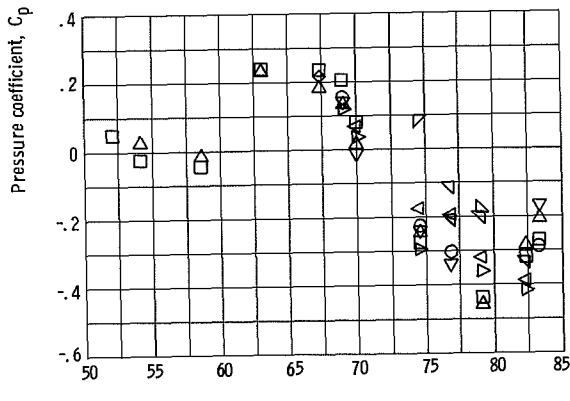
- 0.197
- .264
- ◇ .313
- △ .357
- ◁ .427
- ▽ .505
- ∇ .581
- ▽ .658
- ◁ .737
- ▽ .815



(i-1) Upper surface.

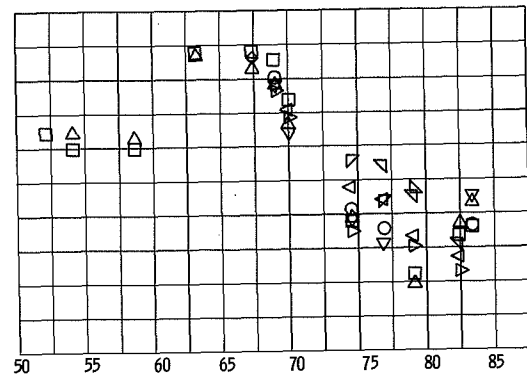


(j-1) Upper surface.



(i-2) Lower surface.

(i) Free-stream Mach number, $M_0 = 1.05$.



(j-2) Lower surface.

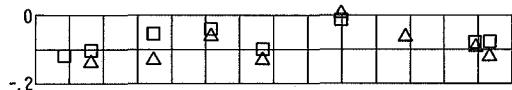
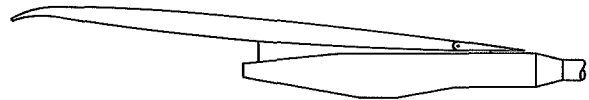
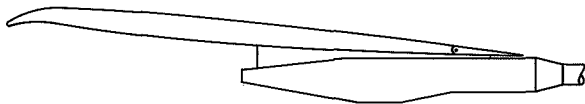
(j) Free-stream Mach number, $M_0 = 1.1$.

Figure 20. - Continued.

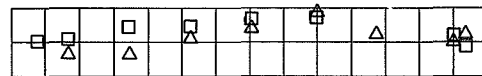
Position
coordinate,
 $2y/b$

- 0.197
- 0.264
- ◇ 0.313
- △ 0.357
- ▽ 0.427
- △ 0.505
- ▽ 0.581
- ▽ 0.658
- ▽ 0.737
- ▽ 0.815

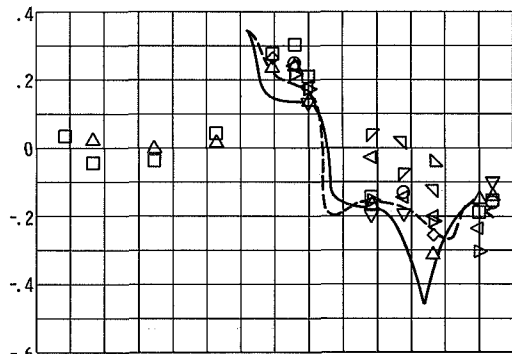
--- Flight, $2y/b = 0.271$
 --- Flight, $2y/b = 0.366$



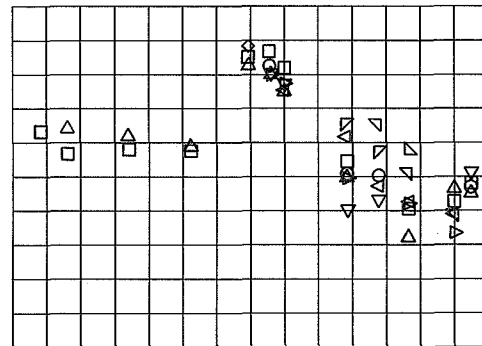
(k-1) Upper surface.



(l-1) Upper surface.



(k-1) Lower surface.

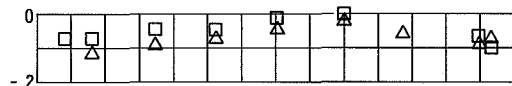


(l-2) Lower surface.

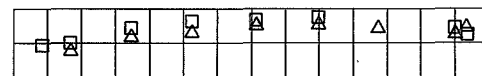
(k) Free-stream Mach number, $M_0 = 1.2$.

(l) Free-stream Mach number, $M_0 = 1.3$.

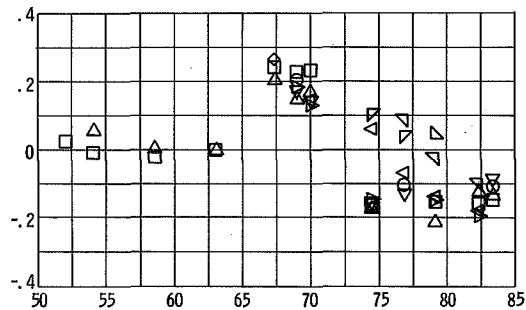
Pressure coefficient, C_p



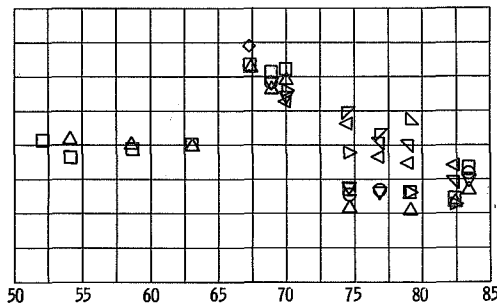
(m-1) Upper surface.



(n-1) Upper surface.



(m-2) Lower surface.



(n-2) Lower surface.

(m) Free-stream Mach number, $M_0 = 1.4$.

(n) Free-stream Mach number, $M_0 = 1.5$.

Model station, cm

Figure 20. - Concluded.

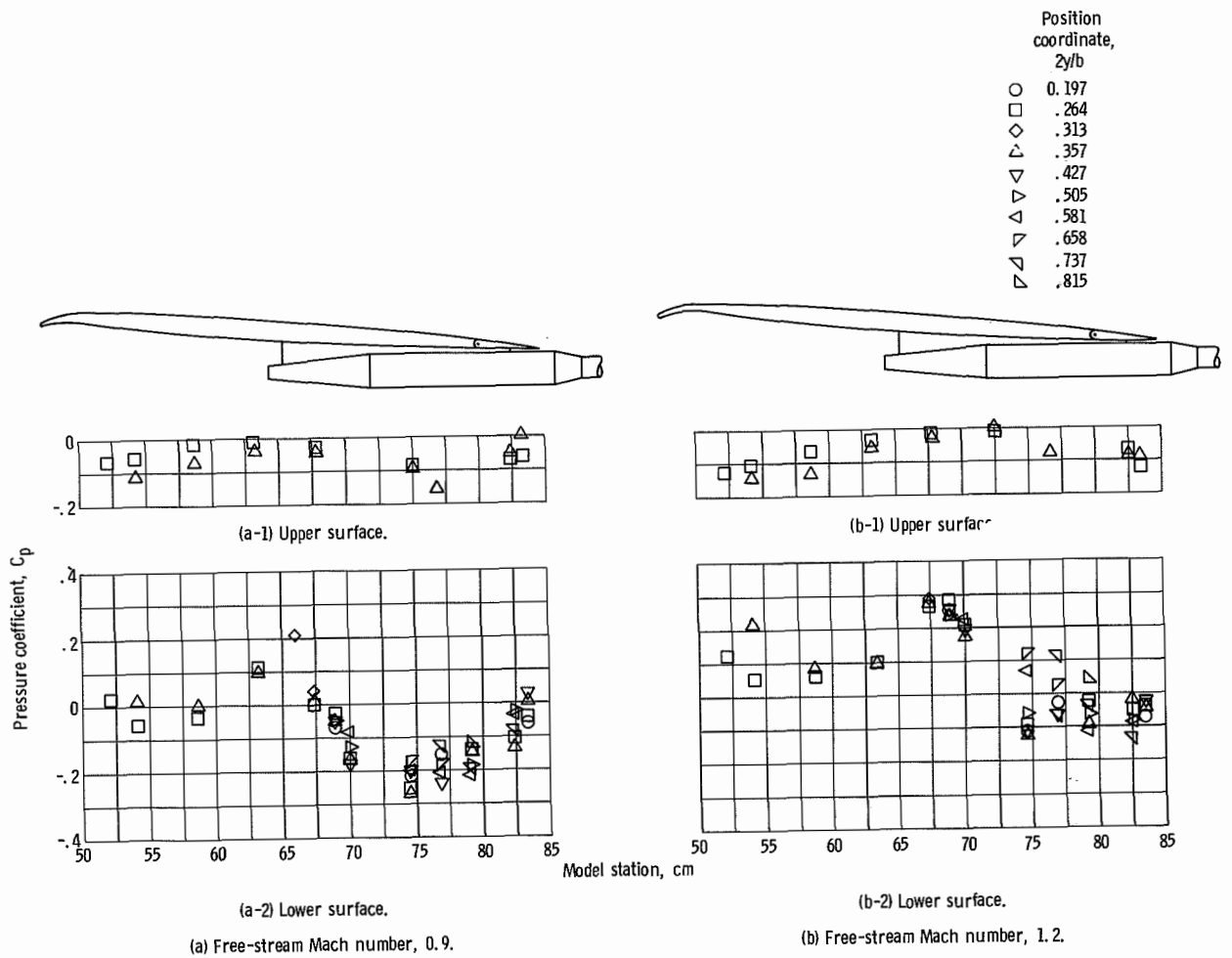


Figure 21. - Wing pressure distribution with open cylindrical nacelles. Angle of attack, 2.5° .

Angle of attack, α , deg	
○	2.5
□	4.5
△	6.5
▽	8.5
◁	15.0

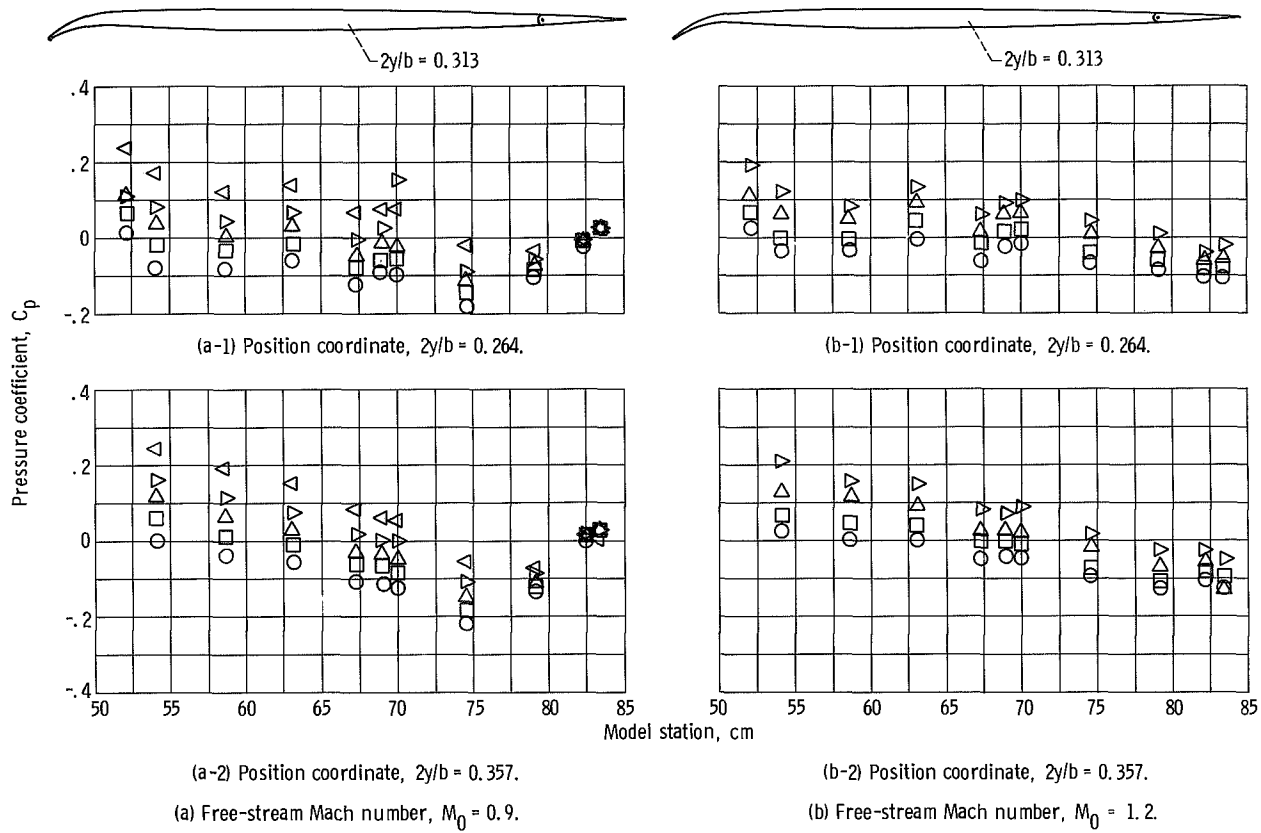
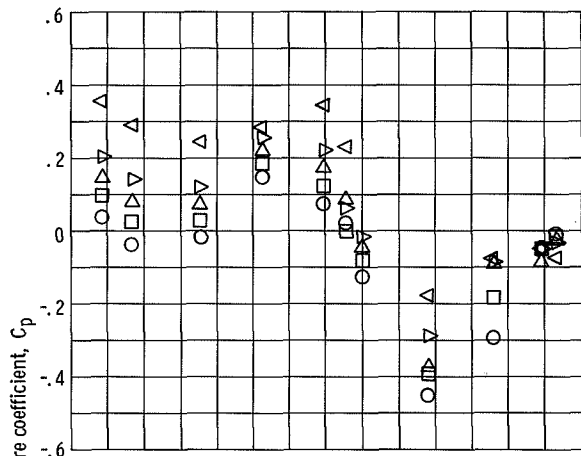
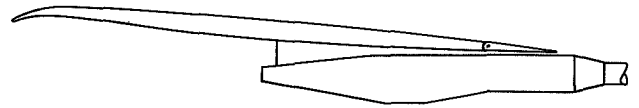
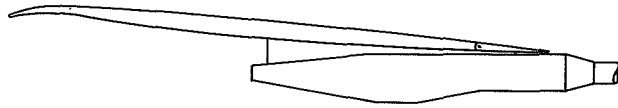
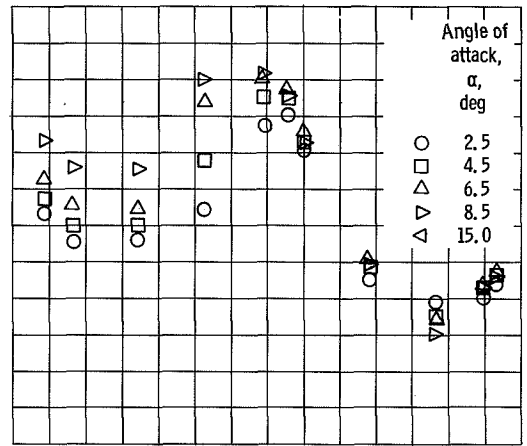


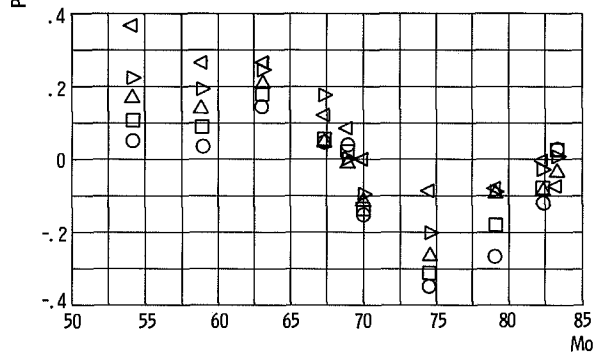
Figure 22. - Effect of angle of attack on wing-lower-surface pressure distribution without nacelles.



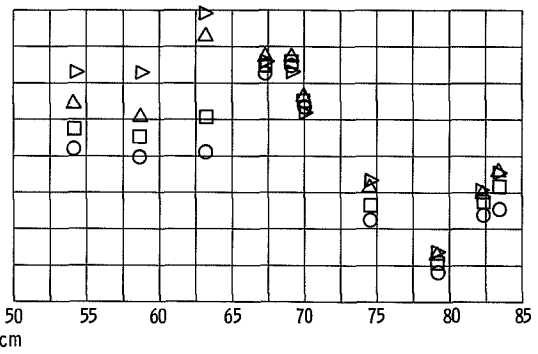
(a-1) Position coordinate, $2y/b = 0.264$.



(b-1) Position coordinate, $2y/b = 0.264$.



(a-2) Position coordinate, $2y/b = 0.357$.



(b-2) Position coordinate, $2y/b = 0.357$.

(a) Free-stream Mach number, $M_0 = 0.9$.

(b) Free-stream Mach number, $M_0 = 1.2$.

Figure 23. - Effect of angle of attack on wing-lower-surface pressure distribution with open bulged nacelles.

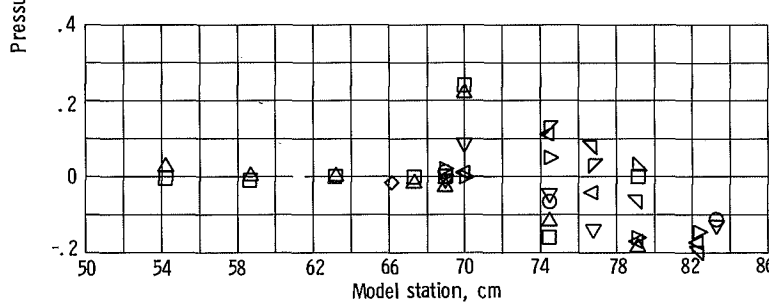
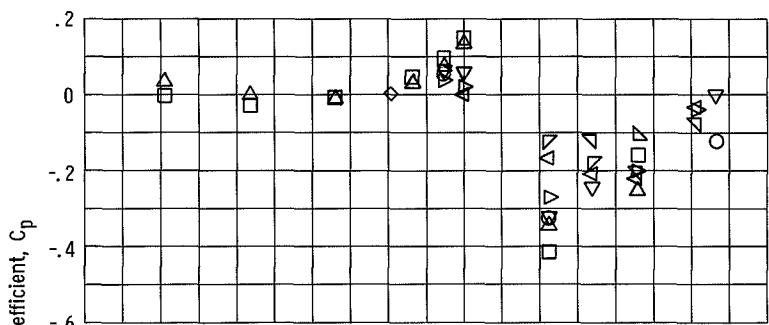
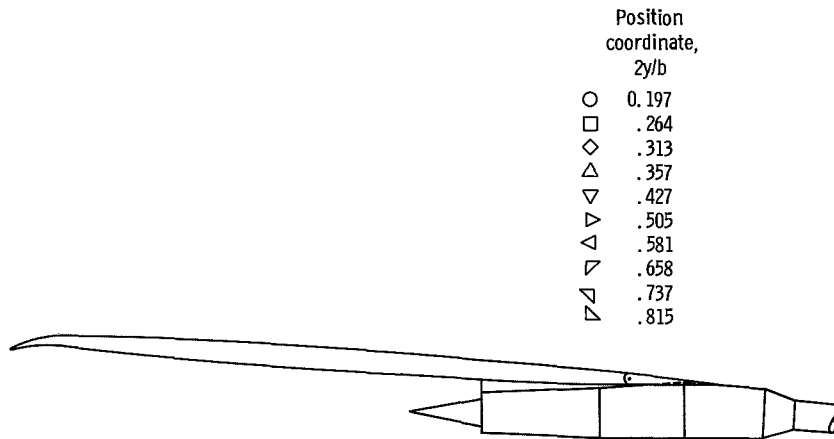
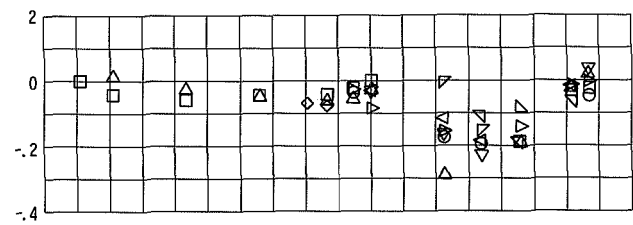


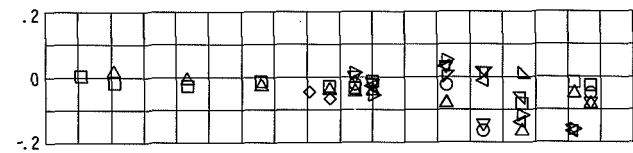
Figure 24. - Wing-lower-surface pressure distribution with bent nacelles. Angle of attack, 2.5° .

Position coordinate, $2y/b$

- 0.197
- .264
- ◇ .313
- △ .357
- ▽ .427
- △ .505
- ▽ .581
- △ .658
- ▽ .737
- △ .815



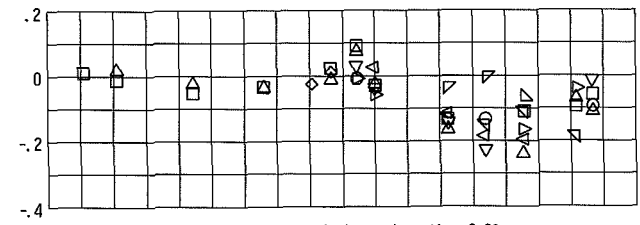
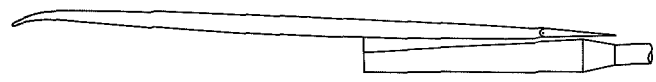
(a-1) Free-stream Mach number, $M_0 = 0.9$.



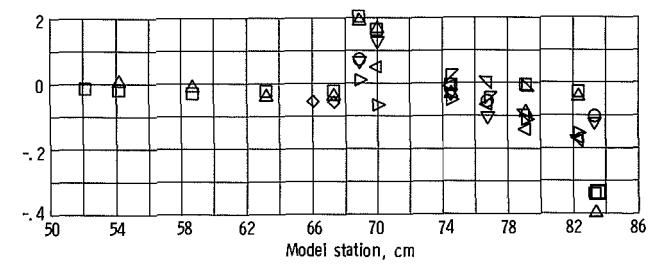
(a-2) Free-stream Mach number, $M_0 = 1.2$.

(a) Nacelle in aft position.

Pressure coefficient, C_p



(b-1) Free-stream Mach number, $M_0 = 0.90$.



(b-2) Free-stream Mach number, $M_0 = 1.2$.

(b) Nacelle in forward position.

Figure 25. - Wing-lower-surface pressure distribution with flared nacelles. Angle of attack, 2.5° .

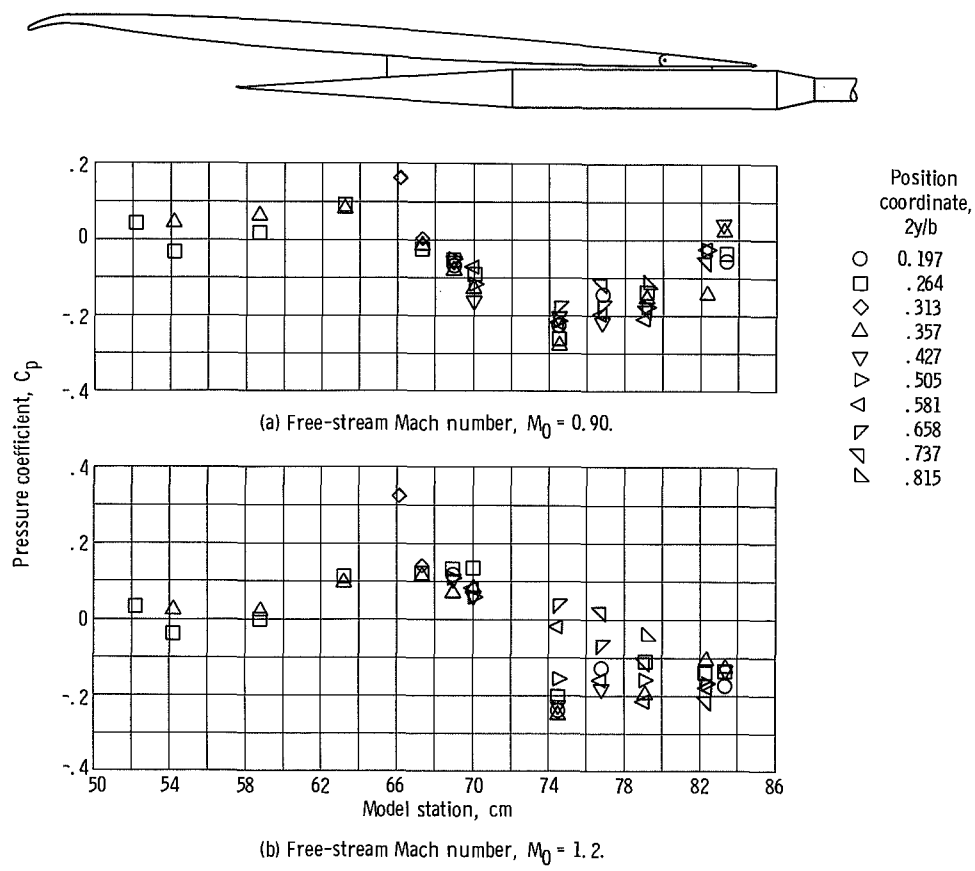
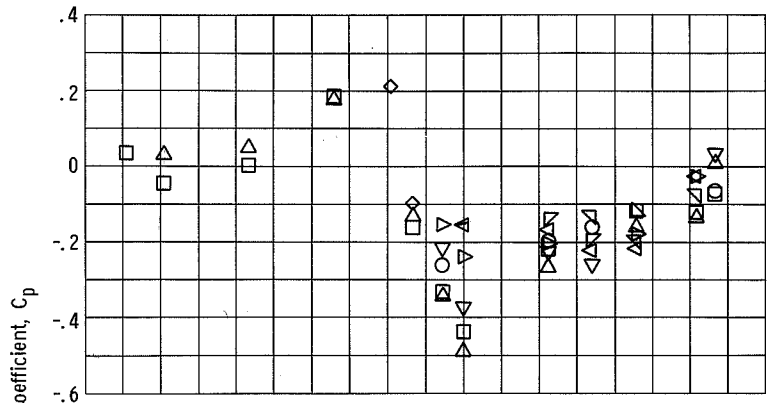
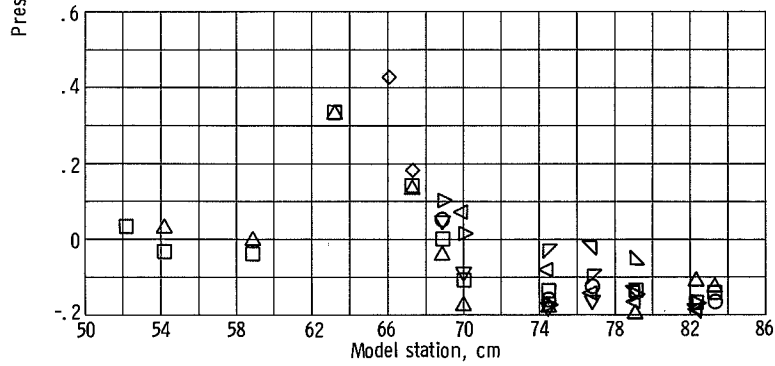


Figure 26. - Wing-lower-surface pressure distribution with solid cylindrical nacelle with 6.1° conic forebody. Angle of attack, 2.5° .

Position coordinate, $2y/b$	
○	0.197
□	.264
◇	.313
△	.357
▽	.427
▽	.505
△	.581
▽	.658
△	.737
▽	.815

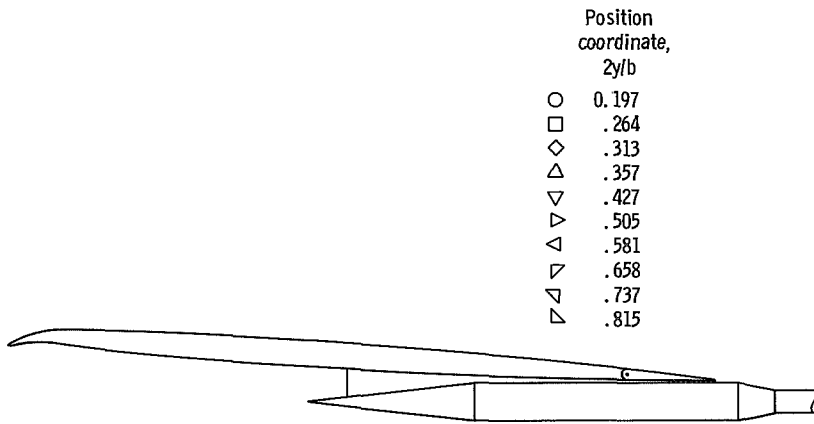


(a) Free-stream Mach number, $M_0 = 0.90$.

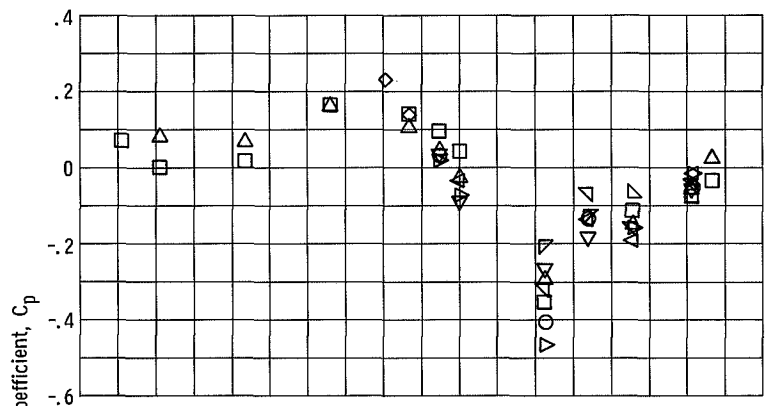


(b) Free-stream Mach number, $M_0 = 1.2$.

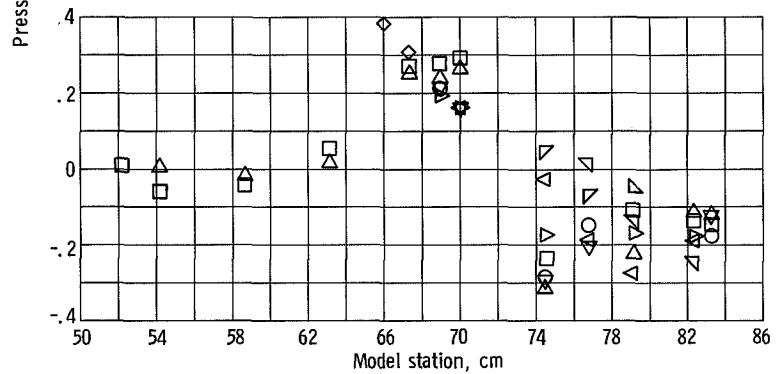
Figure 27. - Wing-lower-surface pressure distribution with solid cylindrical nacelle with ogive forebody. Angle of attack, 2.5° .



Position coordinate, $2y/b$	
○	0.197
□	.264
◇	.313
△	.357
▽	.427
▽	.505
△	.581
▽	.658
▽	.737
▽	.815



(a) Free-stream Mach number, $M_0 = 0.9$.



(b) Free-stream Mach number, $M_0 = 1.2$.

Figure 28. - Wing lower surface pressure distribution with solid cylindrical nacelle having 10° conic forebody at 2.5° angle of attack.

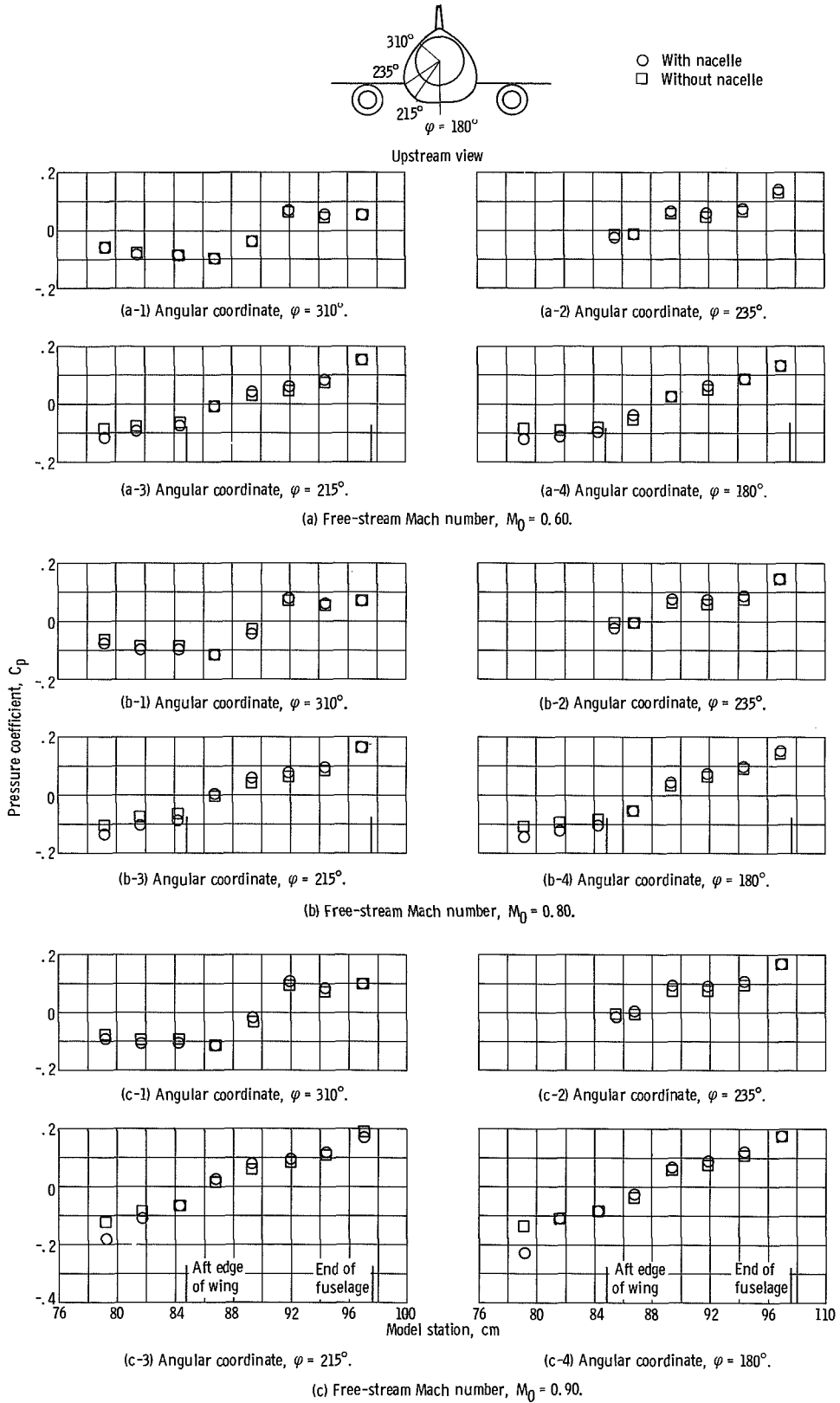
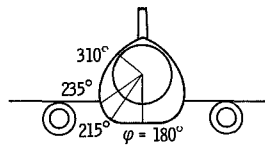


Figure 29. - Effect of nacelle on fuselage aft and pressure distribution with open bulged nacelles. Angle of attack, 0° .



○ With nacelle
 □ Without nacelle

Upstream view

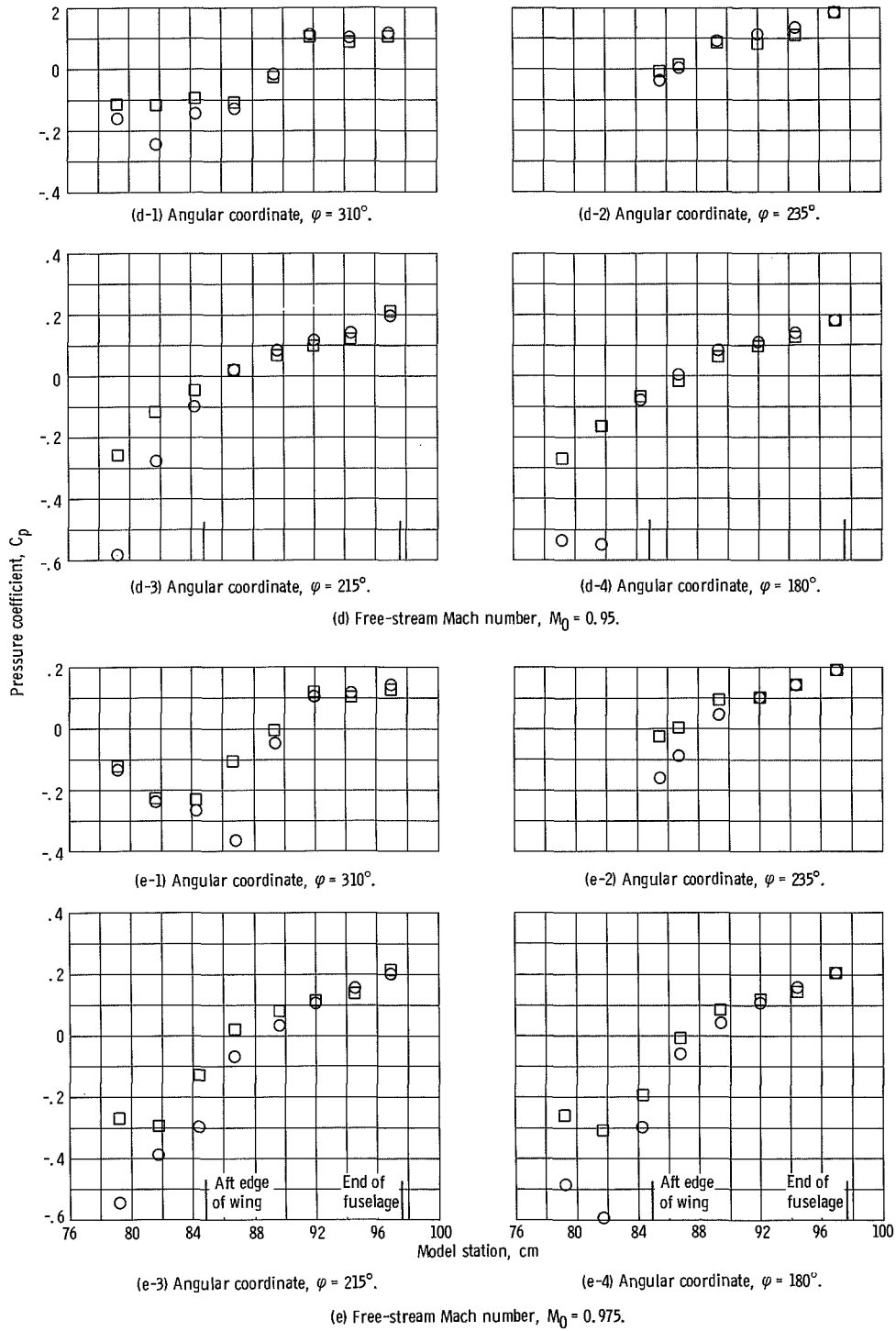


Figure 29. - Continued.

○ With nacelle
 □ Without nacelle

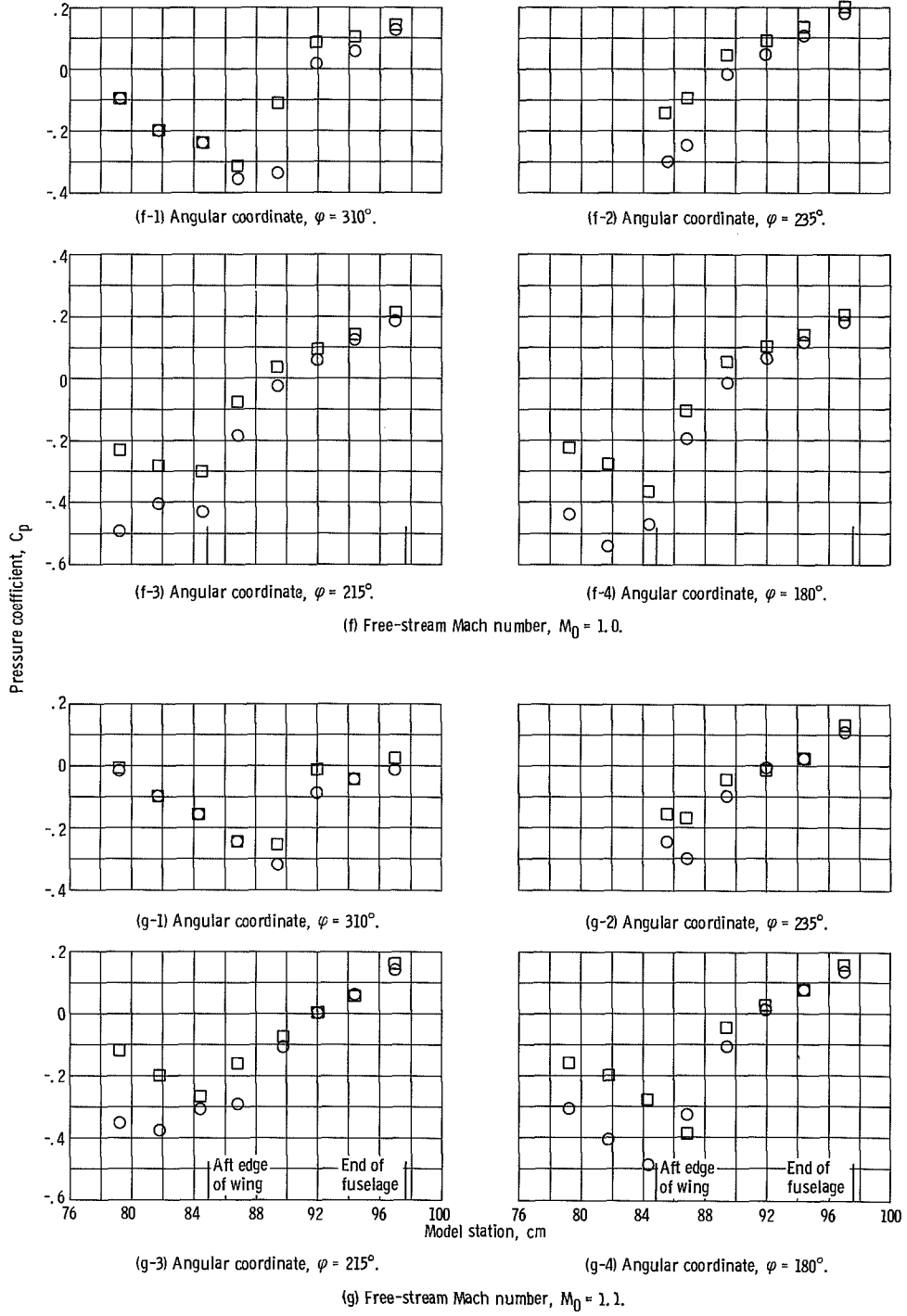
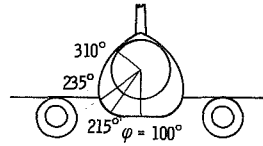


Figure 29. - Continued.

○ With nacelle
 □ Without nacelle

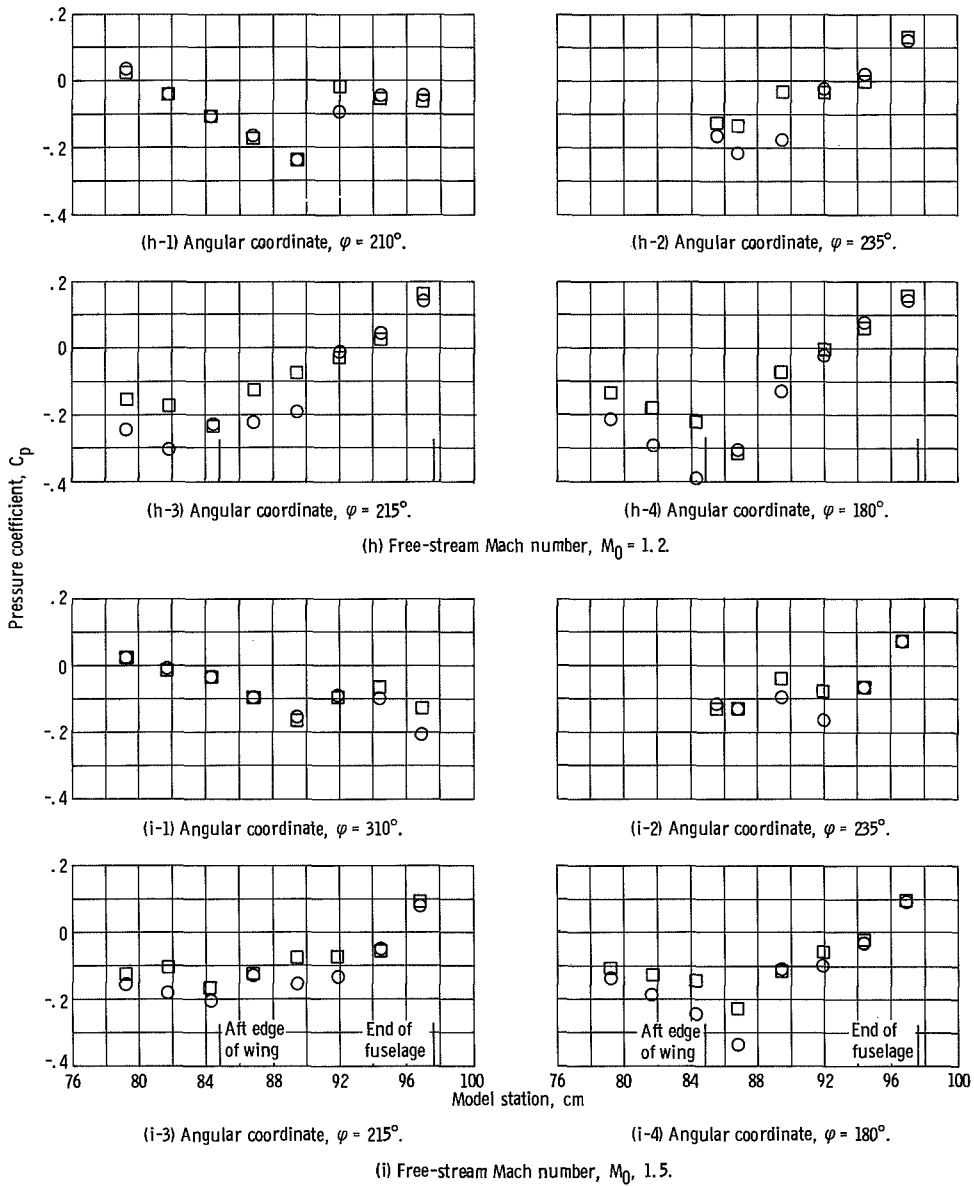
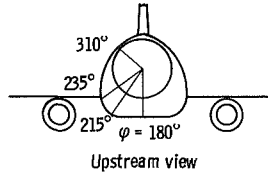
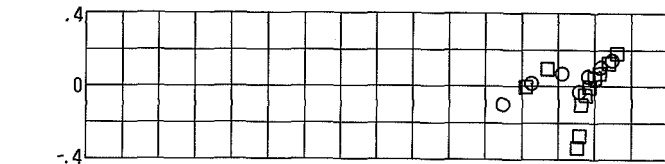
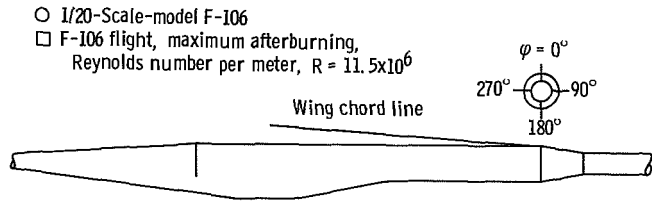
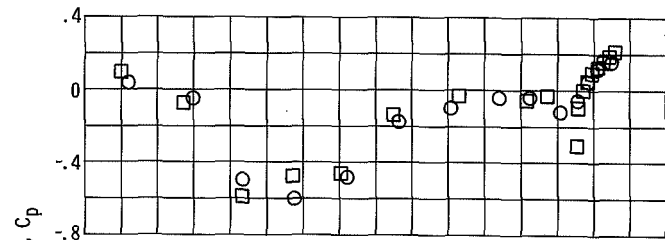


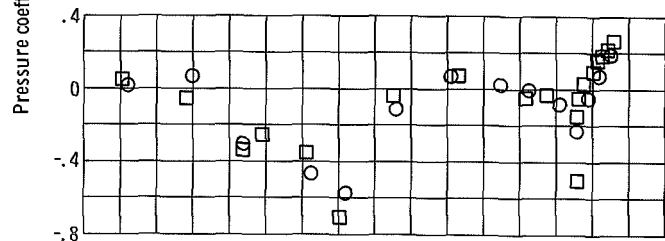
Figure 29. - Concluded.



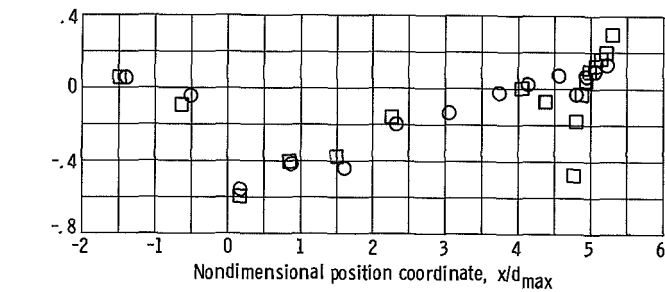
(a-1) Angular coordinate, $\varphi = 0^\circ$.



(a-2) Angular coordinate, $\varphi = 90^\circ$.



(a-3) Angular coordinate, $\varphi = 180^\circ$.

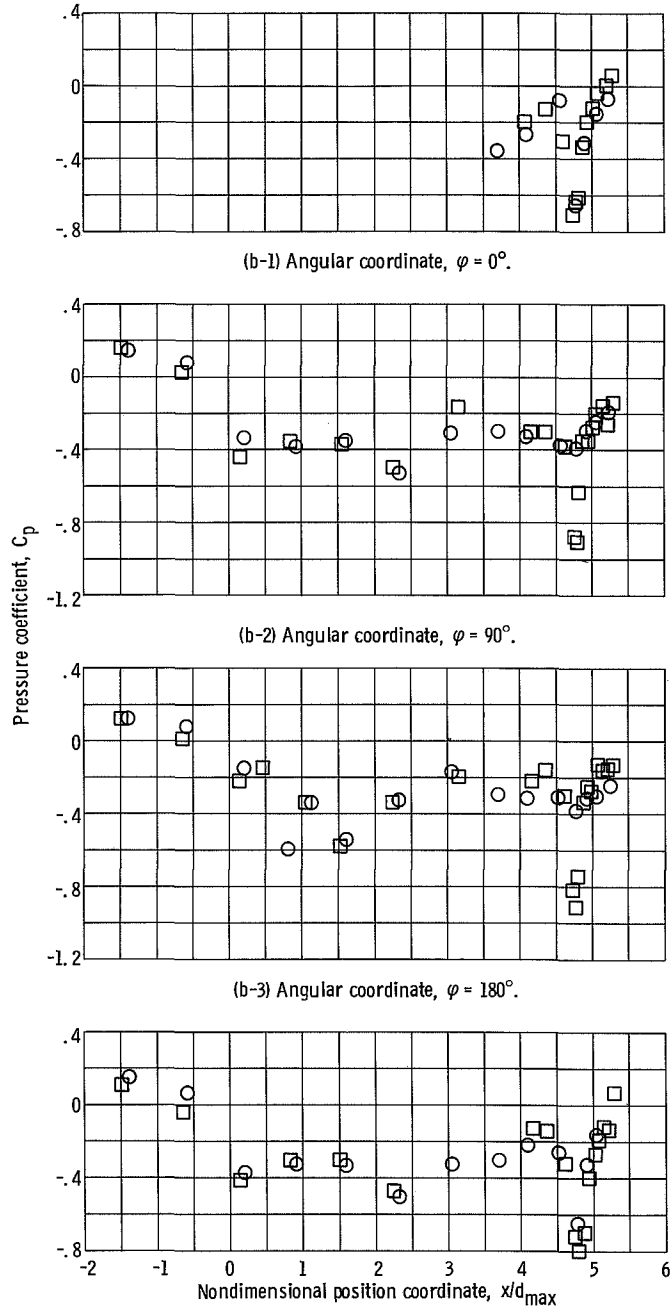
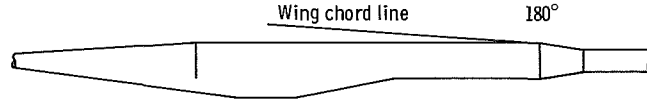
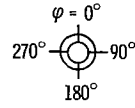


(a-4) Angular coordinate, $\varphi = 270^\circ$.

(a) Free-stream Mach number, $M_0 = 0.9$.

Figure 30. - Comparison of F-106 flight and 1/20-scale-model nacelle pressures. Bulged nacelles; boattail angle, 15° ; model angle of attack, 0° .

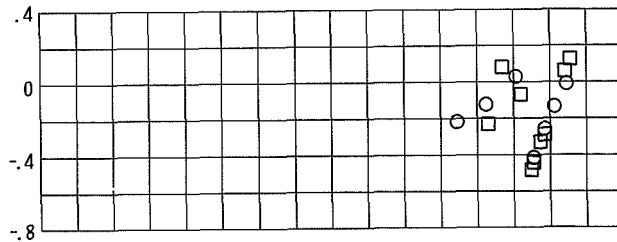
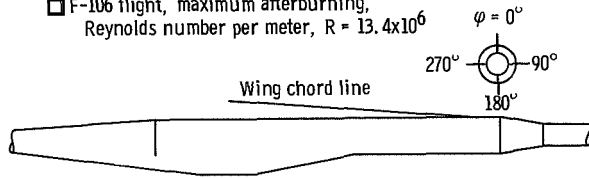
○ 1/20-Scale-model F-106
 □ F-106 flight, maximum afterburning,
 Reynolds number per meter, $R = 10.9 \times 10^6$



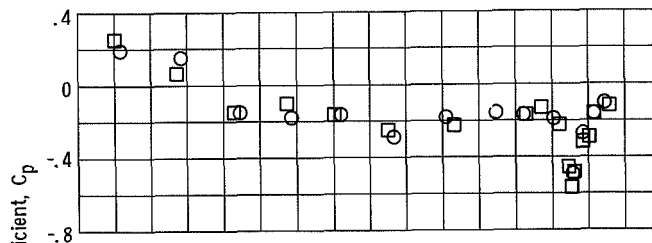
(b) Free-stream Mach number, $M_0 = 1.0$.

Figure 30. - Continued.

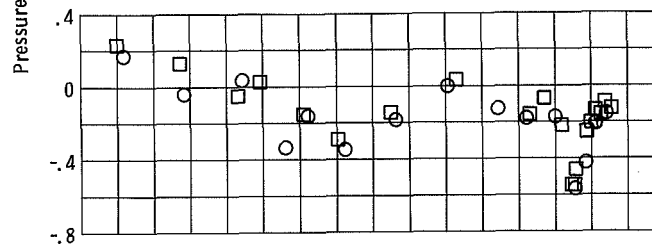
○ 1/20-Scale-model F-106
 □ F-106 flight, maximum afterburning,
 Reynolds number per meter, $R = 13.4 \times 10^6$



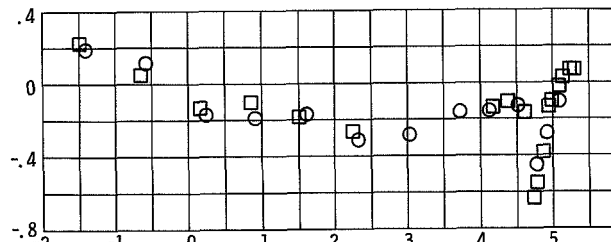
(c-1) Angular coordinate, $\psi = 0^\circ$.



(c-2) Angular coordinate, $\psi = 90^\circ$.



(c-3) Angular coordinate, $\psi = 180^\circ$.



(c-4) Angular coordinate, $\psi = 270^\circ$.

(c) Free-stream Mach number, $M_0 = 1.2$.

Figure 30. - Concluded.

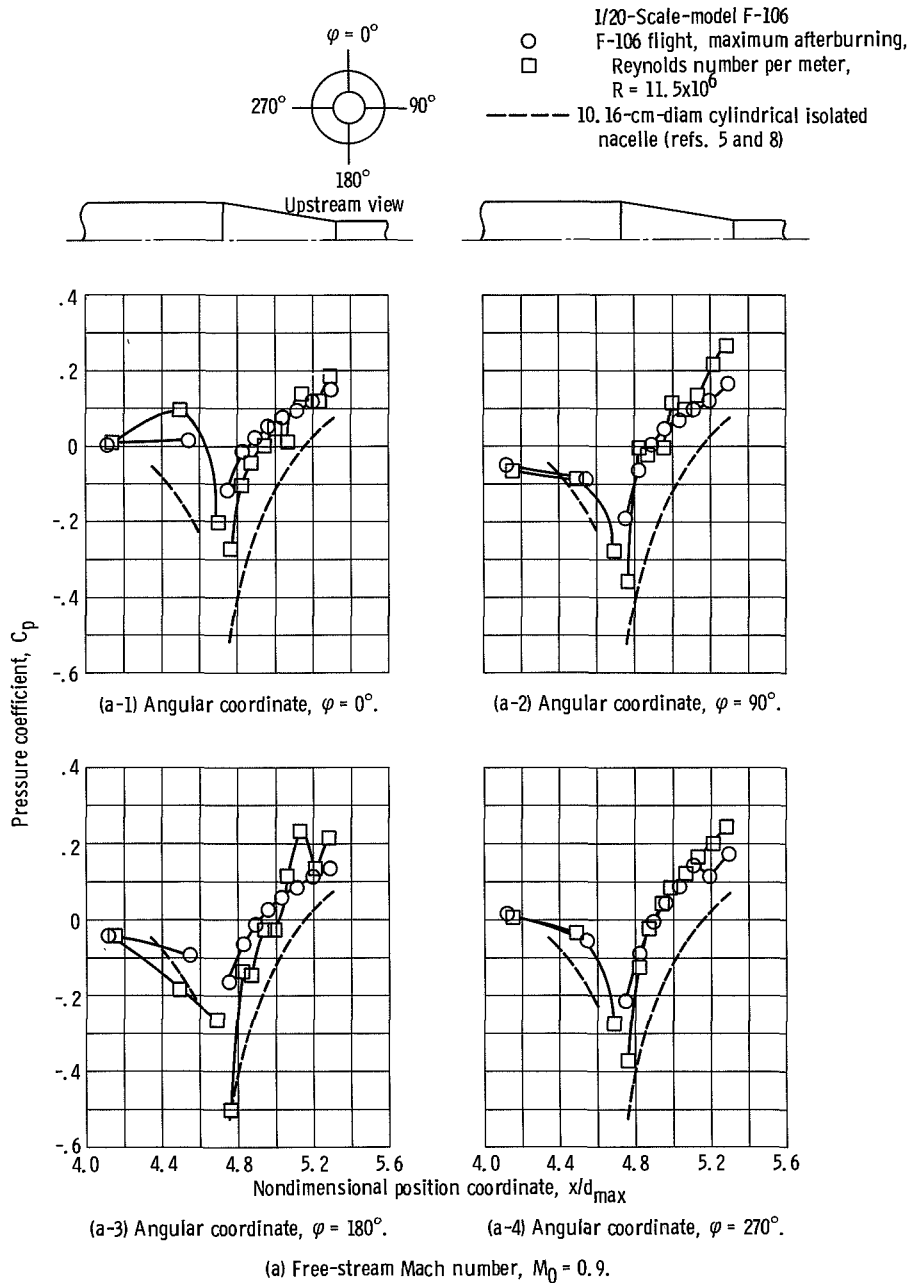
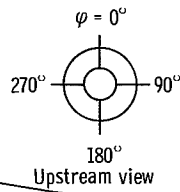
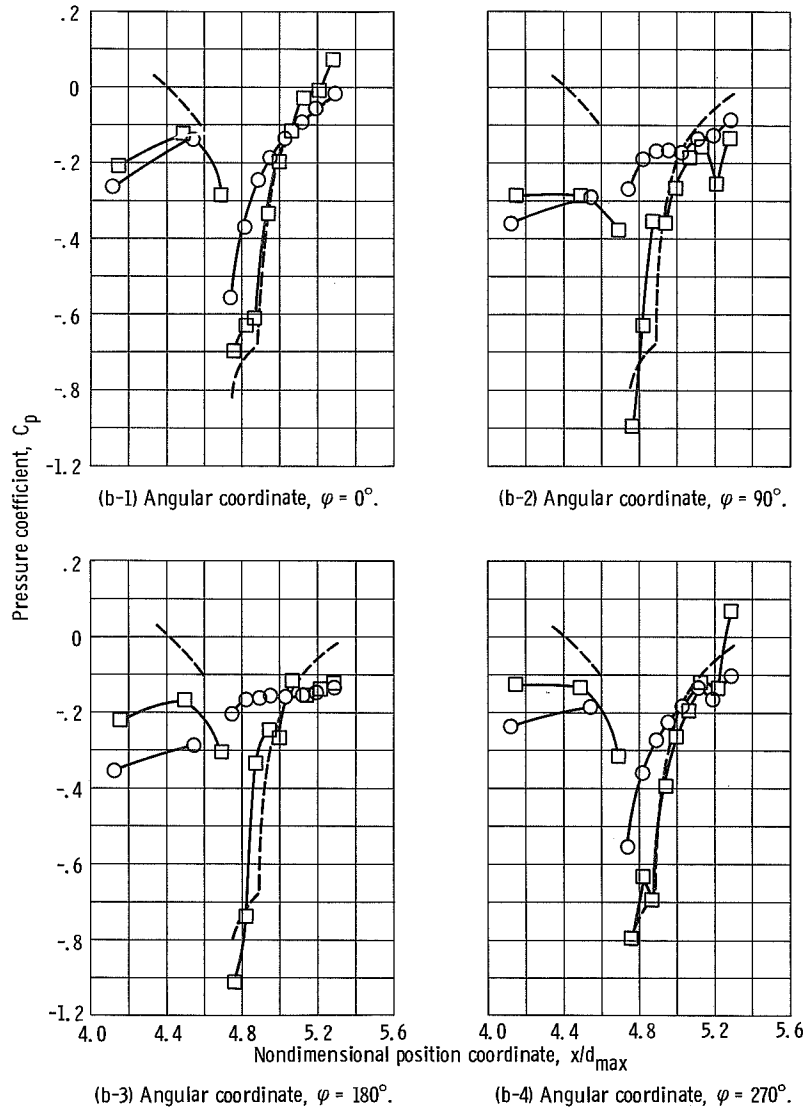


Figure 31. - Comparison of F-106 flight 15° boattail pressures and 1/20-scale-model F-106 boattail pressures. Solid cylindrical nacelles with 10° conic forebodies; angle of attack, 2.5°.

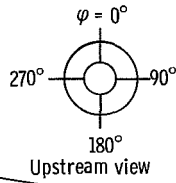


1/20-Scale-model F-106
 F-106 flight, maximum after-
 burning, Reynolds number
 per meter, $R = 10.9 \times 10^6$
 10.16-cm-diam cylindrical
 isolated nacelle (refs. 5 and 8)



(b) Free-stream Mach number, $M_0 = 1.0$.

Figure 31. - Continued.



1/20-Scale-model F-106
 F-106 flight, maximum after-
 burning, Reynolds number
 per meter, $R = 13.4 \times 10^6$
 10.16-cm-diam cylindrical
 isolated nacelle (refs. 5 and 8)

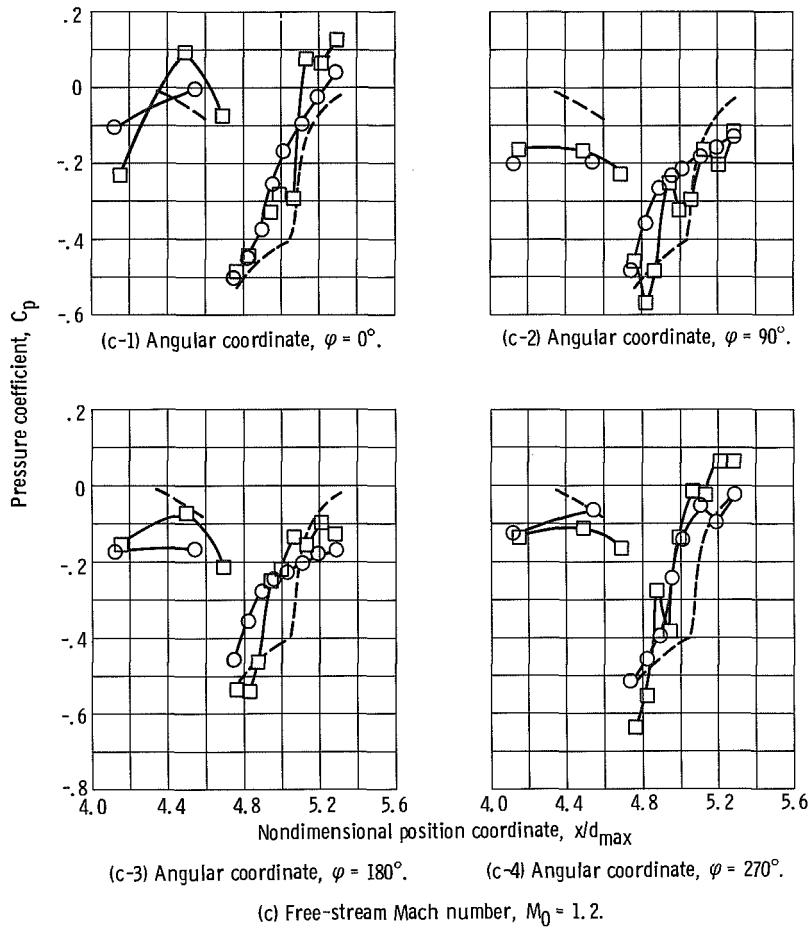
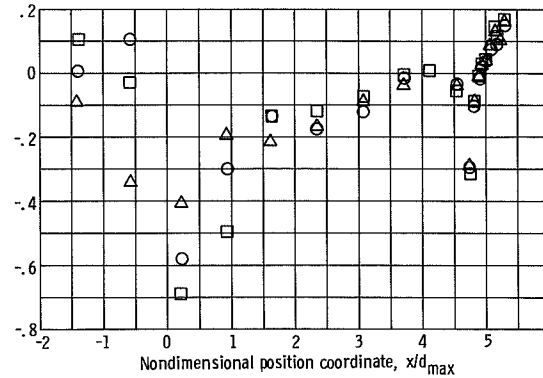
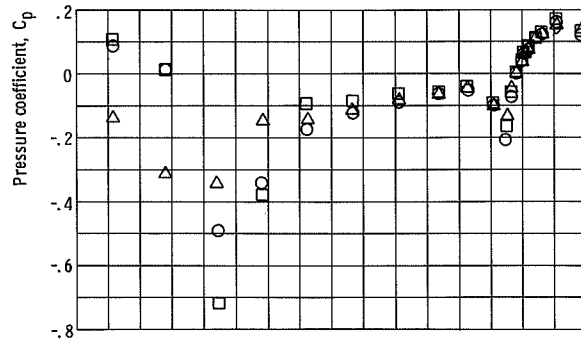
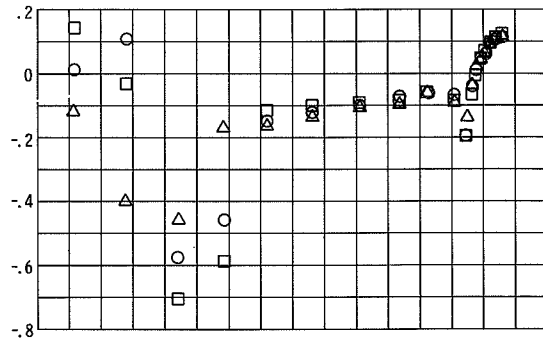
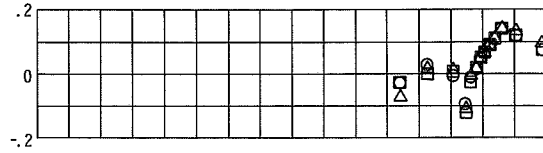
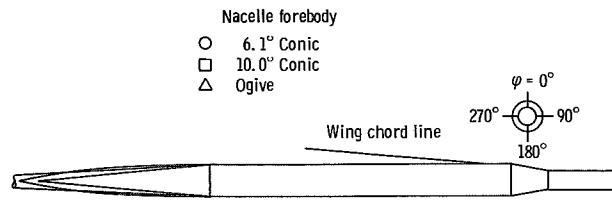
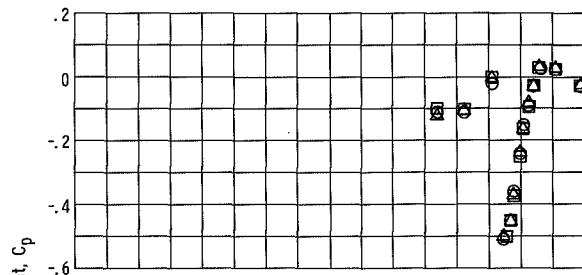
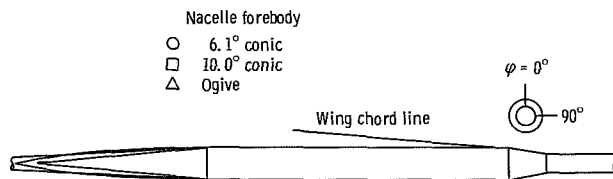


Figure 31. - Concluded.

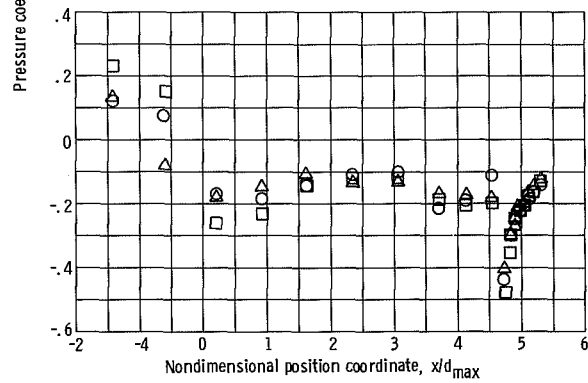


(a) Free-stream Mach number, $M_\infty = 0.9$.

Figure 32. - Effect of forebody shape on solid cylindrical nacelle pressure. Angle of attack, 2.5°; boattail angle, 15°.



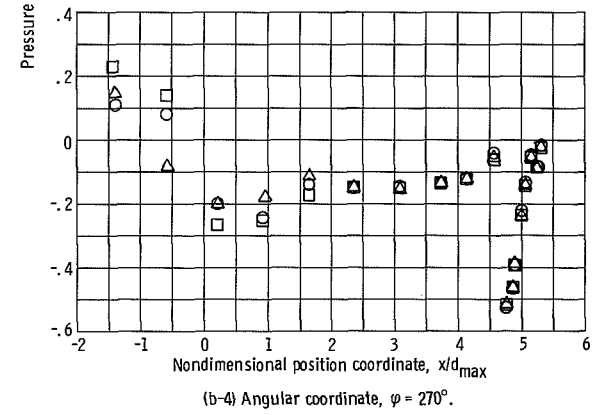
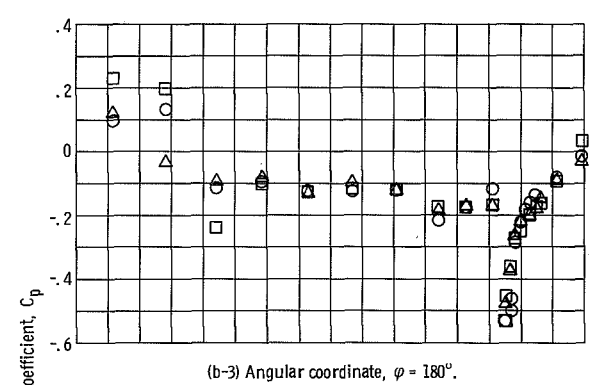
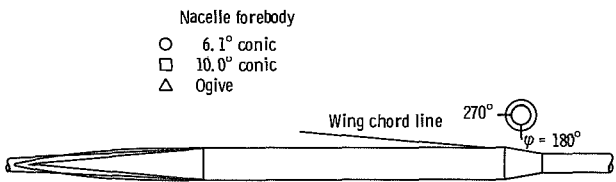
(b-1) Angular coordinate, $\varphi = 0^\circ$.



(b-2) Angular coordinate, $\varphi = 90^\circ$.

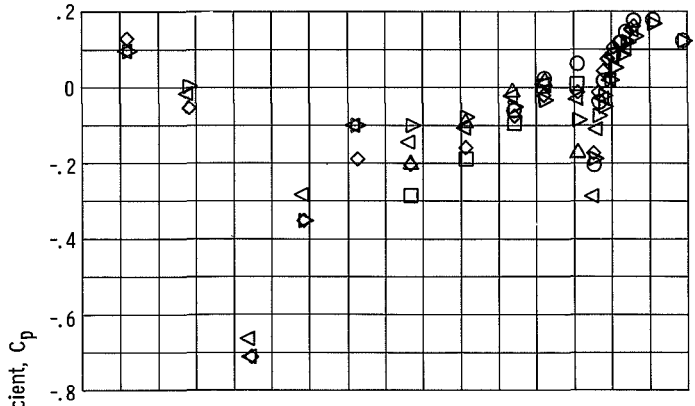
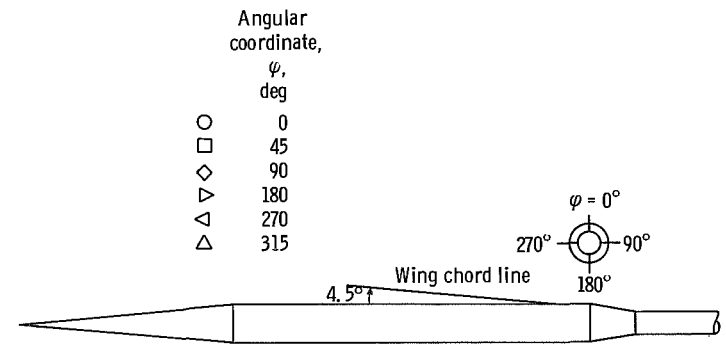
(b) Free-stream Mach number, $M_0 = 1.2$.

Figure 32. - Continued.

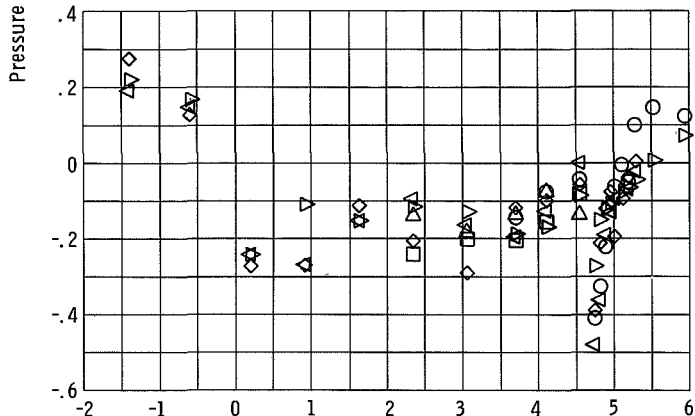


(b) Concluded.

Figure 32. - Concluded.

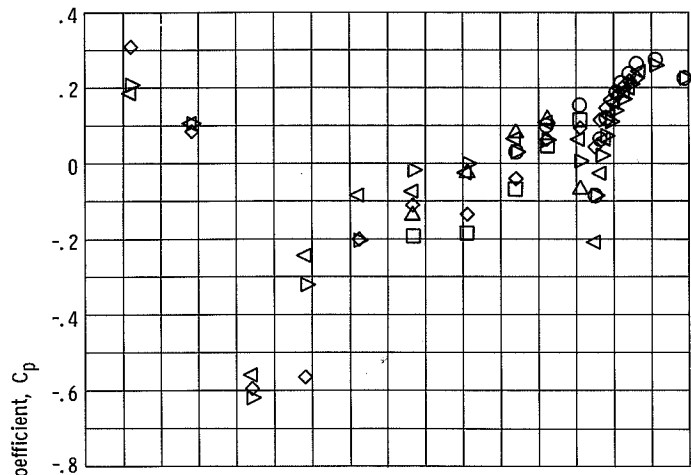
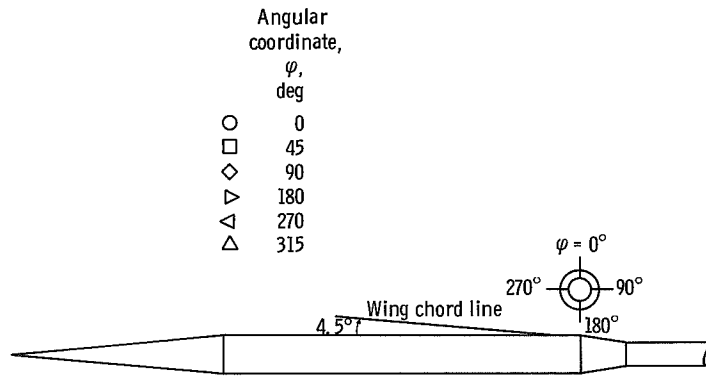


(a) Free-stream Mach number, $M_0 = 0.9$.

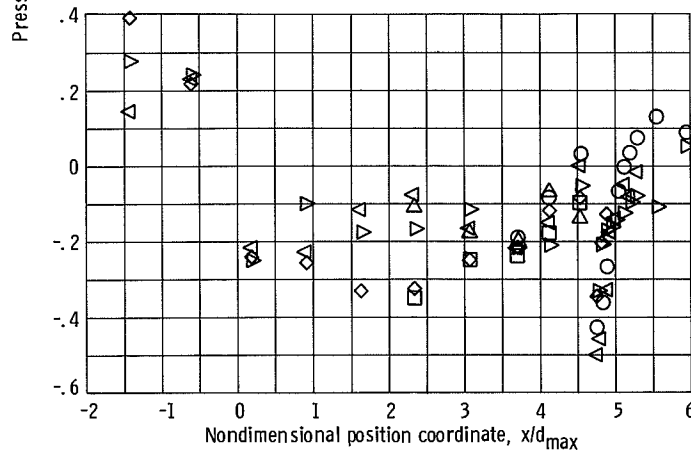


(b) Free-stream Mach number, $M_0 = 1.2$.

Figure 33. - Pressure distribution on solid cylindrical nacelle with 10° conic forebody in outboard position, without inboard nacelle. Angle of attack, 2.5° ; boattail angle, 15° .



(a) Free-stream Mach number, $M_0 = 0.9$.



(b) Free-stream Mach number, $M_0 = 1.2$.

Figure 34. - Pressure distribution on solid cylindrical nacelle with 10° conic forebody in outboard position, with inboard nacelle. Angle of attack, 2.5° ; boattail angle, 15° .

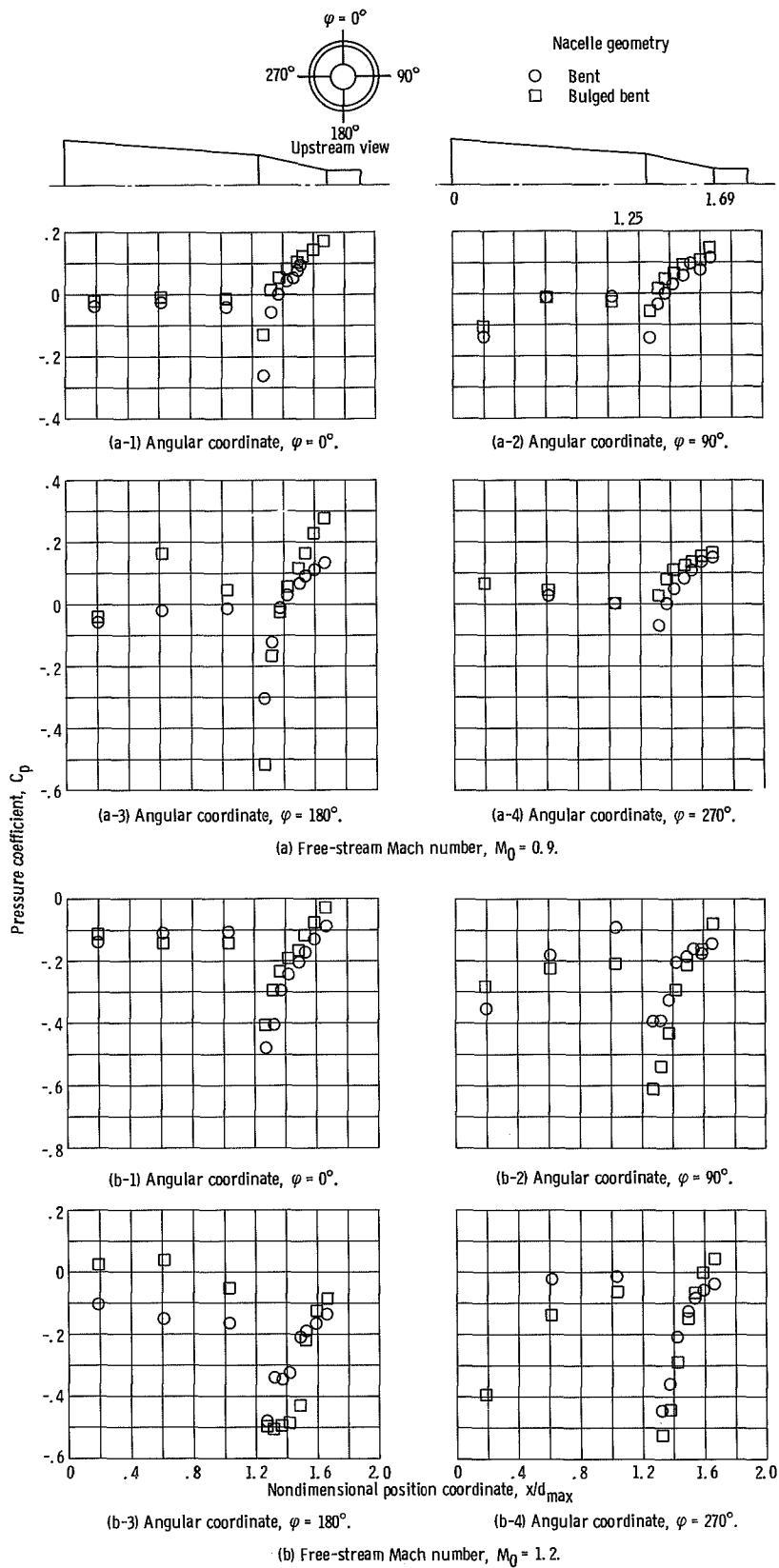


Figure 35. - Bent-nacelle pressures at 2.5° angle of attack.

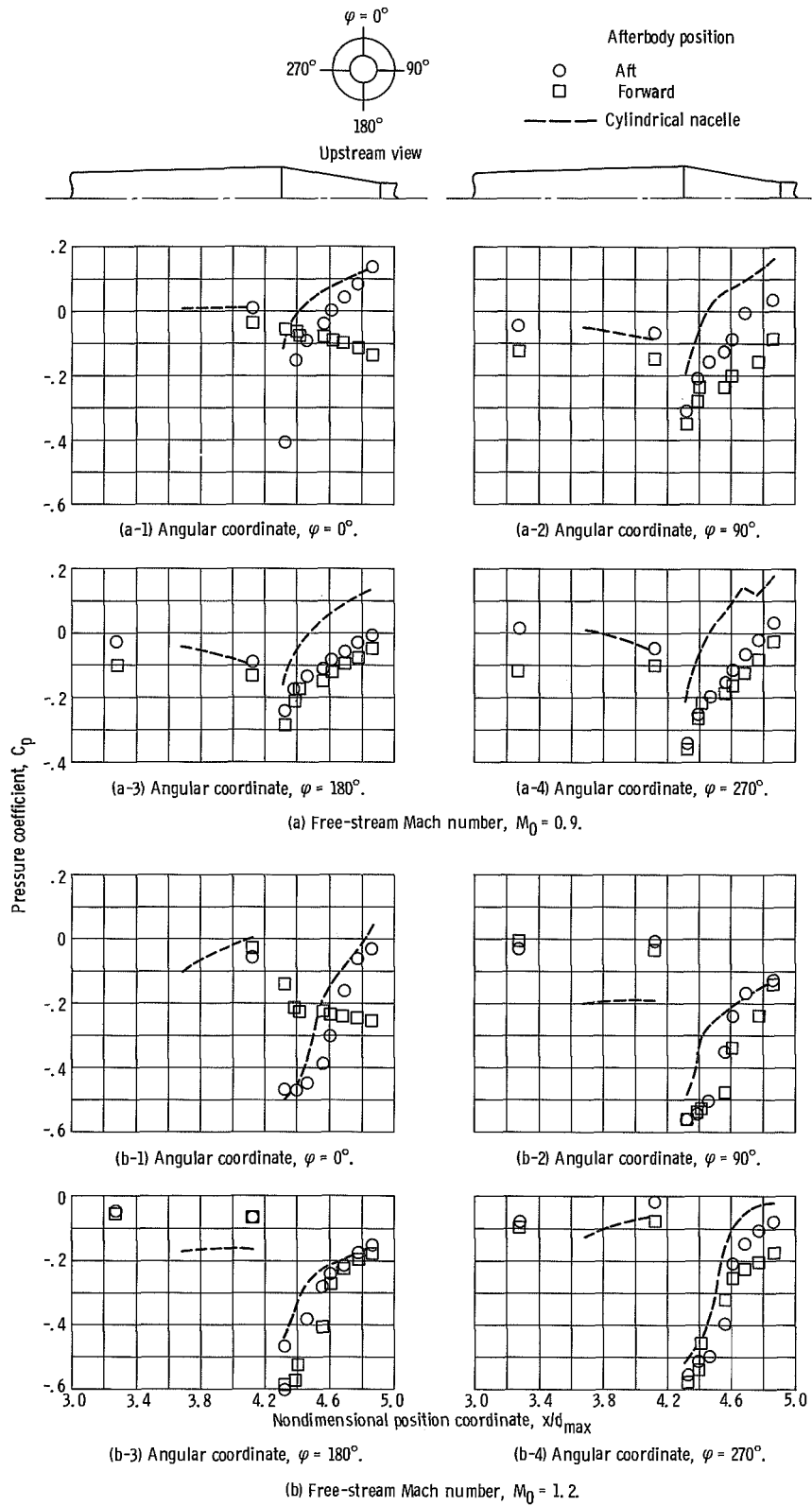


Figure 36. - Flared-nacelle pressures at 2.5° angle of attack.

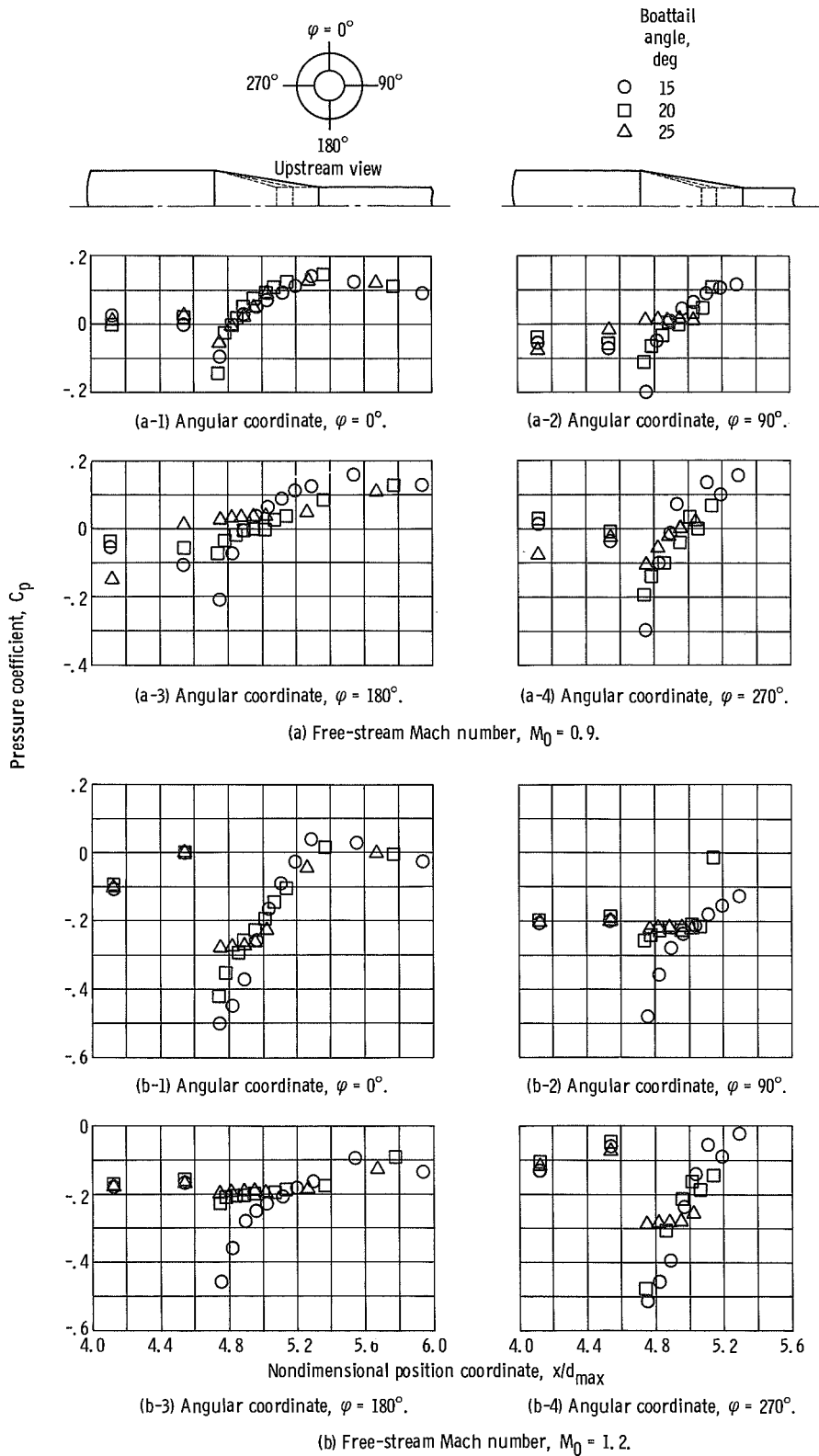


Figure 37. - Effect of increased boattail angle on afterbody pressures. Solid cylindrical nacelles with 10° conic forebody; angle of attack, 2.5° .

NATIONAL AERONAUTICS AND SPACE ADMINISTRATION
WASHINGTON, D. C. 20546
OFFICIAL BUSINESS

FIRST CLASS MAIL



POSTAGE AND FEES PAID
NATIONAL AERONAUTICS AND
SPACE ADMINISTRATION

POSTMASTER: If Undeliverable (Section 109
Postal Manual) Do Not Return

"The aeronautical and space activities of the United States shall be conducted so as to contribute . . . to the expansion of human knowledge of phenomena in the atmosphere and space. The Administration shall provide for the widest practicable and appropriate dissemination of information concerning its activities and the results thereof."

—NATIONAL AERONAUTICS AND SPACE ACT OF 1958

NASA SCIENTIFIC AND TECHNICAL PUBLICATIONS

TECHNICAL REPORTS: Scientific and technical information considered important, complete, and a lasting contribution to existing knowledge.

TECHNICAL NOTES: Information less broad in scope but nevertheless of importance as a contribution to existing knowledge.

TECHNICAL MEMORANDUMS: Information receiving limited distribution because of preliminary data, security classification, or other reasons.

CONTRACTOR REPORTS: Scientific and technical information generated under a NASA contract or grant and considered an important contribution to existing knowledge.

TECHNICAL TRANSLATIONS: Information published in a foreign language considered to merit NASA distribution in English.

SPECIAL PUBLICATIONS: Information derived from or of value to NASA activities. Publications include conference proceedings, monographs, data compilations, handbooks, sourcebooks, and special bibliographies.

TECHNOLOGY UTILIZATION PUBLICATIONS: Information on technology used by NASA that may be of particular interest in commercial and other non-aerospace applications. Publications include Tech Briefs, Technology Utilization Reports and Notes, and Technology Surveys.

Details on the availability of these publications may be obtained from:

SCIENTIFIC AND TECHNICAL INFORMATION DIVISION
NATIONAL AERONAUTICS AND SPACE ADMINISTRATION
Washington, D.C. 20546